Monthly Notices of the ROYAL ASTRONOMICAL SOCIETY

MNRAS **436,** 34–70 (2013)
Advance Access publication 2013 September 26

doi:10.1093/mnras/stt1417

The *GALEX* Arecibo SDSS Survey – VIII. Final data release. The effect of group environment on the gas content of massive galaxies

Barbara Catinella,[1,2]⋆ David Schiminovich,[3] Luca Cortese,[2,4] Silvia Fabello,[5] Cameron B. Hummels,[6] Sean M. Moran,[7] Jenna J. Lemonias,[3] Andrew P. Cooper,[8] Ronin Wu,[9] Timothy M. Heckman[10] and Jing Wang[1]

[1]*Max-Planck Institut für Astrophysik, D-85741 Garching, Germany*
[2]*Centre for Astrophysics and Supercomputing, Swinburne University of Technology, Hawthorn, VIC 3122, Australia*
[3]*Department of Astronomy, Columbia University, New York, NY 10027, USA*
[4]*European Southern Observatory, D-85748 Garching, Germany*
[5]*Autoliv Electronics Germany, Theodor-Heuss-Str. 2, D-85221 Dachau, Germany*
[6]*Department of Astronomy and Steward Observatory, University of Arizona, Tucson, AZ 85721, USA*
[7]*Smithsonian Astrophysical Observatory, 60 Garden Street, Cambridge, MA 02138, USA*
[8]*National Astronomical Observatories, Chinese Academy of Sciences, 20A Datun Rd, Chaoyang, Beijing 100012, People's Republic of China*
[9]*Commissariat à l'Energie Atomique (CEA), F-91191 Gif-sur-Yvette, France*
[10]*Department of Physics and Astronomy, Johns Hopkins University, Baltimore, MD 21218, USA*

Accepted 2013 July 25. Received 2013 July 19; in original form 2013 May 13

ABSTRACT

We present the final data release from the *GALEX* Arecibo SDSS Survey (GASS), a large Arecibo programme that measured the H I properties for an unbiased sample of ∼800 galaxies with stellar masses greater than 10^{10} M$_\odot$ and redshifts $0.025 < z < 0.05$. This release includes new Arecibo observations for 250 galaxies. We use the full GASS sample to investigate environmental effects on the cold gas content of massive galaxies at fixed stellar mass. The environment is characterized in terms of dark matter halo mass, obtained by cross-matching our sample with the Sloan Digital Sky Survey (SDSS) group catalogue of Yang et al. Our analysis provides, for the first time, clear statistical evidence that massive galaxies located in haloes with masses of $10^{13}-10^{14}$ M$_\odot$ have at least 0.4 dex less H I than objects in lower density environments. The process responsible for the suppression of gas in group galaxies most likely drives the observed quenching of the star formation in these systems. Our findings strongly support the importance of the group environment for galaxy evolution, and have profound implications for semi-analytic models of galaxy formation, which currently do not allow for stripping of the cold interstellar medium in galaxy groups.

Key words: galaxies: evolution – galaxies: fundamental parameters – radio lines: galaxies – ultraviolet: galaxies.

1 INTRODUCTION

As the source of the material that will eventually form stars, atomic hydrogen (H I) is clearly a key ingredient to understand how galaxies form and evolve. For instance, physical processes that transform galaxies from blue, star-forming to 'red and dead' objects must deplete their gas reservoirs first, so that their star formation is quenched as a result. Systematic studies of the cold gas content of galaxies as a function of their star formation, mass and structural properties, and across all environmental densities (e.g. Catinella et al. 2010; Huang et al. 2012), are necessary to explain the variety of systems observed today in the local Universe, and to provide important constraints to theoretical models and simulations of galaxy formation (e.g. Fu et al. 2010; Davé, Finlator & Oppenheimer 2011; Lagos et al. 2011; Kauffmann et al. 2012).

Environmental mechanisms are known to be effective in removing gas from galaxies in high-density regions, and indeed H I is one of the most sensitive tracers of environmental effects. This is because H I gas typically extends further away from the centre of galaxies compared to other baryonic components; thus, it is more easily affected by environment. A classic example of the value of H I observations in this context is represented by spatially resolved radio observations of the M81 group, which have revealed a spectacular, complex network of gas filaments connecting three galaxies that appear completely undisturbed in optical images (Yun, Ho & Lo 1994).

⋆ E-mail: bcatinella@swin.edu.au

© 2013 The Authors
Published by Oxford University Press on behalf of the Royal Astronomical Society

Downloaded from http://mnras.oxfordjournals.org/ at Swinburne University of Technology on August 11, 2014

Despite its importance as environmental probe, we are far from having a comprehensive picture of how the H I content of galaxies varies as a function of the local density. This is in stark contrast with optical studies, where the availability of large photometric and spectroscopic data bases such as those assembled by the Sloan Digital Sky Survey (SDSS; York et al. 2000) and the Two-degree Field Galaxy Redshift Survey (Colless et al. 2001) has allowed us to quantify how the star formation properties of galaxies vary across all environments, from voids to clusters, and for different cosmic epochs (e.g. Balogh et al. 2004; Kauffmann et al. 2004; Cooper et al. 2006). The evidence based on such data sets suggests that the transformation from star forming to quiescent galaxies is a smooth function of density, and happens in great part outside clusters (e.g. Dressler 1980; Lewis et al. 2002; Gómez et al. 2003; Blanton & Moustakas 2009). Surprisingly enough, we have not pinned down the mechanisms that drive this decrease in star formation rate, and whether this is accompanied/triggered by gas removal. This is due to a lack of H I observations covering a large enough range of environments to sufficient depth.

Environmental H I studies to date concentrated on the difference between cluster and field populations, and demonstrated that galaxies in high-density regions are H I deficient compared to isolated objects with similar size and stellar morphology (Giovanelli & Haynes 1985; Solanes et al. 2001). Resolved H I maps of galaxies in the Virgo and Coma clusters clearly show that H I is removed from the star-forming disc (Gavazzi 1989; Cayatte et al. 1990; Bravo-Alfaro et al. 2000; Kenney, van Gorkom & Vollmer 2004; Chung et al. 2009), mainly due to ram pressure stripping by the dense intracluster medium through which galaxies move (Gunn & Gott 1972; Vollmer 2009; Boselli & Gavazzi 2006). What happens to the gas content in the lower density group environment, where ram pressure is thought to be inefficient, is still unclear. Several studies have mapped the H I content of galaxies in groups, and found examples of H I-deficient galaxies (e.g. Huchtmeier 1997; Verdes-Montenegro et al. 2001; Kilborn et al. 2009). Tidal interactions in groups might funnel gas in the central regions of galaxies and increase their star formation (Iono, Yun & Mihos 2004; Kewley, Geller & Barton 2006), eventually reducing their H I content, but the net effect on statistical basis is unknown.

Because of limitations in the current H I samples, which target a limited range of environmental densities, with largely different selection criteria, H I sensitivities and multiwavelength coverage, we still do not know at which density scale the environment starts affecting the gas content of galaxies. In order to quantify the effect of environment on the H I reservoir of galaxies, we need wide-area surveys over large enough volumes to sample a variety of environments, and deep enough to probe the H I-poor regime. Accompanying multiwavelength information is essential not only to determine the environmental density, but also to provide measurements of the structural and star formation properties of the galaxies, which are necessary to connect the fate of the gas to that of the stars. In particular, because star formation and galaxy properties are known to scale primarily with mass (e.g. Kauffmann et al. 2003; Shen et al. 2003; Baldry et al. 2004), environmental comparisons must be done at fixed stellar mass.

H I-blind surveys such as the ongoing Arecibo Legacy Fast ALFA (ALFALFA; Giovanelli et al. 2005) survey map large volumes, but are not sensitive enough to detect H I-poor systems beyond the very local Universe (Gavazzi et al. 2013). However, the availability of high-quality H I spectra for galaxies that are individually not detected can offer important constraints on the average gas content of galaxies, when these are binned according to a given property and co-added or 'stacked' (e.g. Fabello et al. 2011a,b). Indeed, statistical analyses based on stacking of optically selected galaxies in the ALFALFA data cubes have already provided interesting insights into the average H I content of nearby massive galaxies in groups. Fabello et al. (2012) found that the average H I gas mass fraction declines with environmental density, and that such decline is stronger than what is observed for the mean global and central specific star formation rates. By comparing the observed trends with the results of semi-analytic models, they concluded that ram pressure stripping is likely to become effective in groups.

In this work, we use deep H I observations of optically selected galaxies from the recently completed *GALEX* Arecibo SDSS Survey (GASS; Catinella et al. 2010, hereafter DR1) to investigate the effects of the environment on a galaxy-by-galaxy basis. GASS includes H I measurements for ~800 galaxies with stellar masses greater than 10^{10} $M_{\odot}$ and redshifts $0.025 < z < 0.05$. For these galaxies, we have homogeneous measurements of structural parameters from SDSS and ultraviolet (UV) photometry from *GALEX* (Martin et al. 2005) imaging. In addition to its clean selection criteria, GASS is unique for being gas fraction limited: we designed the survey to reach small limits of gas content at fixed stellar mass ($M_{\rm H\,I}/M_* \sim$ 2–5 per cent), therefore probing the H I-rich to H I-poor regime. Because there is no morphological or environmental selection, and our redshift cut spans a large volume (approximately corresponding to distances between 100 and 200 Mpc), GASS probes a variety of local densities to significant depth, and thus is ideally suited to investigate environmental effects on the gas content of massive galaxies.

This paper is organized as follows. We summarize our survey design and Arecibo observations in Section 2, and introduce our third and final data release, which includes new Arecibo observations for 250 galaxies, in Section 3 (the catalogues are in Appendix A). Sections 4 and 5 illustrate the H I properties of the full GASS sample and revisit the gas fraction scaling relations introduced in our earlier work. Section 6 briefly describes the group catalogue (based on SDSS) used to characterize the environment of GASS galaxies, and presents our results on the environmental analysis. Discussion and conclusions follow in Section 7. All the distance-dependent quantities in this work are computed assuming $\Omega = 0.3$, $\Lambda = 0.7$ and $H_0 = 70\,{\rm km\,s^{-1}\,Mpc^{-1}}$. AB magnitudes are used throughout the paper.

2 SAMPLE SELECTION, ARECIBO OBSERVATIONS AND DATA REDUCTION

Survey design, sample selection, Arecibo observations and data reduction are described in detail in our first two data release papers (DR1 and Catinella et al. 2012b, hereafter DR2); thus, we only provide a summary here, including relevant updates.

GASS was designed to measure the global H I properties of ~1000 galaxies, selected uniquely by their stellar mass ($10 < \log(M_*/{\rm M}_{\odot}) < 11.5$) and redshift ($0.025 < z < 0.05$). The galaxies are located within the intersection of the footprints of the SDSS primary spectroscopic survey, the *GALEX* Medium Imaging Survey and ALFALFA. We defined a GASS *parent sample*, based on SDSS DR6 (Adelman-McCarthy et al. 2008) and the final ALFALFA footprint, which includes 12 006 galaxies that meet our survey criteria. The targets for 21cm observations were chosen by randomly selecting a subset of the parent sample which balanced the distribution across stellar mass and which maximized existing *GALEX* exposure time.

Downloaded from http://mnras.oxfordjournals.org/ at Swinburne University of Technology on August 11, 2014

We observed the galaxies with the Arecibo radio telescope until we detected them or until we reached a limit of a few per cent in gas mass fraction (defined as $M_{\rm H\,I}/M_*$ in this work). Practically, we set a limit of $M_{\rm H\,I}/M_* > 0.015$ for galaxies with $\log(M_*/{\rm M}_\odot) > 10.5$, and a constant gas mass limit $\log(M_{\rm H\,I}/{\rm M}_\odot) = 8.7$ for galaxies with smaller stellar masses. This corresponds to a gas fraction limit 0.015−0.05 for the whole sample. Given the H I mass limit assigned to each galaxy (set by its gas fraction limit and stellar mass), we computed the observing time, $T_{\rm max}$, required to reach that value with our observing mode and instrumental setup. We excluded from our sample any galaxies requiring more than 3 h of total integration time[1] (this effectively behaves like a redshift cut at the lowest stellar masses). Galaxies with good H I detections already available from ALFALFA and/or the Cornell H I digital archive (Springob et al. 2005, hereafter S05) were not re-observed. These H I-rich galaxies are added back to the GASS observations to make the *representative* sample (see Section 4).

GASS observations started in 2008 March and ended in 2012 July. The total telescope time allocation was 1005 h, of which ∼11 per cent unusable due to radio frequency interference (RFI) or other technical problems. This third and final data release includes the observations carried out after 2011 March 1 (420 h divided into 117 runs).

The Arecibo observations were carried out remotely in standard position-switching mode, using the *L*-band wide receiver and the interim correlator as a backend. Two correlator boards with 12.5 MHz bandwidth, one polarization, and 2048 channels per spectrum (yielding a velocity resolution of 1.4 km s^{-1} at 1370 MHz before smoothing) were centred at or near the frequency corresponding to the SDSS redshift of the target. We recorded the spectra every second with 9-level sampling.

The data reduction, performed in the IDL environment, includes Hanning smoothing, bandpass subtraction, RFI excision and flux calibration. The spectra obtained from each on/off pair are weighted by 1/rms^2, where rms is the root-mean-square noise measured in the signal-free portion of the spectrum, and co-added. The two orthogonal linear polarizations (kept separated up to this point) are averaged to produce the final spectrum, which is boxcar smoothed, baseline subtracted and measured as explained in the DR1 paper. The instrumental broadening correction for the velocity widths is described in the DR2 paper (we revised it after DR1, as discussed in Catinella et al. 2012a).

3 DATA RELEASE

This data release is incremental over DR1 and DR2, and includes new Arecibo observations of 250 galaxies. The catalogues of optical, UV and 21 cm parameters for these objects are presented in Appendix A.

All the optical parameters were obtained from the SDSS DR7 data base server.[2] Stellar masses are from the Max Planck Institute for Astrophysics (MPA)/Johns Hopkins University (JHU) value-added catalogues based on SDSS DR6, and assume a Chabrier (2003) initial mass function.

The *GALEX* UV photometry for our sample was reprocessed by us, as explained in Wang et al. (2010) and summarized in the DR1 paper. Briefly, we produced NUV−*r* images by registering *GALEX* and SDSS frames, and convolving the latter to the UV point spread function. The measured NUV−*r* colours are corrected for Galactic extinction only; we do not apply internal dust attenuation corrections.

The catalogues presented in our three releases are available on the GASS website,[3] along with all the H I spectra in digital format.

4 GASS SAMPLE PROPERTIES

The three GASS data releases combined include 666 galaxies, of which 379 are H I detections and 287 are non-detections. We refer to this as the GASS *observed* sample. Because we did not reobserve galaxies with good H I detections already available from either ALFALFA or the S05 archive, this sample lacks the most gas-rich objects, which need to be added back in the correct proportions. By following the procedure described in the DR1 paper, we obtained a sample that includes 760 galaxies (of which 473 are detections) and that is representative in terms of H I properties. We refer to this as the GASS *representative* sample. Note that, because of the improved statistics compared to DR1, here we use only one such representative sample (as opposed to a suite of 100 realizations with different sets of randomly selected gas-rich galaxies added to the GASS observations).

The H I properties of the detected galaxies are illustrated in Fig. 1 for both observed (solid histograms) and representative (dotted) samples. The blue histogram in the top-left panel shows the redshift distribution for the full GASS observed sample, using the SDSS redshifts for the non-detections (hatched green histogram). We note that H I detections and non-detections present a similar redshift distribution. As for our previous data releases, the distribution of corrected velocity widths (which have not been deprojected to edge-on view) peaks near 300 km s^{-1}, which is the value that we assume to compute upper limits for the H I masses of the non-detections, and to estimate $T_{\rm max}$ in Table A1. The bottom-left panel shows the stellar mass distribution for the observed and representative samples. The corresponding distribution for the non-detections is shown as a hatched green histogram (as for the redshift distribution, the detections are plotted on top of the non-detections). The stellar mass histogram is almost flat by survey design, as we wish to obtain similar statistics in each bin in order to perform comparisons at fixed stellar mass. As already noted in the DR1 and DR2 papers, non-detections span the entire range of stellar masses, but they are concentrated in the red portion of the NUV−*r* space (not shown). The detection fraction, i.e. the ratio of detected galaxies to total, is plotted as a function of stellar mass in the bottom-right panel. The detection fraction is close to 70 per cent for $M_* < 10^{10.7}\,{\rm M}_\odot$, and drops to ∼40 per cent in the highest stellar mass bin.

5 GAS FRACTION SCALING RELATIONS

In this section, we present the final version of the scaling relations introduced in the DR1 paper, now based on the full GASS sample. Here and in the rest of this work, we use the representative sample for our analysis (unless explicitly noted).

Clockwise from the top left, Fig. 2 shows how the gas mass fraction $M_{\rm H\,I}/M_*$ depends on stellar mass, stellar mass surface density (defined as $\mu_* = M_*/(2\pi R_{50,z}^2)$, where $R_{50,\,z}$ is the radius

[1] There are a few exceptions (5 per cent of the sample), represented by galaxies added for our initial pilot observations or already observed by one of our follow-up programmes with the *Hubble Space Telescope* or other facilities (Moran et al. 2012; Saintonge et al. 2011).

[2] http://cas.sdss.org/dr7/en/tools/search/sql.asp

[3] http://www.mpa-garching.mpg.de/GASS/data.php

Downloaded from http://mnras.oxfordjournals.org/ at Swinburne University of Technology on August 11, 2014

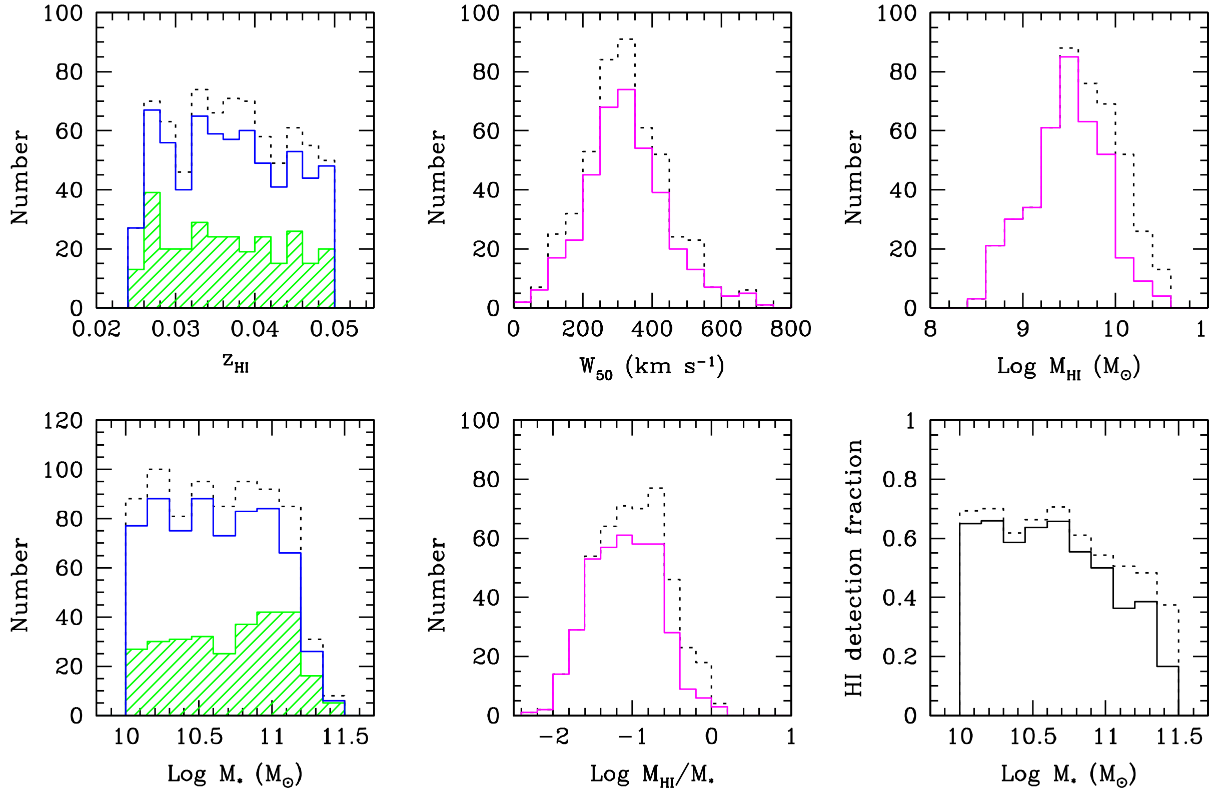

Figure 1. GASS sample properties. Top row: distributions of H I redshifts, velocity widths (not corrected for inclination) and H I masses for the Arecibo detections (magenta histograms). The green hatched histogram in the left-hand panel shows the distribution of SDSS redshifts for the non-detections (the blue histogram includes both detections and non-detections). Bottom row: distributions of stellar mass (same colour scheme as top-left panel), gas fraction and detection fraction (i.e. the ratio of detections to total) as a function of stellar mass. The dotted histograms in all panels correspond to the representative sample, which includes gas-rich objects from ALFALFA and/or S05 archive (see the text).

containing 50 per cent of the Petrosian flux in the z-band, expressed in kpc units), observed NUV$-r$ colour and R_{90}/R_{50} concentration index (a proxy for bulge-to-total ratio). Small grey circles and green upside-down triangles indicate H I detections and non-detections (plotted at their upper limits), respectively. The average values of the gas fraction are overplotted as filled circles; these are computed including the non-detections, whose H I masses were set either to their upper limits (green) or to zero (red). The averages are weighted in order to compensate for the flat stellar mass distribution of the GASS sample, using the volume-limited parent sample as a reference. Briefly, we binned both parent and representative samples by stellar mass (with a 0.2 dex step), and used the ratio between the two histograms as a weight. Error bars indicate the standard deviation of the weighted averages. These results are entirely consistent with our previous findings (see also Cortese et al. 2011 and Fabello et al. 2011a). In summary:

(i) The gas fraction of massive galaxies anticorrelates with all the quantities shown in Fig. 2. The tightest correlations are with observed NUV$-r$ colour (Pearson correlation coefficient $r = -0.69$) and stellar mass surface density ($r = -0.56$), and the weakest ones are with stellar mass ($r = -0.44$) and concentration index ($r = -0.38$).

(ii) The non-detections are almost exclusively found at stellar mass surface densities $\mu_* > 10^{8.5}\,\mathrm{M}_\odot\ \mathrm{kpc}^{-2}$ and NUV$-r > 4.5$ mag. The average gas fractions are insensitive to the way we treat the non-detections, except for the very most massive, dense and red galaxies.

We chose to compute averages of the linear gas fractions and plot their logarithms because this allows us to bracket the possible H I masses of the non-detections (between zero and their upper limits). However, as noted by Cortese et al. (2011), the distribution of H I gas fraction is closer to lognormal than Gaussian, hence averaging the logarithms seems more appropriate. In this case, we can only set the non-detections to their upper limits, and the resulting weighted averages of the logarithmic gas fractions are plotted in Fig. 2 as empty green circles. These are systematically smaller than the averages of the linear gas fractions (filled green circles), and the difference is larger for the stellar mass and concentration index relations, which are also the most scattered. The values of the weighted average gas fractions shown in this figure are listed in Table 1 for reference.

In our past work, we introduced the *gas fraction plane*, a relation between gas mass fraction and a linear combination of NUV$-r$ colour (which is a proxy for star formation rate per unit stellar mass) and stellar mass surface density, which can be used to define what is 'H I normality' for local massive, star-forming galaxies. The plane is obtained by fitting only the H I detections and minimizing the scatter on the y-coordinate (thus, it is equivalent to a direct fit). As demonstrated by Cortese et al. (2011), the distance from the plane along the y-axis strongly correlates with the H I deficiency parameter (Haynes & Giovanelli 1984) and has a similar scatter (naturally, the sample used to define the plane should be representative of unperturbed systems). This makes the gas fraction plane a very useful tool to investigate environmental effects and to identify unusually H I-rich

Downloaded from http://mnras.oxfordjournals.org/ at Swinburne University of Technology on August 11, 2014

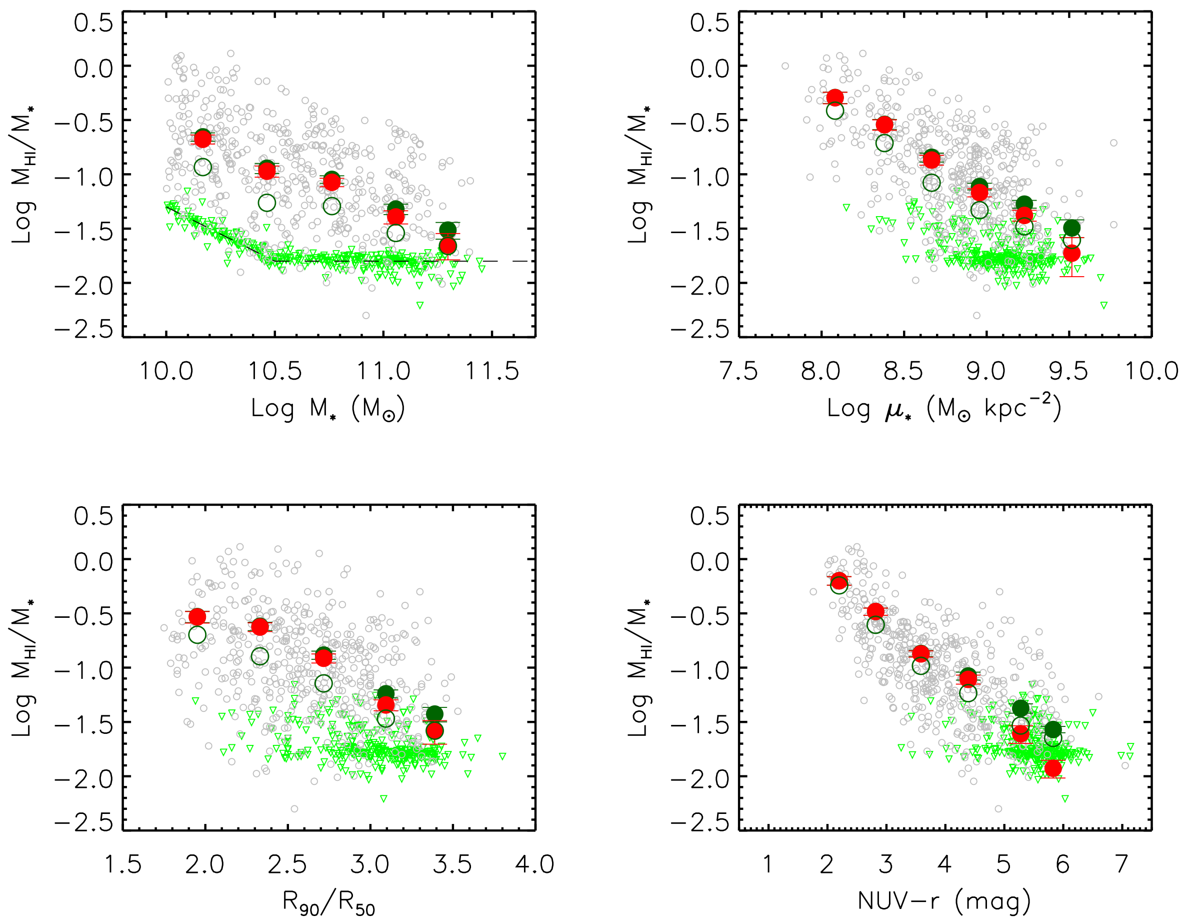

Figure 2. Average trends of H I mass fraction as a function of stellar mass, stellar mass surface density, concentration index and observed NUV−r colour for the representative sample. In each panel, large filled circles indicate weighted average gas fractions (see the text). These were computed including the non-detections, whose H I mass was set to either its upper limit (green) or to zero (red). Large empty circles indicate weighted averages of the logarithms of the gas fractions. Only bins including at least 10 galaxies are shown. These results are listed in Table 1. Small grey circles and green upside-down triangles indicate individual H I detections and non-detections (plotted at their upper limits), respectively. The dashed line in the top-left panel shows the H I gas fraction limit of GASS.

galaxies, especially when an accurate morphological classification is not available.

We plot the gas fraction plane in Fig. 3(a). We refined our sample by excluding galaxies for which confusion within the Arecibo beam is certain (because their measured H I flux belongs entirely or for the most part to a companion galaxy; these objects are marked as blue stars) and galaxies with measured gas fractions below our survey limit[4] (squares). For comparison, we also show the full set of ALFALFA galaxies meeting GASS selection criteria that have been catalogued to date (Haynes et al. 2011, grey dots), and that comprise the most H I-rich systems in the GASS volume. The coefficients of the gas fraction plane are noted on the x-axis of the figure. These have slightly changed with respect to the DR2 version (log $M_{\rm H\,I}/M_* = -0.338$ log μ_* -0.235 NUV−r + 2.908), but the two solutions are entirely consistent: the mean difference between the two gas fraction predictions is −0.023 dex, with a standard deviation of 0.027 dex. The rms scatter of the plane in log $M_{\rm H\,I}/M_*$ is now 0.292 dex (it was 0.319 dex for DR2).

As discussed in the DR2 paper, the validity of the gas fraction plane breaks down in the region where the contribution of the H I non-detections (which are excluded from the sample used to define it) becomes significant. Therefore, we computed another gas fraction plane relation using only galaxies with NUV $- r \leq 4.5$ mag, which is presented in Fig. 3(b). Over its interval of validity, this relation has slightly smaller scatter (0.281 dex) than our original plane in (a). The relation in (b) should be preferred to predict gas fractions of massive galaxies on the star-forming sequence. In any other case, we recommend to use the relation in (a) because it is based on the full sample of detections, rather than on a subset, and spans the entire range of NUV−r colours and stellar mass surface densities covered by massive galaxies.

In summary, the average scaling relations have not significantly changed with respect to our previous data releases, except for the fact that the error bars are of course smaller. However, we can now take advantage of our increased statistics to investigate second-order effects, such as the dependence of the gas content on the environment *at fixed stellar mass*, which would not be feasible without the full survey sample.

[4] Fig. 2 (top-left panel) shows a few H I detections below the nominal gas fraction limit of GASS (dashed line). As explained in the DR1 paper (footnote 6), the main reasons for this are that (i) the expected gas fraction limit assumes a 5σ signal with velocity width of 300 km s^{-1} (hence galaxies with smaller widths and/or face-on might be detected with higher signal to noise) and (ii) we never integrate less than 4 min (but, at large stellar masses, the gas fraction limit can be reached in as little as 1 min).

Downloaded from http://mnras.oxfordjournals.org/ at Swinburne University of Technology on August 11, 2014

Table 1. Weighted average gas fractions.

x	$\langle x \rangle$	$\langle M_{\rm H\,I}/M_* \rangle^a$	$\langle M_{\rm H\,I}/M_* \rangle^b$	$\langle \log(M_{\rm H\,I}/M_*) \rangle^c$	N^d
Log M_*	10.17	0.221 ± 0.020	0.210 ± 0.020	−0.934	188
	10.46	0.114 ± 0.012	0.107 ± 0.013	−1.262	176
	10.76	0.090 ± 0.007	0.084 ± 0.008	−1.293	180
	11.06	0.048 ± 0.005	0.041 ± 0.006	−1.540	177
	11.30	0.031 ± 0.005	0.022 ± 0.006	−1.660	39
Log μ_*	8.08	0.509 ± 0.061	0.508 ± 0.062	−0.414	32
	8.38	0.289 ± 0.031	0.286 ± 0.031	−0.712	69
	8.67	0.143 ± 0.014	0.135 ± 0.014	−1.078	145
	8.96	0.077 ± 0.005	0.068 ± 0.006	−1.330	268
	9.23	0.053 ± 0.004	0.042 ± 0.005	−1.480	218
	9.52	0.032 ± 0.006	0.019 ± 0.007	−1.605	24
R_{90}/R_{50}	1.95	0.295 ± 0.035	0.293 ± 0.036	−0.697	50
	2.33	0.240 ± 0.021	0.237 ± 0.022	−0.896	160
	2.72	0.131 ± 0.011	0.122 ± 0.012	−1.145	217
	3.09	0.057 ± 0.005	0.045 ± 0.005	−1.469	272
	3.39	0.037 ± 0.006	0.026 ± 0.006	−1.580	60
NUV−r	2.20	0.632 ± 0.057	0.632 ± 0.057	−0.242	24
	2.82	0.329 ± 0.025	0.329 ± 0.025	−0.605	108
	3.59	0.135 ± 0.009	0.134 ± 0.009	−0.983	139
	4.39	0.084 ± 0.007	0.078 ± 0.007	−1.235	131
	5.28	0.042 ± 0.004	0.025 ± 0.005	−1.533	194
	5.83	0.027 ± 0.002	0.012 ± 0.002	−1.648	145

Notes. [a]Gas fraction weighted average; H I mass of non-detections set to upper limit. [b]Gas fraction weighted average; H I mass of non-detections set to zero. [c]Weighted average of logarithm of gas fraction; H I mass of non-detections set to upper limit. [d]Number of galaxies in the bin.

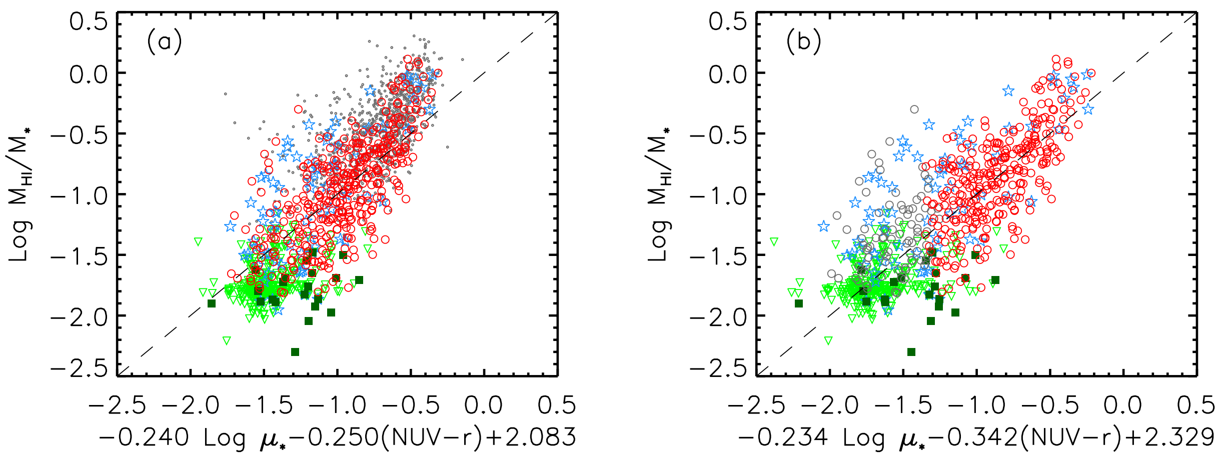

Figure 3. Gas fraction plane, a relation between H I mass fraction and a linear combination of stellar mass surface density and observed NUV−r colour. (*a*) Relation obtained using all the H I detections in the GASS representative sample (red circles) that are not confused (blue stars) or below the nominal gas fraction limit of GASS (dark green squares). Green upside-down triangles are non-detections, and galaxies meeting GASS selection criteria that have been catalogued by ALFALFA to date are shown as grey dots. (*b*) Relation obtained using only the subset of detected galaxies with NUV − $r \leq 4.5$ mag (red circles). Grey circles indicate the remaining H I detections; green and blue symbols are as in (a).

6 EFFECT OF ENVIRONMENT ON THE GAS CONTENT OF MASSIVE GALAXIES

6.1 Group catalogue and halo masses

Here, we describe briefly the group catalogue that we used to characterize the environment of GASS galaxies.

Yang et al. (2007) compiled a catalogue of galaxy groups based on SDSS DR4, using what they refer to as a halo-based group finder. Their algorithm is iterative and includes the following steps: (a) identify potential group centres using two methods; (b) compute the characteristic luminosity of each tentative group (i.e. the combined luminosity of all group members brighter than a threshold); (c) estimate the mass, size and velocity dispersion of the dark matter halo associated with it (initially using a constant mass-to-light ratio for all groups); (d) reassign galaxies to each tentative group based on its halo properties; (e) recompute group centres and iterate until there is no further change in the group memberships.

Once the group catalogue was finalized, Yang et al. (2007) assigned halo masses via abundance matching, assuming the halo mass function of Warren et al. (2006). In practice, they associated the characteristic luminosity or stellar mass of a group to a halo mass by matching their rank orders.

Downloaded from http://mnras.oxfordjournals.org/ at Swinburne University of Technology on August 11, 2014

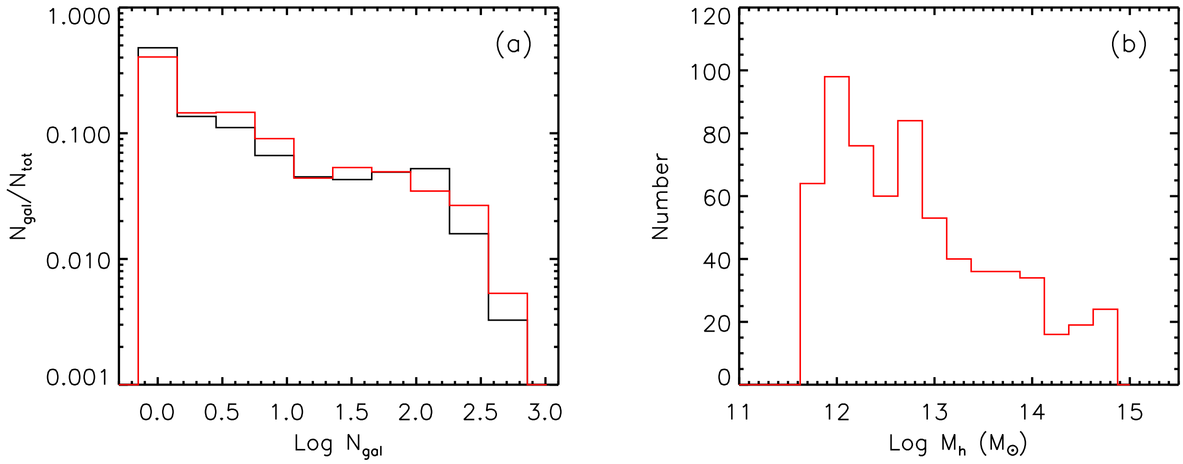

Figure 4. (a) Normalized distribution of N_{gal}, the number of galaxies in each group, for the GASS parent and representative samples (black and red, respectively; see the text). (b) Distribution of halo masses for the representative sample. This histogram does not include 110 galaxies in very small groups that do not have halo masses assigned in the group catalogue.

They applied the same algorithm to SDSS DR7 (Yang et al. 2012) and generated two sets of group catalogues,[5] one based on Petrosian magnitudes and one based on model magnitudes. We use the latter for our environmental analysis and adopt halo masses M_h obtained by rank ordering the groups by stellar mass, following e.g. Woo et al. (2013). The catalogue also classifies galaxies as centrals or satellites.

We note that 10 out of 760 galaxies in our GASS representative sample are not included in the group catalogue and are thus excluded from our environmental analysis. Lastly, very small groups are not assigned halo masses in the group catalogue, and this affects 110 of the remaining galaxies. However, this is not an issue for our analysis, as we will divide our sample into three intervals of halo mass, and include those 110 galaxies in the lowest M_h bin ($\log M_h/M_\odot < 12$).

6.2 The environment of GASS galaxies

We begin our analysis by asking what are the typical environments probed by the GASS galaxies. In order to establish this, we cross-matched both our parent and representative samples with the galaxies in the group catalogue described above. We remind the reader that the parent sample is the superset of all the 12 006 galaxies in SDSS DR6 that meet the GASS selection criteria (stellar mass, redshift cuts and located within the final ALFALFA footprint), out of which we extracted those that we observed with Arecibo. As such, the parent sample is volume limited and reasonably complete in stellar mass above 10^{10} $M_\odot$ (aside from SDSS fibre collision issues).

We plot the normalized distribution of N_{gal}, the number galaxies in each group, in Fig. 4(a), for both parent (black) and GASS (red) samples. Galaxies with $N_{gal} = 1$ are isolated, and we generically call ‘group’ any structure with two or more members. According to this definition, about half of the GASS parent sample galaxies are isolated (48 per cent; the percentage is 43 per cent for the representative sample) and about half are in groups. The richest structure in our survey volume is represented by the far outskirts of the Coma cluster (with $N_{gal} = 623$; with a median redshift of 0.0229, the centre of Coma is just below our redshift cutoff). Compared with the parent sample, the GASS sample probes the same environments in terms of group richness. The distribution of halo masses for the GASS sample is shown in panel (b); the 110 galaxies in small groups mentioned above, which do not have halo masses assigned in the group catalogue, are not plotted. As a result of our survey strategy (specifically, the fact that we selected a set of galaxies that balanced the distribution across stellar mass), this histogram is less peaked at low M_h than the corresponding one for the parent sample (not shown), but most importantly the two samples span the same interval of halo mass.

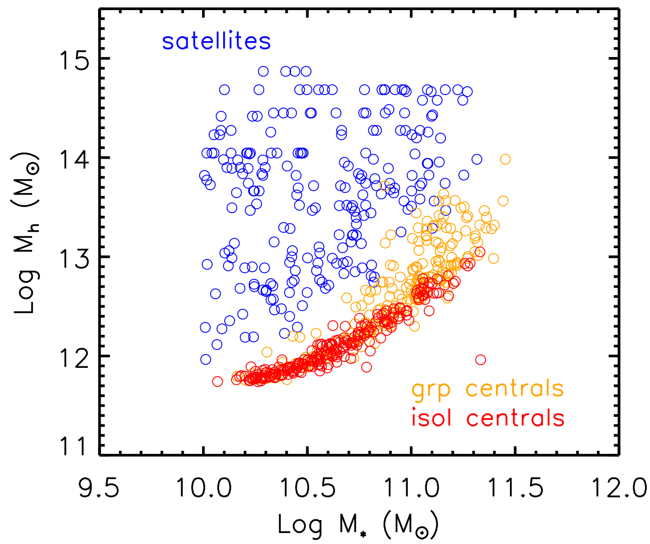

Figure 5. Relation between halo and stellar masses for central galaxies in isolation (red circles) or in groups (orange) and for satellite galaxies (blue) in the GASS sample.

Lastly, Fig. 5 shows the relation between stellar and halo masses for the galaxies in our sample with assigned halo mass; we colour-coded the points to indicate central galaxies in isolation (red) or in groups (orange) and satellites (blue). Our sample does not include central galaxies in the most massive haloes, because such systems are rare.

Having established that the GASS sample is representative of the parent sample also in terms of environment, it is important

[5] Available at http://gax.shao.ac.cn/data/Group.html.

Downloaded from http://mnras.oxfordjournals.org/ at Swinburne University of Technology on August 11, 2014

to note that our survey only probes low- to intermediate-density environments (as we discuss later, our most massive halo bin is dominated in number by groups with an average of 20 members). There are no rich clusters, such as Virgo or Coma, in our survey volume. Both the limited dynamic range in galaxy density and our relatively high gas fraction limit (see below) do not allow us to investigate the most dramatic cases of H I stripping, which are well known to occur in the central regions of clusters and rich groups (Cayatte et al. 1990; Bravo-Alfaro et al. 2000; Boselli & Gavazzi 2006). The reader should bear this in mind when interpreting our results in the following sections. Instead, GASS is optimally suited to look for evidence of quenching mechanisms acting on the H I and stellar content of massive galaxies *in the group environment* and from a statistical point of view.

6.3 Quantifying the suppression of H I gas

If environmental mechanisms play an important role in removing cold gas from galaxies, it is reasonable to expect that the H I content of the affected galaxies will be lower than that of similar (in terms of structural and star formation properties), but unperturbed, systems. This idea is behind the definition of the classic 'H I deficiency' parameter (Haynes & Giovanelli 1984), which has been successfully used to demonstrate that galaxies in the densest environments have their H I gas content largely reduced, most likely by ram pressure stripping by the dense intracluster medium (Giovanelli & Haynes 1985; Solanes et al. 2001; Chung et al. 2007; Vollmer 2009; Cortese et al. 2011).

As mentioned in Section 5, the gas fraction plane is an excellent tool to investigate environmental effects, and the distance from the best-fitting relation has been shown to be equivalent to the H I deficiency for galaxies in the Virgo cluster (Cortese et al. 2011). Indeed, the plane is a reformulation of the H I deficiency relation in terms of quantities (stellar mass surface density and NUV−*r* colour, which is a proxy for the specific star formation rate) that have a more immediate physical interpretation (compared to morphological classification and optical diameter) and are more easily applicable to large, modern data sets. However, we show below that GASS does not probe the H I-deficient regime; hence, the gas fraction plane is of limited use to find evidence for gas suppression *within our own sample*.

We measured the 'H I richness' parameter for our galaxies, defined as the difference between the logarithms of the measured gas fraction and that predicted by the relation in Fig. 3(a). H I-poor galaxies have smaller gas fractions than predicted, i.e. a negative H I richness. Fig. 6(a) shows the distribution of the H I richness parameter for H I-detected galaxies in three bins of halo mass, as indicated on the top left; panel (b) shows the same histograms for the non-detections. These distributions clearly illustrate that the non-detections pile up at H I richness between −0.5 and −0.2, but they start to be important already in the 'H I-normal' regime, i.e. near H I richness of zero. Keeping in mind that the scatter of the plane is 0.3 dex, only galaxies with gas fractions that deviate from the predicted values by at least that amount (or more conservatively 0.5 dex, as usually assumed for the H I deficiency parameter) should be called H I-deficient (or H I-excess) systems. Thus, because our survey gas fraction limit is so close to the start of the H I-deficient regime, it turns out that the plane is much better suited to characterize the H I-excess systems in the GASS redshift interval than the H I-poor ones (since for the latter we only have upper limits).

The sample used to define the gas fraction plane is indeed representative of unperturbed systems, because it does not include the H I non-detections, which are the galaxies affected by the environment. We checked this by computing the gas fraction plane using only H I detections in the $M_{\rm h} < 10^{12}$ M$_{\odot}$ bin, which gives a solution that is indistinguishable from that in Fig. 3(a). The highest halo mass bin, $M_{\rm h} \geq 10^{13}$ M$_{\odot}$, includes only 70 detections, and although the corresponding gas fraction plane is slightly offset towards lower $M_{\rm HI}/M_*$ with respect to the 'undisturbed' one, the difference is statistically not significant (the mean difference between the two solutions is 0.17 dex, with a standard deviation of 0.08 dex, and the scatters of the planes are both 0.3 dex; see Fig. 6a).

Because we cannot quantify the degree of H I removal in individual H I-deficient systems at the distances probed by GASS, and also our statistics become limited when we start binning galaxies by stellar mass and environment, we do not attempt to compute the average gas fraction scaling relations presented in Fig. 2 in bins of environmental density (see however Section 7). This approach was adopted by Cortese et al. (2011) to compare Virgo cluster and H I-normal galaxies, and was successful because the more nearby Herschel Reference Survey (HRS; Boselli et al. 2010) sample includes H I detections and more stringent upper limits in the H I-deficient regime.

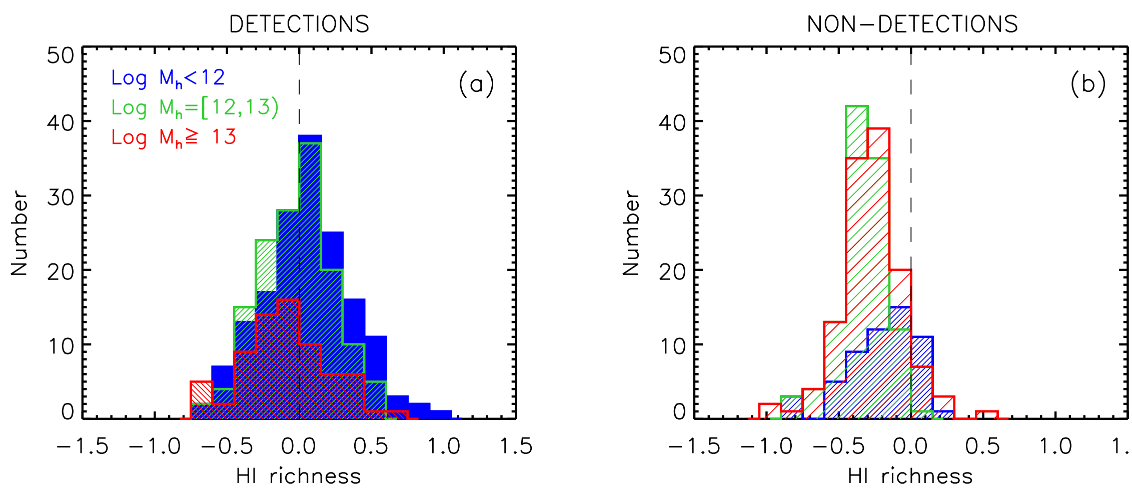

Figure 6. (*a*) Distribution of H I richness, i.e. the difference between measured and expected gas fractions, for H I-detected galaxies. The sample is divided into three bins of halo mass, as indicated in the top-left corner. (*b*) Same distributions for galaxies that were not detected in H I (plotted at their upper limits), together with detections below the gas fraction limit of GASS. The colors correspond to the same halo mass bins indicated on the top-left corner of (a).

Downloaded from http://mnras.oxfordjournals.org/ at Swinburne University of Technology on August 11, 2014

Instead, as already done by Kauffmann et al. (2012) for our sample, we adopt the gas fraction threshold of GASS as the nominal division between H I-normal and H I-deficient systems, and look for trends in the H I detection fractions as a function of galaxy properties and environment. As discussed above, this is entirely justified by the fact that the detection limit of GASS roughly corresponds to the gas fraction separating H I-normal from H I-deficient massive galaxies. In order to compute meaningful detection fractions, we excluded from our sample the objects for which confusion within the Arecibo beam is certain (15 per cent of the H I detections, indicated by blue stars in Fig. 3; these galaxies were not included in Fig. 6). Also, as already noted, the few H I detections with gas fraction below the GASS limit (dark green squares in Fig. 3) are effectively H I-poor systems, and thus are counted as non-detections.

6.4 Suppression of H I gas in the group environment

In this section, we investigate the relation between gas content and other galaxy properties in different environments, looking for possible evidence of gas removal at the highest densities. We use dark matter halo masses as our environmental estimator and, for the reasons explained above, we resort to using detection fractions to characterize the average gas content in a given bin of, e.g. stellar and halo mass.

Fig. 7 shows how the average H I detection fraction, i.e. the ratio of detections to total in each bin, $N_{\rm det}/N_{\rm tot}$, changes as a function of stellar mass, stellar mass surface density and concentration index in the first column, and NUV$-r$, $g-i$ colours in the second one. Blue and red circles indicate galaxies that inhabit dark matter haloes with masses below and above 10^{13} M$_\odot$, respectively. We initially divided our sample into the same three bins of halo mass used for Fig. 6, which contain similar numbers of galaxies (see also Fig. 4). We indicate the average detection fractions in the two lowest halo mass intervals, $\log M_{\rm h}/{\rm M}_\odot < 12$ and $12 \le \log M_{\rm h}/{\rm M}_\odot < 13$, with dashed purple and dot–dashed green lines, respectively. As can be seen, there is no significant difference between these two halo mass bins in any of these plots (the only apparent exception would be the first stellar mass bin in the top-left panel, but note that the green data point is based on 20 objects only), so we combined them to increase statistics.

The top-left panel of Fig. 7 is the main result of this work, and clearly shows that the H I content of massive galaxies that live in dark matter haloes with $M_{\rm h} \gtrsim 10^{13}$ M$_\odot$ is significantly reduced compared to that of galaxies *with the same stellar mass*, at least below $M_* \sim 10^{11}$ M$_\odot$. We do not see a difference at larger stellar mass, which seems to suggest that the environment has no detectable effect on the most massive galaxies in our sample. We will come back to this point later. Because GASS does not contain any very rich group or clusters (and indeed 2/3 of the haloes in our highest density bin have masses between 10^{13} and 10^{14} M$_\odot$; see also Fig. 4b), our result implies that *the suppression of H I is modulated by the environment even at the intermediate densities probed by our sample*.

The other two panels in the first column of Fig. 7 show that the suppression of H I gas in the most massive haloes in our sample can be seen also at fixed stellar mass surface density and concentration index, both proxies of stellar morphology (higher values of μ_* and R_{90}/R_{50} correspond to bulge-dominated systems).

The plots on the right-hand column of Fig. 7 compare the detection fractions in different environments at fixed galaxy colour. Interestingly, we find that galaxies in more massive haloes have lower gas content only for NUV$-r$ colours redder than $\sim$4 mag. In the stellar mass range probed by GASS, this colour corresponds to the red edge of the blue cloud and the start of the green valley (Wyder et al. 2007), suggesting that a fraction of our gas-poor systems have not yet completely stopped forming stars. The presence of gas-poor, but still star-forming, galaxies may indicate that the time-scale of the gas removal is significantly shorter than the time-scale necessary for the NUV$-r$ colour to reach values typical of the red sequence galaxies, i.e. NUV $- r \sim 5.5$ mag ($\sim$1 Gyr, see also fig. 4 in Cortese et al. 2011).

Less enlightening is the variation of H I detection fraction with $g-i$ colour. Although we find that, at fixed $g-i$ colour, galaxies in high-mass haloes have significantly lower detection fractions, this result does not provide any additional insights into the physical process at play. Indeed, massive galaxies generally lie on the optical red sequence regardless of their current star formation activity (Wyder et al. 2007; Cortese 2012), thus their optical colours are saturated – they cannot significantly redden following further quenching of the star formation.

We look in more detail at the properties of the lower stellar mass galaxies, for which we see a clear difference of gas content above and below $M_{\rm h} \sim 10^{13}$ M$_\odot$, in Fig. 8. Here, the detection fraction is shown as a function of stellar mass surface density, concentration index, NUV$-r$ and $g-i$ colours for the subset of galaxies with $M_* < 10^{10.75}$ M$_\odot$. For comparison, the same plots are presented in Fig. 9 for the galaxies with stellar mass above that limit. As expected, the offsets seen in Fig. 7 become larger when we restrict the sample to the lower stellar mass bin. This is particularly interesting in the case of the NUV$-r$, since it slightly reinforces our time-scale argument. Overall, the larger differences shown in Fig. 8 are simply due to the exclusion of the most massive galaxies, which have lower gas fractions (see Fig. 2). With regard to the galaxies with stellar mass $M_* \ge 10^{10.75}$ M$_\odot$, we caution the reader that the median galaxy is a non-detection, hence we cannot conclude that the environment is not acting on the gas reservoir of those systems – our survey might simply not be sensitive enough to detect environmental effects on these already gas-poor galaxies.

The trends in detection fraction observed when we divide the sample according to halo mass are present also when we describe the environment in terms of central and satellite galaxies. Fig. 10 repeats the panels of Fig. 7, but now blue and red circles represent central and satellite galaxies, respectively. Purple dashed and green dot–dashed lines indicate central galaxies in isolation and in groups, respectively. There is no significant difference between the two classes of central galaxies and, at fixed stellar mass (at least below $\sim 10^{11}$ M$_\odot$), satellite galaxies have lower gas content on average than centrals. This is completely consistent with the result shown in the corresponding panel of Fig. 7, as expected from the fact that central galaxies in this stellar mass interval are mostly isolated (see Fig. 5). Overall, the offsets in detection fraction are slightly smaller when we divide the sample into central and satellites rather than by halo mass (mostly because satellite galaxies are found at all halo masses, not only in haloes with $M_{\rm h} > 10^{13}$ M$_\odot$), but they are still significant.

It would be very interesting to know whether the observed decrease of H I content is primarily dependent on the dark matter halo mass or on the nature of the galaxy as central versus satellite. This is because there could be physically distinct processes that link H I content separately to these two different environmental descriptors (e.g. Weinmann et al. 2006). Unfortunately, our data do not allow us to disentangle between the two scenarios. As can be seen by simply drawing a horizontal line at $\log M_{\rm h}/{\rm M}_\odot = 13$ in Fig. 5, there are almost no central galaxies above that threshold and there are only

Downloaded from http://mnras.oxfordjournals.org/ at Swinburne University of Technology on August 11, 2014

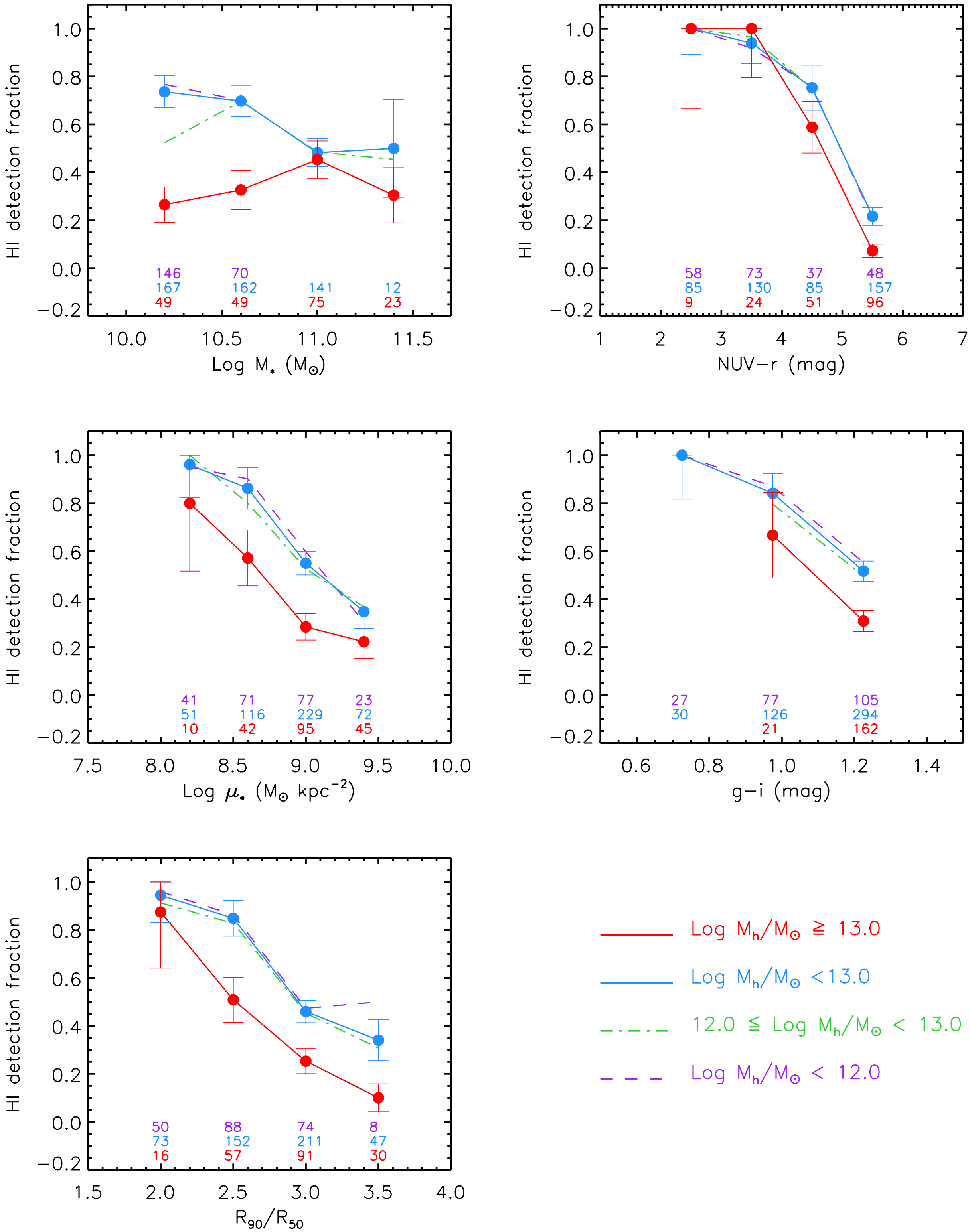

Figure 7. H I detection fraction of GASS galaxies plotted as a function of stellar mass, stellar mass surface density and concentration index in the first column, and NUV−r, $g-i$ colours in the second one. The data in each panel are divided into two bins of halo mass, below and above 10^{13} M$_\odot$ (blue and red, respectively), as indicated in the bottom right-hand corner of the figure. Large circles are average detection fractions, and the numbers in each panel indicate the total number of galaxies in each bin (only bins with $N_{\rm tot} \geq 5$ are shown); error bars are Poissonian (truncated at detection fraction of 1 if necessary). We also show the results for a finer division of the lowest halo mass interval, i.e. $\log M_{\rm h}/{\rm M}_\odot < 12$ (dashed purple line) and $12 \leq \log M_{\rm h}/{\rm M}_\odot < 13$ (dot–dashed green line). Note that haloes with $M_{\rm h} < 10^{12}$ M$_\odot$ are populated only by galaxies in the lowest two stellar mass bins.

Downloaded from http://mnras.oxfordjournals.org/ at Swinburne University of Technology on August 11, 2014

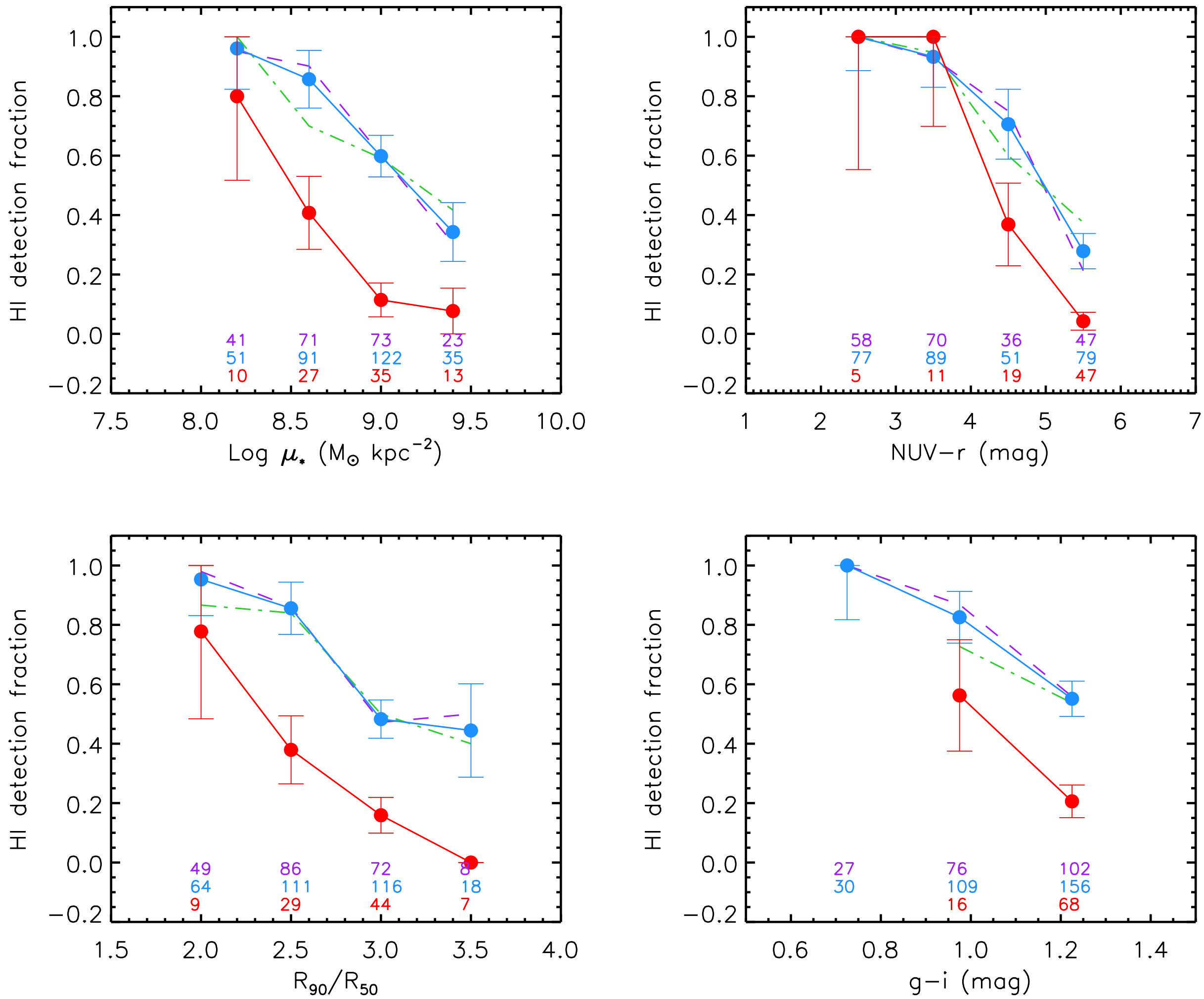

Figure 8. H I detection fraction plotted as a function of stellar mass surface density, concentration index, NUV−r and $g - i$ colours for the subset of galaxies with stellar mass $\log M_*/M_\odot < 10.75$. Symbols and colours are the same as in Fig. 7.

very few satellites below. Therefore, although splitting the sample by halo mass is not the same as splitting by centrals versus satellites, once we bin the galaxies to reach sufficient statistics the two classifications become almost the same, and the issue ends up being just a semantic one.

7 DISCUSSION AND CONCLUSIONS

In this work, we have used the full GASS data set, which includes H I measurements for ∼800 galaxies with stellar masses $10 < \log(M_*/M_\odot) < 11.5$ and redshift $0.025 < z < 0.05$, to study how the gas content of massive systems depends on environment *at fixed stellar mass*. We characterized the environment of GASS galaxies by their dark matter halo mass, obtained from the SDSS group catalogue of Yang et al. (2007, updated to SDSS DR7) using the abundance matching technique.

The key new result of our analysis is that we obtained clear evidence for suppression of H I gas at fixed stellar mass (at least below $M_* \sim 10^{11}\,M_\odot$) for galaxies that are located in groups with halo masses $M_h \gtrsim 10^{13}\,M_\odot$. The effect is seen also at fixed stellar morphology (i.e. μ_* and R_{90}/R_{50}) and when we divide our sample according to central/satellite classification. As shown in Fig. 4, our most massive halo bin is dominated by systems with M_h between 10^{13} and $10^{14}\,M_\odot$. In the SDSS group catalogue, such haloes include up to ∼60 members (20 on average), whereas smaller haloes include up to 10 members (2 on average). Thus, the environment where we detect a decrease of H I gas content in massive galaxies is that of moderately rich groups, and we are certainly not probing the cluster regime.

We attempt to quantify the amount of gas depletion for our sample in Fig. 11. We computed average gas fractions in bins of stellar and halo mass, including the non-detections at their upper limits. As in Figs 7–9, blue and red lines indicate dark matter haloes with masses below and above $10^{13}\,M_\odot$, respectively. The result is qualitatively consistent with what is shown in the top-left panel of Fig. 7 for the average detection fractions: at fixed stellar mass (at least below $\sim 10^{11}\,M_\odot$), the H I content of galaxies in more massive haloes is systematically lower. In the first two stellar mass bins, the difference of H I gas fractions between galaxies in haloes with masses below and above $10^{13}\,M_\odot$ is ∼0.4 dex (linear gas fractions drop from 12 to 5 per cent in the first M_* bin and from 6 to 3 per cent in the second one). As indicated by the red arrows, the average gas fractions for the $M_h \geq 10^{13}\,M_\odot$ bins (and those for $M_* \geq 10^{11}\,M_\odot$ regardless of halo mass) are dominated by non-detections, and thus must be considered upper limits. This gives us a lower limit on the

Downloaded from http://mnras.oxfordjournals.org/ at Swinburne University of Technology on August 11, 2014

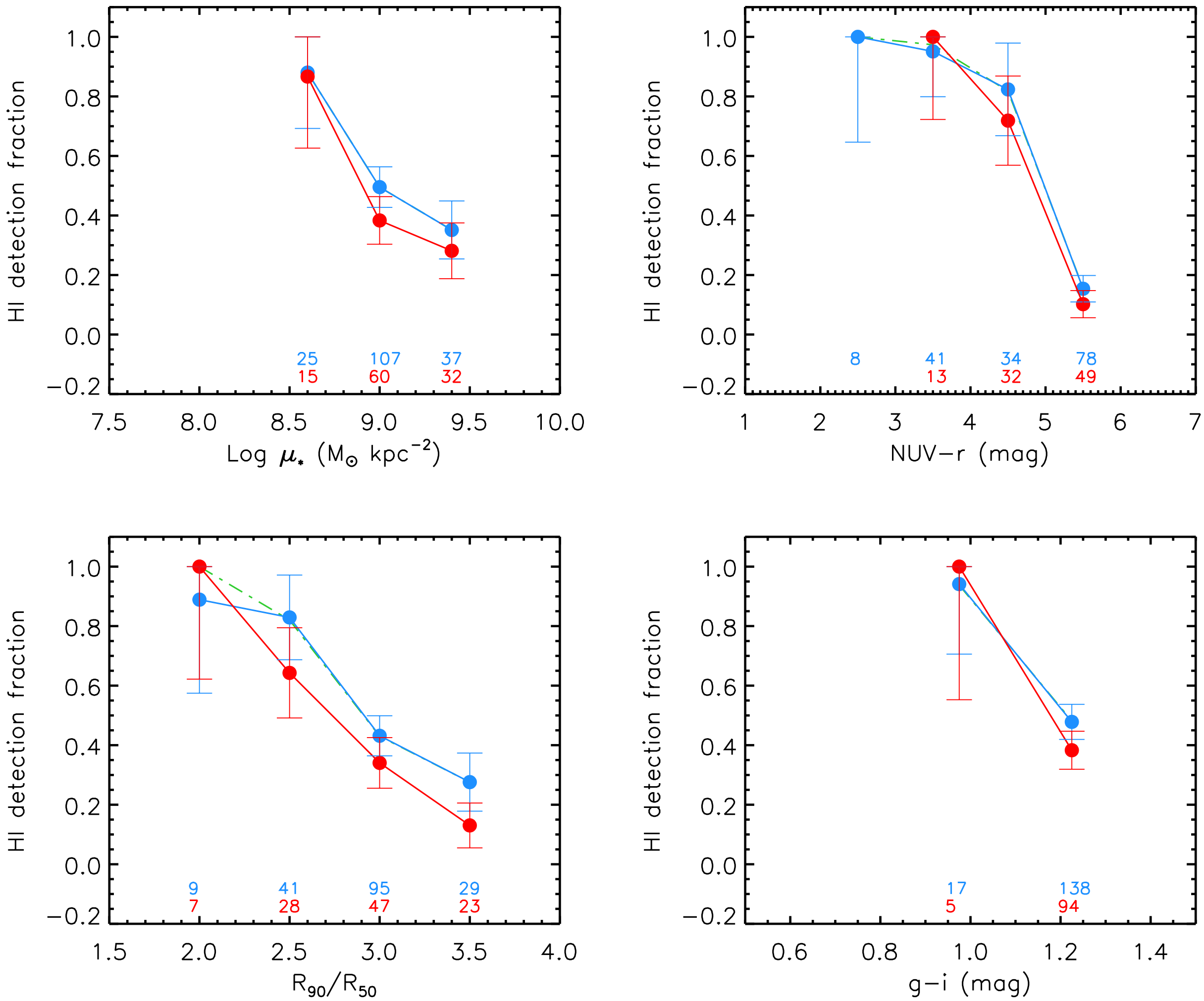

Figure 9. Same as Fig. 8 for galaxies with larger stellar mass ($\log M_*/M_\odot \geq 10.75$).

typical amount of H I suppression in groups, which is at least a factor of 2 compared to galaxies in smaller haloes, but prevents us from a more precise quantification. This is the reason why we decided to carry out our analysis in terms of detection fractions instead of gas fractions.

As expected, the decrease of H I content measured in the group environment for our sample, 0.4 dex, is smaller than what observed in higher density regions, such as rich galaxy clusters. For instance, H I-deficient Virgo members with stellar masses $\sim 10^{10}-10^{10.7}$ $M_\odot$ have gas fractions that are 0.8 dex smaller than H I-normal galaxies in the HRS (see table 1 in Cortese et al. 2011). Galaxies in more massive clusters such as Coma have more extreme levels of H I deficiency (Solanes et al. 2001).

It is interesting to determine whether the star formation properties of the galaxies for which H I has been reduced are affected as well. Fig. 12 shows the running averages of the specific star formation rates versus stellar mass for our sample, binned by halo mass as in Fig. 11. The star formation rates were computed from our near-ultraviolet (NUV) photometry as in Schiminovich et al. (2010). As for the gas, we see a quenching of the star formation in the group environment (at least for galaxies with stellar mass less than $\sim 10^{11}$ $M_\odot$). This is in qualitative agreement with optical studies, which established that the star formation properties of galaxies are affected by the environment well before reaching the high-density regimes that are typical of clusters (e.g. Lewis et al. 2002; Gómez et al. 2003). A detailed comparison with such studies is difficult, as sample selections and environmental descriptors vary widely, and we specifically targeted only massive galaxies.

We can think of two main scenarios to explain the observed suppression of H I content in group galaxies: direct removal of H I from the disc and starvation (Larson, Tinsley & Caldwell 1980). In the first case, the H I is directly affected and removed from the galaxy disc by one or more environmental mechanisms (e.g. ram pressure or gravitational interactions). In the second case, the lower H I mass fraction in the more massive haloes (and in satellites versus centrals) is due to the group environment disrupting the accretion of the infalling, pristine gas, which, if allowed to reach the galaxy disc, would subsequently replenish its H I reservoir. However, it seems unlikely that starvation alone could explain both the H I suppression and the difference of gas content at fixed specific star formation rate seen in our data. If the supply of infalling gas is stopped and no other external mechanisms are at play, then the H I in the galaxy will be consumed by star formation, and the two quantities should track each other and decrease on the same time-scale (Boselli et al. 2006; Cortese et al. 2011). Instead, Fig. 8 shows that, at fixed NUV−r colour (i.e. at fixed specific star formation rate), the H I content of galaxies in more massive haloes is systematically lower, at least in objects with stellar masses less than 10^{11} $M_\odot$. This supports a

Downloaded from http://mnras.oxfordjournals.org/ at Swinburne University of Technology on August 11, 2014

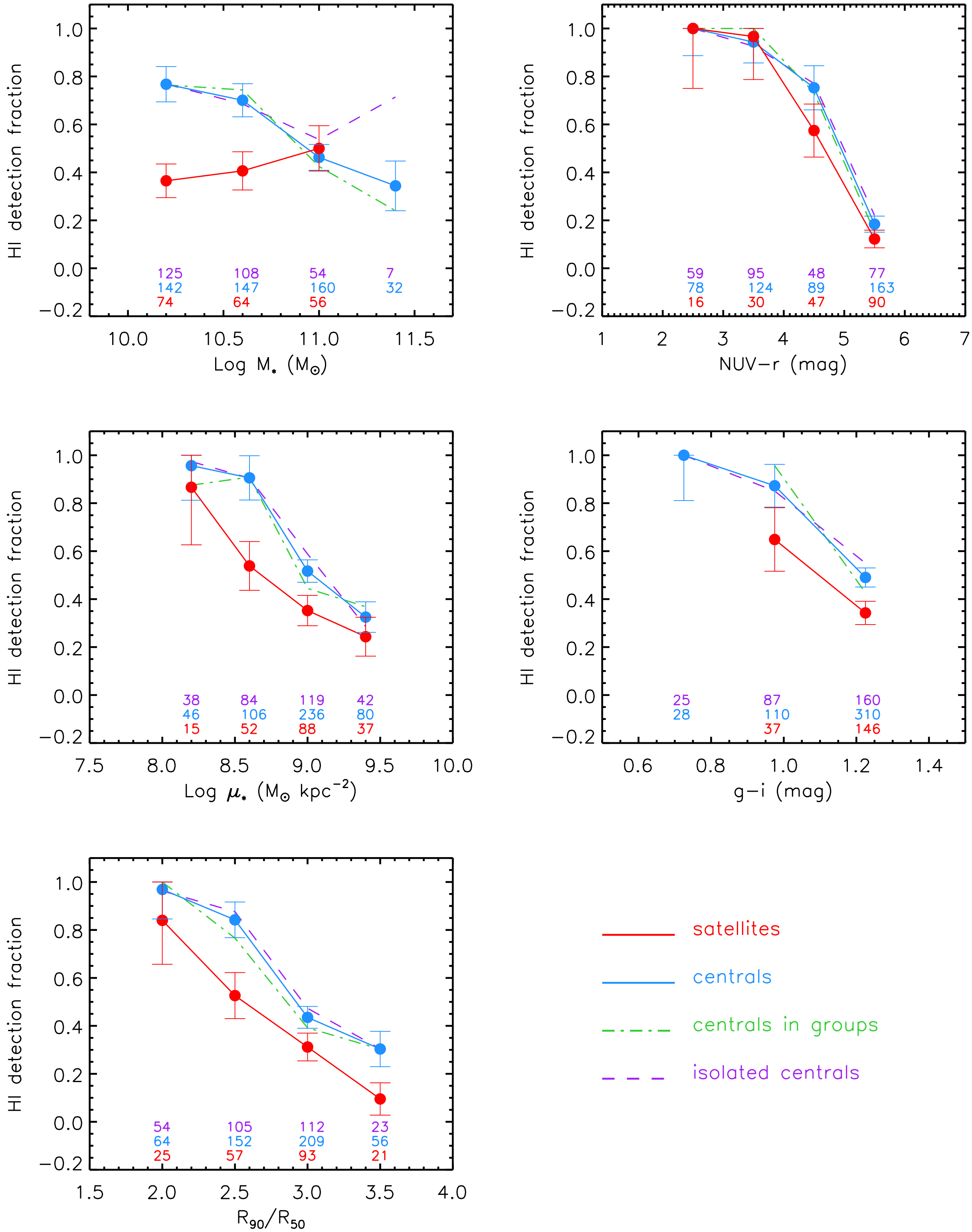

Figure 10. The H I detection fraction of GASS galaxies is plotted here as a function of the same quantities seen in Fig. 7, but now the data are divided into centrals (blue) and satellites (red). The purple dashed and green dot–dashed lines indicate central galaxies in isolation and in groups, respectively.

scenario in which an environmental mechanism acting directly on the cold gas reservoir is needed to explain our findings. We will assume that this is the case in the remainder of this section.

Without detailed information on the distribution and kinematics of the H I gas we cannot determine which environmental process is responsible for the H I removal, but we can try to establish if it acts outside-in by looking at the colour gradients of our galaxies. Indeed, Cortese et al. (2012) have recently shown that the extent of the star-forming disc and the shape of the colour gradients are tightly related to the amount of H I gas. Using $g - i$ colour gradients

Downloaded from http://mnras.oxfordjournals.org/ at Swinburne University of Technology on August 11, 2014

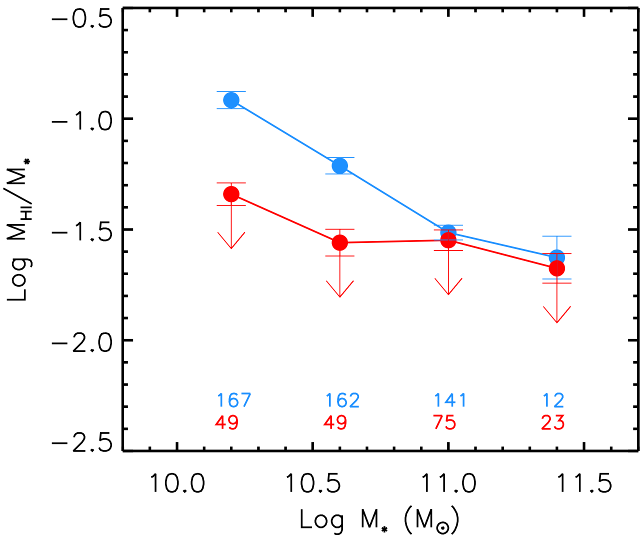

Figure 11. Averages of H I gas fraction logarithms versus stellar mass. The data are divided into two bins of halo mass, above and below 10^{13} $M_{\odot}$ (red and blue, respectively). Downward arrows indicate upper limits (because the corresponding bins are dominated by H I non-detections). The numbers at the bottom indicate the total number of galaxies in each bin (only bins with $N_{\rm tot} \geq 5$ are shown); error bars are errors on the mean.

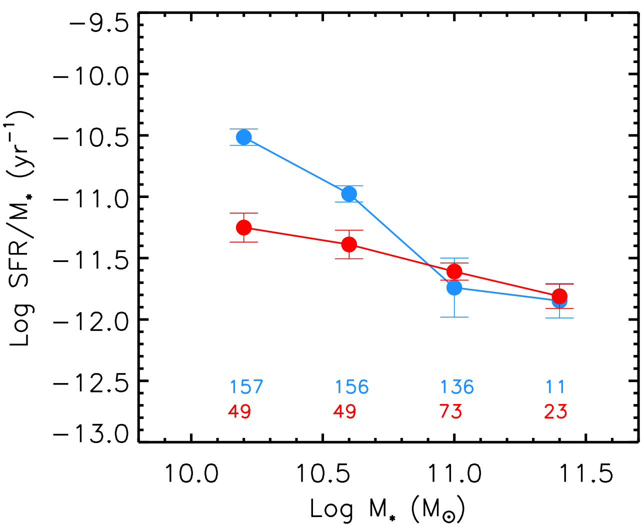

Figure 12. Average specific star formation rates are plotted as a function of stellar mass for two bins of halo mass (symbols and colours as in Fig. 11).

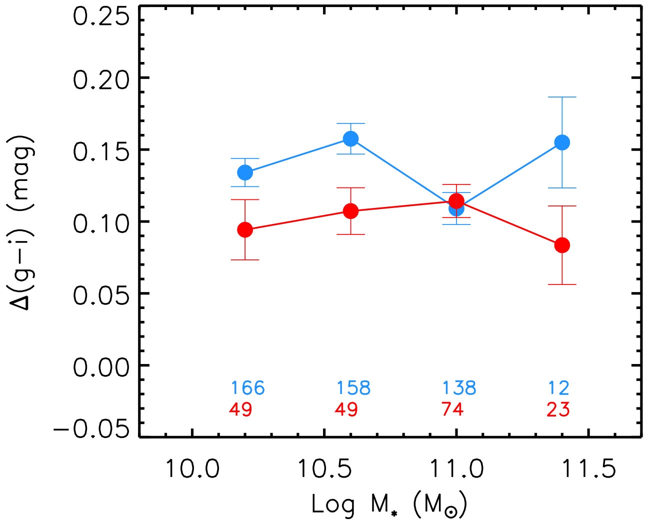

Figure 13. Average $g - i$ colour gradients, defined as the difference between inner and outer $g - i$ colours, versus stellar mass for two bins of halo mass (symbols and colours as in Figs 11 and 12).

of massive galaxies extracted from the GASS parent sample, Wang et al. (2011) showed that more H I-rich systems are bluer on the outside relative to the inside compared to control samples matched in stellar mass and redshift. We use the same quantity adopted by Wang et al. (2011), but with opposite sign, and define $\Delta(g - i)$ as the difference between inner and outer $g - i$ colours (inner and outer regions are enclosed by R_{50} and 2.5 times the Kron radius, both determined from r-band photometry, respectively). Therefore, $\Delta(g - i)$ is typically positive for disc galaxies (especially the bulge-dominated ones), because their outer regions are bluer than their inner regions. We plot the average $g - i$ colour gradients versus stellar mass in our two usual halo bins in Fig. 13. There is tentative evidence that galaxies in the stellar mass interval of interest ($\lesssim 10^{11}$ $M_{\odot}$) have smaller values of $\Delta(g - i)$ when they are located in more massive haloes – in other words their colour gradients are *flatter*. Because their specific star formation rates are smaller (i.e. their global $g - i$ colours are redder), this implies that their outer regions have become redder (as opposed to their central parts bluer), compared to those of galaxies with the same stellar mass but found in smaller haloes. This is expected from the fact that most of the H I gas in a galaxy is typically found beyond R_{50}, and supports an outside-in suppression (without any strong enhancement in the centre) of both gas and star formation in groups.

From the evidence presented by our data, we conclude that H I gas is removed from massive galaxies in the group environment, and that the process responsible for this quenches their star formation as well, most likely in the outer regions of the galaxy. Although we clearly observe the H I suppression only in galaxies with stellar masses less than $\sim 10^{11}$ $M_{\odot}$, we cannot exclude that environmental effects are at work also in more massive systems, which are already gas poor. This is because at high stellar mass the average GASS galaxy is a non-detection; hence, we are not able to detect a possible H I decrease with respect to similar objects in smaller dark matter haloes.

As discussed in the previous section, the difference of detection fractions at fixed NUV$-r$ colour between high- and low-mass haloes might indicate that the suppression of the gas takes place on time-scales of $\sim$1 Gyr or shorter. This would be in qualitative agreement with the cosmological hydrodynamical simulations of Davé et al. (2013), which suggest that the process that removes H I from satellite galaxies acts quickly compared to the infall time-scale into the halo (several Gyr). All this points to a pre-processing of the gas (and star formation) in the group environment. Both ram pressure stripping and tidal interactions might be responsible for this quenching, but the fact that the mechanism seems to truncate the star formation outside-in might favour ram pressure. It is currently unclear if ram pressure stripping can significantly affect the interstellar medium of galaxies outside the rich cluster environment, where hot X-ray-emitting gas is not present, but there is some evidence that this might be the case (e.g. Freeland & Wilcots 2011; Scott et al. 2012).

Very interestingly, Fabello et al. (2012) came to a similar conclusion with a completely different approach. These authors determined the average gas content of massive galaxies by

Downloaded from http://mnras.oxfordjournals.org/ at Swinburne University of Technology on August 11, 2014

cross-correlating the GASS parent sample with ALFALFA, and stacking the H I spectra (mostly non-detections). They binned the galaxies by stellar mass and local density, estimated from the number of neighbours with $M_* \geq 10^{9.5}\,M_\odot$ within 1 Mpc and $\pm$ 500 km s^{-1}, and compared their results with predictions of semi-analytic models (Guo et al. 2011). For galaxies with $M_* \leq 10^{10.5}\,M_\odot$ (where they are not limited by small number statistics), the decline in average gas fraction with local density is stronger than the decline in mean global and central specific star formation rates. This ordering is not reproduced by the semi-analytic models, which do not include stripping of the cold interstellar medium, and suggests that ram pressure is able to remove atomic gas from the outer discs of galaxies *in the group environment* probed by GASS. Furthermore, Fabello et al. (2012) used mock catalogues generated from the semi-analytic models to show that galaxies with $10 < \log M_*/M_\odot < 10.5$ and local density parameter $N > 7$, for which the strong decline in H I content is seen, are found in dark matter haloes with masses in the range of 10^{13}–$10^{14}\,M_\odot$, in agreement with what we determined more directly in this work.

Although it is well known that the star formation of galaxies is affected by the environment well before reaching the highest densities typical of clusters, to our knowledge this is the first time that environmental effects have been proved to remove H I gas in groups in a statistical sense and from an observational point of view. Our data indicate that, at fixed stellar mass, the gas fraction of galaxies with stellar mass between 10^{10} and $10^{11}\,M_\odot$ drops by at least 50 per cent in dark matter haloes with $M_h \sim 10^{13}$–$10^{14}\,M_\odot$. The removal of gas in groups most likely drives the observed quenching of the star formation in these systems, and although not conclusive, we offered some evidence in support of a hydrodynamical process like ram pressure stripping behind this effect. This is extremely important for our understanding of the physical processes that transform galaxies from blue, star forming to red and passively evolving, and suggests a key role for the pre-processing in groups. Indeed, hydrodynamical processes are usually considered not to be important in groups, and simulations do not include them (for instance, in the Guo et al. 2011 models, tidal and ram pressure forces only remove hot gas from the haloes of infalling satellites, and do not act on the cold gas).

Progress in this field requires not only better statistics and spatial resolution, but also sensitivity to low levels of gas content, which can be achieved only with large apertures and/or long integrations. GASS has the unique advantage of combining a stellar mass selection over a large volume (100–200 Mpc) with a low gas fraction limit, which allowed us to detect galaxies with $M_{\rm HI}/M_*$ down to a few per cent. In order to reach these gas fractions, we observed our targets up to 90 min on-source with the largest collecting area currently available. Restricting the survey to lower redshifts would decrease the telescope time, but at the price of increasing cosmic variance. All-sky H I-blind surveys planned with the Australian Square Kilometre Array (SKA) Pathfinder (ASKAP; Johnston et al. 2007) and the upgraded Westerbork Synthesis Radio Telescope (APERTIF; Verheijen et al. 2008), will provide larger samples and much better spatial resolution. The large volumes surveyed will compensate for the modest sensitivity, which will be comparable to that of ALFALFA, definitely allowing a step further in this field. Furthermore, stacking is a promising, complementary technique to extend the results presented in this work. However, a sensitive H I survey able to detect galaxies with small gas fractions over a comparable volume to GASS and across a wide range of environments might have to wait for the full SKA.

ACKNOWLEDGEMENTS

We thank the anonymous referee for useful suggestions.

BC is the recipient of an Australian Research Council Future Fellowship (FT120100660). APC acknowledges the National Natural Science Foundation of China International Cooperation and Exchange Grant, no. 11250110509. The research leading to these results has received funding from the European Community's Seventh Framework Programme (/FP7/2007-2013/) under grant agreement no. 229517.

This research has made use of the NASA/IPAC Extragalactic Database (NED) which is operated by the Jet Propulsion Laboratory, California Institute of Technology, under contract with the National Aeronautics and Space Administration.

The Arecibo Observatory is operated by SRI International under a cooperative agreement with the National Science Foundation (AST-1100968), and in alliance with Ana G. Méndez-Universidad Metropolitana and the Universities Space Research Association.

GALEX (Galaxy Evolution Explorer) is a NASA Small Explorer, launched in April 2003. We gratefully acknowledge NASA's support for construction, operation and science analysis for the *GALEX* mission, developed in cooperation with the Centre National d'Etudes Spatiales (CNES) of France and the Korean Ministry of Science and Technology.

Funding for the SDSS and SDSS-II has been provided by the Alfred P. Sloan Foundation, the Participating Institutions, the National Science Foundation, the US Department of Energy, the National Aeronautics and Space Administration, the Japanese Monbukagakusho, the Max Planck Society and the Higher Education Funding Council for England. The SDSS website is http://www.sdss.org/.

The SDSS is managed by the Astrophysical Research Consortium for the Participating Institutions. The Participating Institutions are the American Museum of Natural History, Astrophysical Institute Potsdam, University of Basel, University of Cambridge, Case Western Reserve University, University of Chicago, Drexel University, Fermilab, the Institute for Advanced Study, the Japan Participation Group, Johns Hopkins University, the Joint Institute for Nuclear Astrophysics, the Kavli Institute for Particle Astrophysics and Cosmology, the Korean Scientist Group, the Chinese Academy of Sciences (LAMOST), Los Alamos National Laboratory, the Max-Planck-Institute for Astronomy (MPIA), the Max-Planck-Institute for Astrophysics (MPA), New Mexico State University, Ohio State University, University of Pittsburgh, University of Portsmouth, Princeton University, the United States Naval Observatory and the University of Washington.

REFERENCES

Adelman-McCarthy J. K. et al., 2008, ApJS, 175, 297
Baldry I. K., Glazebrook K., Brinkmann J., Ivezić Ž., Lupton R. H., Nichol R. C., Szalay A. S., 2004, ApJ, 600, 681
Balogh M. et al., 2004, MNRAS, 348, 1355
Binggeli B., Sandage A., Tammann G. A., 1985, AJ, 90, 1681
Blanton M. R., Moustakas J., 2009, ARA&A, 47, 159
Boselli A., Gavazzi G., 2006, PASP, 118, 517
Boselli A., Boissier S., Cortese L., Gil de Paz A., Seibert M., Madore B. F., Buat V., Martin D. C., 2006, ApJ, 651, 811
Boselli A. et al., 2010, PASP, 122, 261
Bravo-Alfaro H., Cayatte V., van Gorkom J. H., Balkowski C., 2000, AJ, 119, 580
Catinella B. et al., 2010, MNRAS, 403, 683 (DR1)
Catinella B. et al., 2012a, MNRAS, 420, 1959

Downloaded from http://mnras.oxfordjournals.org/ at Swinburne University of Technology on August 11, 2014

Catinella B. et al., 2012b, A&A, 544, A65 (DR2)
Cayatte V., van Gorkom J. H., Balkowski C., Kotanyi C., 1990, AJ, 100, 604
Chabrier G., 2003, PASP, 115, 763
Chung A., van Gorkom J. H., Kenney J. D. P., Vollmer B., 2007, ApJ, 659, L115
Chung A., van Gorkom J. H., Kenney J. D. P., Crowl H., Vollmer B., 2009, AJ, 138, 1741
Colless M. et al., 2001, MNRAS, 328, 1039
Cooper M. C. et al., 2006, MNRAS, 370, 198
Cortese L., 2012, A&A, 543, A132
Cortese L., Catinella B., Boissier S., Boselli A., Heinis S., 2011, MNRAS, 415, 1797
Cortese L. et al., 2012, A&A, 544, A101
Davé R., Finlator K., Oppenheimer B. D., 2011, MNRAS, 416, 1354
Davé R., Katz N., Oppenheimer B. D., Kollmeier J. A., Weinberg D. H., 2013, MNRAS, 434, 2645
Dressler A., 1980, ApJ, 236, 351
Dreyer J. L. E., 1888, Mem. R. Astron. Soc., 49, 1
Dreyer J. L. E., 1895, Mem. R. Astron. Soc., 51, 185
Dreyer J. L. E., 1908, Mem. R. Astron. Soc., 59, 105
Fabello S., Catinella B., Giovanelli R., Kauffmann G., Haynes M. P., Heckman T. M., Schiminovich D., 2011a, MNRAS, 411, 993
Fabello S., Kauffmann G., Catinella B., Giovanelli R., Haynes M. P., Heckman T. M., Schiminovich D., 2011b, MNRAS, 416, 1739
Fabello S., Kauffmann G., Catinella B., Li C., Giovanelli R., Haynes M. P., 2012, MNRAS, 427, 2841
Freeland E., Wilcots E., 2011, ApJ, 738, 145
Fu J., Guo Q., Kauffmann G., Krumholz M. R., 2010, MNRAS, 409, 515
Gavazzi G., 1989, ApJ, 346, 59
Gavazzi G. et al., 2013, A&A, 553, A90
Giovanelli R., Haynes M. P., 1985, ApJ, 292, 404
Giovanelli R. et al., 2005, AJ, 130, 2598
Gómez P. L. et al., 2003, ApJ, 584, 210
Gunn J. E., Gott J. R., III, 1972, ApJ, 176, 1
Guo Q. et al., 2011, MNRAS, 413, 101
Haynes M. P., Giovanelli R., 1984, AJ, 89, 758
Haynes M. P. et al., 2011, AJ, 142, 170
Huang S., Haynes M. P., Giovanelli R., Brinchmann J., 2012, ApJ, 756, 113
Huchtmeier W. K., 1997, A&A, 325, 473
Iono D., Yun M. S., Mihos J. C., 2004, ApJ, 616, 199
Johnston S. et al., 2007, PASA, 24, 174
Kauffmann G. et al., 2003, MNRAS, 341, 54
Kauffmann G., White S. D. M., Heckman T. M., Ménard B., Brinchmann J., Charlot S., Tremonti C., Brinkmann J., 2004, MNRAS, 353, 713
Kauffmann G. et al., 2012, MNRAS, 422, 997
Kenney J. D. P., van Gorkom J. H., Vollmer B., 2004, AJ, 127, 3361
Kewley L. J., Geller M. J., Barton E. J., 2006, AJ, 131, 2004
Kilborn V. A., Forbes D. A., Barnes D. G., Koribalski B. S., Brough S., Kern K., 2009, MNRAS, 400, 1962
Lagos C. D. P., Baugh C. M., Lacey C. G., Benson A. J., Kim H.-S., Power C., 2011, MNRAS, 418, 1649
Larson R. B., Tinsley B. M., Caldwell C. N., 1980, ApJ, 237, 692
Lewis I. et al., 2002, MNRAS, 334, 673
Martin D. C. et al., 2005, ApJ, 619, L1
Moran S. M. et al., 2012, ApJ, 745, 66
Nilson P., 1973, Uppsala General Catalogue of Galaxies, Almqvist & Wiksell (distr.)
Saintonge A., 2007, AJ, 133, 2087
Saintonge A. et al., 2011, MNRAS, 415, 32
Salim S. et al., 2007, ApJS, 173, 267
Schiminovich D. et al., 2010, MNRAS, 408, 919
Scott T. C., Cortese L., Brinks E., Bravo-Alfaro H., Auld R., Minchin R., 2012, MNRAS, 419, L19
Shen S., Mo H. J., White S. D. M., Blanton M. R., Kauffmann G., Voges W., Brinkmann J., Csabai I., 2003, MNRAS, 343, 978
Solanes J. M., Manrique A., García-Gómez C., González-Casado G., Giovanelli R., Haynes M. P., 2001, ApJ, 548, 97
Springob C. M., Haynes M. P., Giovanelli R., Kent B. R., 2005, ApJS, 160, 149 (S05)
Verdes-Montenegro L., Yun M. S., Williams B. A., Huchtmeier W. K., Del Olmo A., Perea J., 2001, A&A, 377, 812
Verheijen M. A. W., Oosterloo T. A., van Cappellen W. A., Bakker L., Ivashina M. V., van der Hulst J. M., 2008, in Minchin R., Momjian E., eds, AIP Conf. Ser. Vol. 1035, The Evolution of Galaxies Through the Neutral Hydrogen Window. Am. Inst. Phys., New York, p. 265
Vollmer B., 2009, A&A, 502, 427
Wang J., Overzier R., Kauffmann G., von der Linden A., Kong X., 2010, MNRAS, 401, 433
Wang J. et al., 2011, MNRAS, 412, 1081
Warren M. S., Abazajian K., Holz D. E., Teodoro L., 2006, ApJ, 646, 881
Weinmann S. M., van den Bosch F. C., Yang X., Mo H. J., 2006, MNRAS, 366, 2
Woo J. et al., 2013, MNRAS, 428, 3306
Wyder T. K. et al., 2007, ApJS, 173, 293
Yang X., Mo H. J., van den Bosch F. C., Pasquali A., Li C., Barden M., 2007, ApJ, 671, 153
Yang X., Mo H. J., van den Bosch F. C., Zhang Y., Han J., 2012, ApJ, 752, 41
York D. G. et al., 2000, AJ, 120, 1579
Yun M. S., Ho P. T. P., Lo K. Y., 1994, Nat, 372, 530
Zwicky F., Herzog E., Wild P., Karpowicz M., Kowal C. T., 1961, Catalogue of Galaxies and of Clusters of Galaxies, Vol. I. California Institute of Technology

APPENDIX A: DATA RELEASE

We present here SDSS postage stamp images, Arecibo H I-line spectra and catalogues of optical, UV and H I parameters for the 250 galaxies included in this third and final data release. The content and format of the tables are identical to the DR2 ones, and we refer the reader to that paper for details. We only briefly summarize their content below. Notes on individual objects (marked with an asterisk in the last column of Tables A2 and A3) are reported in Appendix B.

SDSS and *GALEX* data

Table A1 lists optical and UV quantities for the 250 GASS galaxies, ordered by increasing right ascension:

Columns 1 and 2: GASS and SDSS identifiers.

Column 3: UGC (Nilson 1973), NGC (Dreyer 1888) or IC (Dreyer 1895, 1908) designation, or other name, typically from the Catalog of Galaxies and Clusters of Galaxies (CGCG; Zwicky et al. 1961), or the Virgo Cluster Catalog (Binggeli, Sandage & Tammann 1985).

Column 4: SDSS redshift, $z_{\rm SDSS}$. The typical uncertainty of SDSS redshifts for this sample is 0.0002.

Column 5: base-10 logarithm of the stellar mass, M_*, in solar units. Stellar masses are derived from SDSS photometry using the methodology described in Salim et al. (2007) (a Chabrier 2003 initial mass function is assumed). Over our required stellar mass range, these values are believed to be accurate to better than 30 per cent.

Column 6: radius containing 50 per cent of the Petrosian flux in z band, $R_{50,\,z}$, in arcsec.

Columns 7 and 8: radii containing 50 and 90 per cent of the Petrosian flux in r band, R_{50} and R_{90}, respectively, in arcsec.

Downloaded from http://mnras.oxfordjournals.org/ at Swinburne University of Technology on August 11, 2014

Table A1. SDSS and UV parameters.

GASS (1)	SDSS ID (2)	Other name (3)	z_{SDSS} (4)	$\log M_*$ ($M_\odot$) (5)	$R_{50,z}$ (arcsec) (6)	R_{50} (arcsec) (7)	R_{90} (arcsec) (8)	$\log \mu_*$ ($M_\odot$ kpc^{-2}) (9)	ext$_r$ (mag) (10)	r (mag) (11)	$(b/a)_r$ (12)	incl (deg) (13)	NUV$-r$ (mag) (14)	T_{NUV} (s) (15)	T_{max} (min) (16)
11892	J000200.82+150132.1	–	0.0357	10.54	3.12	3.37	9.96	8.99	0.13	15.03	0.820	36	5.60	1705	49
11903	J000458.72+154018.2	–	0.0373	10.17	2.16	2.11	5.99	8.90	0.19	15.93	0.411	69	5.49	260	71
11910	J000632.57+154004.7	–	0.0370	10.28	2.97	3.10	8.53	8.74	0.18	15.67	0.555	58	3.69	260	68
12030	J001842.68+151142.6	–	0.0372	10.65	2.41	2.44	7.63	9.29	0.13	14.85	0.724	45	5.68	1588	34
12062	J002556.06+153815.0	–	0.0365	10.09	2.63	2.83	6.16	8.67	0.15	15.41	0.708	46	2.36	222	65
3157	J003032.94+145635.4	–	0.0381	10.57	2.73	2.87	8.41	9.08	0.17	15.33	0.744	43	5.09	3133	56
3258	J005316.95+160556.1	–	0.0393	10.27	2.82	3.11	7.98	8.72	0.21	16.23	0.363	72	6.23	1918	88
3305	J005709.66+143906.6	–	0.0494	10.71	3.22	3.83	11.49	8.84	0.14	15.39	0.360	72	3.02	1996	85
3321	J010228.41+154457.0	–	0.0403	10.85	5.22	5.52	13.71	8.75	0.31	15.42	0.218	85	5.76	110	19
3284	J010253.84+141140.3	–	0.0397	10.60	4.16	4.82	12.14	8.71	0.14	15.57	0.335	74	5.05	110	57
3634	J011347.63+153029.8	–	0.0453	10.89	3.58	3.72	10.82	9.01	0.18	14.87	0.908	25	6.15	1440	26
3666	J011803.07+153224.4	–	0.0382	10.25	3.30	3.49	9.00	8.59	0.16	15.47	0.614	54	2.96	1647	78
3773	J012153.31+145344.6	–	0.0362	10.56	2.68	2.79	8.81	9.13	0.13	14.82	0.887	28	5.31	1658	47
3792	J012842.03+143633.2	–	0.0364	10.81	4.44	5.34	15.14	8.93	0.10	14.62	0.805	37	4.79	112	15
27250	J013006.16+131702.1	–	0.0380	10.24	4.22	4.67	10.19	8.37	0.15	15.25	0.928	22	2.59	198	76
27284	J013204.58+153001.2	–	0.0440	10.95	4.31	4.89	13.12	8.93	0.15	14.47	0.772	40	3.61	107	18
3851	J013851.94+150258.8	CGCG 437−007	0.0278	10.59	4.14	4.49	13.67	9.02	0.16	14.45	1.000	2	5.88	2954	14
4111	J014601.79+141421.0	–	0.0441	10.89	6.64	8.49	16.61	8.49	0.14	14.63	0.733	44	3.39	1625	24
4165	J015046.48+134127.5	–	0.0441	10.83	2.42	2.65	8.85	9.31	0.21	15.10	0.708	46	5.83	1661	30
4163	J015244.40+131133.3	–	0.0262	10.22	3.89	4.47	10.87	8.75	0.19	14.85	0.699	47	2.94	1661	17
4134	J015606.45+123403.2	–	0.0445	10.64	3.23	3.60	10.14	8.86	0.19	15.77	0.335	74	5.16	1659	76
4136	J015703.78+131001.4	–	0.0323	10.85	4.42	4.85	14.49	9.09	0.15	14.43	0.558	58	5.70	1651	8
4130	J015720.03+131013.4	–	0.0448	10.81	3.37	3.54	11.49	8.99	0.15	15.03	0.621	53	5.09	1651	36
4132	J015742.52+132318.8	–	0.0443	10.82	4.15	4.52	10.15	8.83	0.16	15.25	0.330	74	3.79	1651	32
3917	J015755.84+132129.3	–	0.0444	10.95	3.95	4.07	10.82	9.00	0.15	14.61	0.664	50	4.48	1651	18
3936	J015945.90+134652.6	–	0.0441	10.12	3.82	3.83	7.14	8.20	0.17	15.94	0.426	67	2.72	1663	141
3957	J020325.71+133910.7	–	0.0325	10.14	2.70	3.01	9.15	8.80	0.24	15.75	0.683	48	5.57	1664	40
3960	J020351.38+144534.3	–	0.0321	10.03	2.21	2.68	6.87	8.87	0.17	15.68	0.449	66	3.30	1664	38
3956	J020353.23+134011.9	–	0.0327	10.59	3.29	3.63	11.75	9.07	0.26	14.92	0.778	40	5.64	1662	27
3966	J020455.76+140055.4	–	0.0310	10.53	4.07	4.50	14.63	8.87	0.21	14.85	0.779	40	5.69	1664	29
3972	J020539.16+143907.7	–	0.0429	11.15	4.49	4.67	14.67	9.12	0.13	14.19	0.709	46	5.83	564	6
4014	J020720.31+130154.4	–	0.0482	10.98	3.54	3.60	11.85	9.05	0.26	14.67	0.509	61	5.57	1661	22
4008	J020829.86+124359.9	–	0.0347	10.49	3.70	4.28	10.55	8.81	0.31	14.96	0.783	39	3.28	1661	53
3987	J021337.66+132741.5	–	0.0420	10.80	2.47	2.62	8.43	9.31	0.28	14.78	0.718	45	5.93	1692	28
4056	J021349.29+135035.7	–	0.0375	10.42	1.75	1.81	5.29	9.33	0.35	15.41	0.434	67	4.17	1692	72
3980	J021423.65+122015.6	–	0.0408	10.95	2.82	2.97	8.91	9.37	0.42	14.44	0.463	65	–	201	13
12069	J073906.01+290936.2	CGCG 147−050	0.0388	11.13	6.76	7.73	17.60	8.83	0.13	13.70	0.924	23	2.93	1531	5
14260	J074158.62+231035.0	CGCG 117−066	0.0431	11.06	2.47	2.56	8.67	9.54	0.14	14.17	0.733	44	5.71	194	10
14017	J074426.50+291609.7	CGCG 147−063	0.0396	10.92	2.97	3.09	10.11	9.32	0.09	14.47	0.568	57	5.41	1535	13
21842	J074533.96+184812.0	–	0.0450	11.06	4.36	5.72	17.49	9.01	0.10	14.57	0.729	44	5.41	156	12
51334	J075329.53+140122.8	–	0.0294	10.10	3.59	4.28	9.68	8.61	0.10	16.04	0.202	88	3.57	1656	27
51351	J075457.85+142718.8	CGCG 058−069	0.0293	11.01	5.21	6.28	18.89	9.19	0.09	13.60	0.615	54	3.95	209	3

Downloaded from http://mnras.oxfordjournals.org/ at Swinburne University of Technology on August 11, 2014

Table A1 – *continued*

GASS (1)	SDSS ID (2)	Other name (3)	z_{SDSS} (4)	$\log M_*$ ($M_\odot$) (5)	$R_{50,z}$ (arcsec) (6)	R_{50} (arcsec) (7)	R_{90} (arcsec) (8)	$\log \mu_*$ ($M_\odot$ kpc^{-2}) (9)	ext$_r$ (mag) (10)	r (mag) (11)	$(b/a)_r$ (12)	incl (deg) (13)	NUV$-r$ (mag) (14)	T_{NUV} (s) (15)	T_{max} (min) (16)
51462	J075600.62+141144.6	CGCG 058−072	0.0357	11.10	2.97	3.04	9.69	9.59	0.09	13.63	0.483	63	6.11	196	4
51336	J075617.10+143609.6	–	0.0474	11.00	5.38	6.18	13.64	8.72	0.09	14.66	0.732	44	4.20	209	19
19132	J080020.05+222634.8	–	0.0350	10.35	2.04	2.10	6.46	9.18	0.18	15.50	0.832	35	5.74	1696	54
56320	J080342.27+100159.7	–	0.0337	10.22	2.69	2.87	8.25	8.85	0.07	15.64	0.776	40	6.37	218	47
51580	J080403.84+150518.4	–	0.0390	10.24	2.24	2.49	7.46	8.90	0.10	16.52	0.264	80	4.27	2650	85
14247	J080528.11+355648.1	IC 2225	0.0330	11.14	6.73	7.72	22.90	8.99	0.13	13.53	0.567	57	4.90	218	2
19274	J081625.36+255928.8	UGC 4303	0.0453	11.32	6.38	8.06	20.00	8.94	0.10	14.01	0.753	42	4.54	78	4
51899	J083131.52+192228.3	–	0.0387	10.01	2.72	3.01	6.85	8.51	0.09	16.26	0.510	61	3.27	3072	82
52045	J083836.42+173809.2	CGCG 089−060	0.0415	10.17	3.45	3.97	9.44	8.40	0.08	15.47	0.962	16	2.25	1830	109
32308	J083934.43+252837.6	–	0.0292	10.02	7.09	8.07	14.75	7.93	0.10	15.33	0.943	20	3.52	4026	26
56486	J084528.61+143425.6	–	0.0360	10.26	2.79	2.82	7.35	8.79	0.05	15.46	0.787	39	4.98	1685	61
56509	J085045.27+114839.0	–	0.0297	10.48	2.10	2.18	6.52	9.44	0.09	14.79	0.491	63	5.60	5569	28
8096	J085254.99+030908.4	–	0.0345	10.28	3.64	3.89	9.42	8.62	0.14	15.33	0.614	54	2.81	112	51
19989	J085425.62+081241.0	–	0.0294	10.46	2.97	3.14	10.01	9.13	0.14	14.78	0.658	50	5.73	1545	27
52297	J085724.03+204237.9	–	0.0328	10.49	3.18	3.44	10.42	9.00	0.07	15.03	0.572	57	4.19	1637	42
56662	J090254.93+133938.5	–	0.0299	10.24	5.22	6.66	15.78	8.41	0.09	15.90	0.227	84	4.71	1612	29
56612	J090307.74+134149.4	–	0.0290	10.27	2.15	2.36	6.97	9.23	0.08	15.29	0.477	64	5.07	1612	25
56650	J090308.20+133103.9	–	0.0289	10.24	1.78	1.85	5.43	9.37	0.09	15.50	0.463	65	5.81	1612	25
20026	J090610.15+082343.3	–	0.0457	10.46	2.10	2.22	7.41	9.04	0.14	15.66	0.912	25	5.40	1696	163
20041	J091427.70+080445.9	–	0.0309	10.03	2.97	3.19	9.10	8.65	0.13	15.78	0.350	73	4.77	2441	32
20042	J091444.06+083605.3	–	0.0468	10.01	2.69	2.61	6.02	8.35	0.14	16.30	0.617	53	2.64	2187	180
16756	J091717.67+064151.5	–	0.0333	10.43	2.79	3.07	9.89	9.04	0.10	15.22	0.654	51	5.85	1693	44
16815	J091831.34+065223.3	–	0.0393	10.63	1.62	1.82	6.02	9.56	0.11	15.60	0.605	54	5.96	1693	49
19672	J091929.51+341810.2	–	0.0458	10.73	3.11	3.33	7.19	8.96	0.05	15.00	0.690	48	2.55	168	58
33019	J092533.76+272050.9	CGCG 151−078	0.0484	11.15	4.73	4.92	13.76	8.97	0.06	14.34	0.298	77	5.72	345	10
32937	J092708.07+292408.2	CGCG 151−081	0.0258	10.45	5.57	6.63	18.38	8.68	0.06	14.60	0.441	66	4.02	8435	16
32907	J093009.18+285351.3	–	0.0349	10.47	4.36	4.64	10.94	8.65	0.06	15.79	0.261	80	4.58	112	54
53269	J093116.00+263259.6	–	0.0458	10.98	2.52	2.64	7.93	9.39	0.06	15.10	0.375	71	6.98	202	18
20165	J093231.96+094957.3	–	0.0498	10.82	2.23	2.25	6.96	9.26	0.11	15.34	0.823	35	–	–	53
33214	J093624.28+320445.5	–	0.0269	10.34	5.02	5.45	16.21	8.63	0.05	14.78	0.842	33	5.23	213	19
20149	J093647.77+100551.1	–	0.0494	10.91	4.15	4.51	10.97	8.82	0.08	15.03	0.351	73	4.20	106	35
55745	J093710.07+165837.9	NGC 2928	0.0278	10.92	10.04	12.44	28.70	8.57	0.10	13.71	0.432	67	4.28	106	3
8349	J093953.62+034850.2	–	0.0285	10.36	3.46	4.18	12.26	8.92	0.14	15.61	0.328	75	4.73	1735	24
33469	J095009.35+333409.5	NGC 3013	0.0270	10.61	4.82	5.56	15.62	8.93	0.04	14.24	0.718	45	–	–	11
22822	J095144.91+353719.6	–	0.0270	10.56	3.73	4.22	10.92	9.10	0.03	14.81	0.393	70	3.79	208	14
20376	J095416.82+103457.5	–	0.0399	10.54	2.83	3.11	8.57	8.97	0.08	15.44	0.776	40	5.40	208	78
20445	J095429.64+103530.1	–	0.0397	10.71	2.13	2.19	6.67	9.40	0.08	14.84	0.434	67	5.93	208	34
26017	J095641.82+111144.6	–	0.0416	10.71	5.24	5.46	11.51	8.57	0.09	14.97	0.562	58	4.46	109	42
33737	J095851.33+320423.0	CGCG 153−007	0.0270	10.69	5.85	7.27	17.66	8.84	0.04	14.28	0.661	50	–	–	8
33777	J100250.75+323840.2	–	0.0477	10.10	1.70	1.77	4.49	8.82	0.04	16.86	0.718	45	5.47	109	195
8634	J101324.41+050131.7	–	0.0464	10.13	1.32	1.37	3.54	9.09	0.08	16.74	0.862	31	5.59	320	174
26407	J102138.86+131845.6	–	0.0461	11.03	5.41	5.96	12.97	8.77	0.13	14.34	0.576	57	3.71	111	15

Downloaded from http://mnras.oxfordjournals.org/ at Swinburne University of Technology on August 11, 2014

Table A1 – *continued*

GASS (1)	SDSS ID (2)	Other name (3)	z_{SDSS} (4)	log M_* ($M_\odot$) (5)	$R_{50,z}$ (arcsec) (6)	R_{50} (arcsec) (7)	R_{90} (arcsec) (8)	log μ_* ($M_\odot$ kpc^{-2}) (9)	ext$_r$ (mag) (10)	r (mag) (11)	$(b/a)_r$ (12)	incl (deg) (13)	NUV$-r$ (mag) (14)	T_{NUV} (s) (15)	T_{max} (min) (16)
26406	J102149.72+132649.6	CGCG 065−008	0.0322	10.76	4.83	5.98	15.67	8.92	0.12	14.23	0.714	46	4.47	111	12
54240	J102253.59+243623.0	IC 2569	0.0463	11.13	4.61	4.98	15.67	9.01	0.06	14.32	0.867	31	5.97	199	9
26503	J102314.32+125224.0	–	0.0329	10.45	1.92	2.00	6.46	9.39	0.11	15.15	0.528	60	5.36	322	42
26436	J102413.51+131444.8	–	0.0326	10.01	2.36	2.36	6.00	8.78	0.11	16.09	0.883	29	5.57	322	41
23029	J102705.85+110317.5	IC 612	0.0323	10.90	3.65	3.76	11.45	9.30	0.08	14.12	0.524	60	5.72	335	6
26535	J102727.40+132526.2	–	0.0315	10.06	3.68	3.82	9.73	8.47	0.12	15.41	0.431	67	3.26	331	35
5204	J102750.83+023634.0	–	0.0285	10.40	3.00	3.14	7.85	9.09	0.10	14.82	0.785	39	4.70	3027	23
23070	J102802.88+104630.4	–	0.0448	11.02	4.77	5.25	13.43	8.89	0.09	15.37	0.200	90	4.33	335	14
23102	J102949.21+115144.4	–	0.0386	10.18	4.20	4.38	9.99	8.30	0.09	16.04	0.459	65	4.64	332	81
54577	J103018.65+273422.9	–	0.0480	11.00	2.83	2.95	9.83	9.27	0.07	14.73	0.675	49	5.71	1661	20
55541	J103246.99+211256.3	–	0.0429	10.62	4.41	5.04	12.50	8.61	0.07	15.31	0.233	83	3.08	190	72
23203	J103549.90+121212.7	CGCG 065−061	0.0371	10.92	4.34	4.55	13.98	9.05	0.08	14.26	0.732	44	6.03	211	10
26586	J103611.29+131025.3	–	0.0334	10.06	1.47	1.55	4.23	9.22	0.08	15.87	0.651	51	4.16	106	45
23213	J103621.90+115317.0	–	0.0293	10.14	3.49	3.74	9.00	8.67	0.07	15.53	0.331	74	3.67	206	26
26569	J103808.15+131737.0	–	0.0319	10.25	3.52	3.71	9.89	8.70	0.10	15.36	0.568	57	4.38	106	37
23302	J104248.63+110000.8	–	0.0295	10.43	3.56	3.83	11.02	8.94	0.08	14.79	0.708	46	4.51	439	27
15257	J104805.79+060114.4	–	0.0288	10.09	2.46	2.43	6.68	8.94	0.08	15.75	0.731	44	5.45	209	24
8971	J104837.87+044756.4	–	0.0333	10.15	4.44	4.60	9.93	8.35	0.08	15.75	0.600	55	4.42	42 538	45
34723	J105134.08+301221.8	–	0.0356	10.57	3.55	3.86	12.37	8.91	0.07	15.03	0.726	45	5.60	2610	43
8953	J105241.71+040913.9	–	0.0425	10.95	3.76	4.09	11.57	9.08	0.12	14.81	0.525	60	5.56	217	15
8945	J105315.29+042003.1	–	0.0417	10.82	2.39	2.69	7.90	9.37	0.11	15.27	0.461	65	4.60	1515	25
23496	J105721.59+120611.0	–	0.0477	10.16	4.62	4.99	9.72	8.01	0.05	15.55	0.564	57	2.08	203	196
17635	J105935.53+085536.5	CGCG 066−078	0.0309	10.48	4.75	5.08	11.56	8.69	0.08	14.72	0.442	66	3.61	106	33
17673	J105958.54+102312.4	–	0.0363	10.32	3.32	3.31	8.26	8.71	0.09	15.46	0.815	36	5.63	107	63
15485	J110004.55+080622.2	–	0.0349	10.13	2.08	2.07	4.81	8.95	0.10	15.82	0.790	39	5.48	442	54
23457	J110011.41+121015.1	–	0.0354	10.12	3.90	4.55	10.31	8.39	0.05	16.59	0.213	86	4.49	106	57
17622	J110043.97+090243.0	–	0.0354	10.05	3.50	4.04	11.28	8.41	0.07	16.58	0.260	80	4.49	106	57
34989	J110339.49+315129.4	UGC 6124	0.0466	11.04	3.51	4.03	13.19	9.15	0.08	14.87	0.361	72	4.35	6247	15
48356	J111113.19+284147.0	NGC 3561	0.0287	11.25	6.43	8.53	24.67	9.26	0.08	13.40	0.819	36	4.33	959	1
47825	J111147.22+281602.2	CGCG 156−017	0.0359	11.05	3.54	3.74	12.53	9.39	0.06	14.04	0.823	35	5.66	959	5
48205	J111151.56+271156.0	–	0.0471	11.12	3.56	4.14	14.72	9.21	0.06	14.31	0.775	40	3.44	184	10
48160	J111201.78+275053.8	–	0.0474	11.03	3.40	3.89	11.51	9.15	0.06	14.94	0.665	50	5.46	199	16
17824	J111404.85+090924.0	–	0.0342	10.11	3.05	3.37	7.82	8.62	0.09	16.02	0.302	77	3.77	1605	49
23531	J111429.02+110847.8	–	0.0406	10.74	2.20	2.30	7.02	9.38	0.04	14.88	0.212	86	5.78	1612	34
5701	J111509.40+024156.4	–	0.0442	10.72	4.23	5.43	13.81	8.72	0.19	15.75	0.111	90	4.03	220	51
48521	J111738.91+263506.0	–	0.0475	10.29	1.22	1.25	3.99	9.30	0.05	15.90	0.836	34	3.06	183	192
48518	J111750.72+263927.0	–	0.0285	10.42	5.03	5.15	13.21	8.65	0.04	14.78	0.734	44	4.33	183	23
24496	J111809.91+074653.9	–	0.0421	10.60	3.13	3.61	9.04	8.90	0.11	15.45	0.437	67	3.41	1524	73
12452	J112006.21+041035.6	–	0.0492	10.82	3.28	3.54	10.16	8.94	0.12	15.42	0.407	69	5.53	1536	51
48544	J112039.09+271737.4	–	0.0486	11.05	4.05	4.59	14.73	9.00	0.06	14.49	0.665	50	5.11	186	17
5848	J112142.43+033424.5	CGCG 039−145	0.0391	10.44	4.83	5.58	13.83	8.43	0.13	15.30	0.313	76	2.96	2045	85
23703	J112731.58+120834.3	IC 2835	0.0459	10.74	2.88	3.21	8.98	9.04	0.10	15.25	0.572	57	5.48	127	55

Downloaded from http://mnras.oxfordjournals.org/ at Swinburne University of Technology on August 11, 2014

Table A1 – *continued*

GASS (1)	SDSS ID (2)	Other name (3)	z_{SDSS} (4)	$\log M_*$ ($M_\odot$) (5)	$R_{50,z}$ (arcsec) (6)	R_{50} (arcsec) (7)	R_{90} (arcsec) (8)	$\log \mu_*$ ($M_\odot$ kpc^{-2}) (9)	ext$_r$ (mag) (10)	r (mag) (11)	$(b/a)_r$ (12)	incl (deg) (13)	NUV$-r$ (mag) (14)	T_{NUV} (s) (15)	T_{max} (min) (16)
48604	J112746.27+265734.5	CGCG 156−077	0.0334	10.60	3.76	4.34	10.11	8.95	0.05	14.64	0.657	50	3.20	51	29
6015	J113524.48+021627.3	–	0.0289	10.23	2.33	2.92	7.75	9.13	0.08	16.40	0.371	71	4.46	1714	25
23761	J113704.29+125535.7	IC 2945	0.0345	11.07	5.96	6.71	21.97	8.99	0.08	13.80	0.727	44	5.06	341	4
23739	J113706.07+115237.7	–	0.0358	10.90	2.72	2.93	9.64	9.47	0.08	14.58	0.432	67	6.13	252	9
23789	J114144.66+122937.1	–	0.0342	10.41	3.23	3.37	9.03	8.87	0.11	15.11	0.913	25	5.69	112	50
23781	J114212.30+113041.1	–	0.0432	10.62	2.36	2.51	7.87	9.14	0.10	15.49	0.610	54	4.29	258	75
48994	J114218.00+301349.0	UGC 6664	0.0322	10.73	6.70	9.16	25.94	8.61	0.06	14.35	0.275	79	2.67	103	14
23815	J115036.65+112151.9	–	0.0306	10.23	2.66	3.03	9.31	8.95	0.11	15.47	0.613	54	3.24	107	32
18084	J115112.59+085311.6	–	0.0351	10.34	5.30	5.61	10.74	8.35	0.06	15.27	0.706	46	3.85	112	55
18004	J115135.06+084507.6	–	0.0352	11.12	5.39	5.42	17.74	9.11	0.07	13.89	0.809	37	5.75	112	3
49433	J115536.63+292104.4	–	0.0458	10.45	3.12	3.27	8.43	8.68	0.06	15.57	0.627	53	3.67	109	164
49386	J115913.81+305325.8	–	0.0294	10.53	3.13	3.81	12.26	9.15	0.04	15.19	0.416	68	5.30	1680	23
18138	J120239.51+085624.2	–	0.0347	10.64	4.46	4.98	14.66	8.81	0.06	15.40	0.247	81	5.13	86	27
18185	J120308.04+110920.4	–	0.0438	10.83	3.72	3.83	12.91	8.95	0.07	14.81	0.828	35	5.68	1201	30
49727	J120445.20+311132.9	CGCG 158−011	0.0250	10.27	2.31	2.40	7.85	9.30	0.05	15.11	0.455	65	4.76	1695	14
18131	J120445.85+092521.1	–	0.0353	10.34	2.29	2.61	7.65	9.07	0.07	15.49	0.568	57	7.05	86	57
18225	J120511.42+103341.0	–	0.0334	10.14	2.49	2.55	7.06	8.84	0.06	15.94	0.745	43	4.68	1201	45
18220	J120536.25+104113.3	–	0.0344	10.50	3.72	3.70	10.17	8.83	0.07	15.17	0.320	75	4.71	1201	50
28062	J122800.84+081108.1	–	0.0377	10.70	4.06	4.52	12.83	8.87	0.06	14.91	0.514	61	4.43	3272	30
28030	J122902.67+083133.3	–	0.0385	10.02	4.16	4.43	8.60	8.15	0.06	16.27	0.522	60	3.75	1597	81
50404	J123409.10+280750.5	–	0.0400	10.55	2.24	2.30	6.65	9.18	0.04	15.05	0.635	52	5.26	1626	76
12967	J123553.51+054723.4	–	0.0419	10.57	3.64	4.06	14.50	8.74	0.06	15.06	0.630	52	5.05	3047	82
50406	J123653.92+274456.8	NGC 4559B	0.0258	10.41	6.09	6.12	13.65	8.57	0.06	14.34	0.817	36	3.11	1626	16
50550	J124128.01+284728.3	–	0.0350	10.29	3.66	3.73	8.26	8.62	0.05	15.14	0.622	53	3.27	123	55
50856	J125547.82+281521.9	–	0.0270	10.40	4.23	5.16	14.97	8.83	0.03	15.40	0.241	82	5.13	2547	19
50866	J125609.90+275039.3	–	0.0253	10.49	4.93	5.39	15.59	8.85	0.03	14.51	0.527	60	5.69	2780	14
40495	J125626.93+093604.5	–	0.0459	10.92	3.09	3.20	9.48	9.15	0.06	14.71	0.645	51	5.08	247	24
35497	J125650.61+285547.4	–	0.0270	10.44	4.66	4.96	14.57	8.79	0.03	14.25	0.384	70	4.92	2593	19
40502	J125752.83+101754.6	–	0.0363	10.19	3.44	3.89	9.89	8.54	0.06	15.87	0.219	85	3.15	233	63
35475	J125935.67+283304.9	–	0.0253	10.29	2.59	2.71	9.10	9.21	0.03	14.94	0.576	57	5.79	3503	14
35437	J130125.07+284038.0	–	0.0291	10.23	7.60	7.89	15.76	8.09	0.04	14.45	0.923	23	2.70	3503	26
6679	J130210.77+030623.6	CGCG 043−105	0.0472	11.03	3.57	3.78	11.84	9.11	0.09	14.07	0.937	21	3.32	306	16
13159	J130525.44+035929.7	–	0.0437	10.37	2.40	2.66	6.96	8.86	0.07	16.62	0.290	78	5.27	3371	135
40647	J130624.82+095635.8	–	0.0487	10.73	4.16	4.32	9.22	8.65	0.07	14.88	0.653	51	3.09	354	74
25215	J131032.19+110121.0	CGCG 072−010	0.0427	10.59	4.29	4.54	10.41	8.60	0.08	14.84	0.635	52	2.98	293	81
25213	J131222.82+114339.5	–	0.0320	10.12	4.09	4.38	9.21	8.43	0.08	15.60	0.628	53	3.42	128	38
26936	J131525.21+152522.2	CGCG 101−014	0.0266	10.74	3.48	3.80	12.19	9.36	0.07	14.36	0.458	65	5.99	332	6
44354	J132050.70+313700.6	–	0.0448	10.68	4.17	6.36	15.28	8.67	0.03	15.33	0.660	50	3.06	3417	66
51150	J132259.87+270659.1	IC 4234	0.0345	10.80	6.54	6.91	16.82	8.64	0.06	13.74	0.815	36	3.60	161 224	13
51161	J132522.77+271456.7	–	0.0345	10.15	5.07	5.65	14.19	8.21	0.04	15.38	0.616	54	2.84	161 224	51
43963	J134142.40+300731.5	NGC 5271	0.0370	11.05	5.46	7.83	22.14	8.98	0.04	13.98	0.640	52	4.03	148	5
35659	J134159.72+294653.5	–	0.0449	11.14	4.73	5.35	16.17	9.02	0.05	14.41	0.515	61	4.83	148	8

Downloaded from http://mnras.oxfordjournals.org/ at Swinburne University of Technology on August 11, 2014

Table A1 – *continued*

GASS (1)	SDSS ID (2)	Other name (3)	z_{SDSS} (4)	log M_* ($M_\odot$) (5)	$R_{50,z}$ (arcsec) (6)	R_{50} (arcsec) (7)	R_{90} (arcsec) (8)	log μ_* ($M_\odot$ kpc^{-2}) (9)	ext$_r$ (mag) (10)	r (mag) (11)	$(b/a)_r$ (12)	incl (deg) (13)	NUV$-r$ (mag) (14)	T_{NUV} (s) (15)	T_{max} (min) (16)
44021	J134231.07+301500.1	CGCG 161−128	0.0363	11.06	4.03	4.23	14.07	9.27	0.04	14.18	0.460	65	5.23	148	5
38018	J134834.19+245329.2	–	0.0297	10.08	4.18	5.09	13.46	8.44	0.04	16.24	0.230	83	3.35	178	28
35981	J135308.35+354250.5	UGC 8802	0.0411	10.30	4.78	8.79	19.46	8.25	0.04	15.31	0.458	65	2.50	3864	106
44856	J135411.14+243322.5	–	0.0286	10.05	1.60	1.64	4.92	9.28	0.04	15.85	0.669	49	5.29	268	24
44892	J135609.30+251143.6	CGCG 132−055	0.0290	10.66	4.42	4.78	15.64	9.00	0.05	14.40	0.769	41	5.59	268	12
13618	J135622.01+043710.6	–	0.0339	10.20	2.96	3.22	8.06	8.74	0.08	16.01	0.339	74	4.62	18 451	47
13674	J135815.23+035953.8	CGCG 046−020	0.0300	10.10	5.25	5.64	11.64	8.25	0.10	15.00	0.522	61	2.58	18 849	29
9317	J140430.25+050629.4	–	0.0295	10.04	4.71	5.05	10.95	8.30	0.07	15.13	0.912	25	2.64	15 250	27
38458	J140603.77+123016.2	–	0.0387	10.41	2.82	3.17	10.94	8.88	0.08	15.50	0.887	28	5.51	220	82
7121	J140642.63+015452.2	–	0.0472	10.24	1.34	1.45	4.05	9.18	0.10	16.48	0.415	68	4.46	129	187
30746	J140908.49+061048.8	–	0.0363	10.32	1.92	2.00	5.84	9.18	0.06	15.55	0.508	62	5.91	1680	63
7310	J141657.47+021039.5	CGCG 018−102	0.0261	10.44	2.48	2.66	9.00	9.37	0.12	14.67	0.614	54	5.20	1636	16
45254	J141830.77+291012.3	CGCG 163−026	0.0349	11.03	3.46	3.88	12.27	9.41	0.05	14.02	0.677	49	4.98	161	5
7405	J141837.70+020245.4	–	0.0256	10.53	4.55	5.01	10.96	8.95	0.10	14.98	0.269	79	3.74	1636	13
45940	J142748.88+262900.7	–	0.0325	10.43	2.55	2.89	9.90	9.13	0.05	15.16	0.822	36	5.86	61	40
28703	J142802.34+120134.9	–	0.0267	10.16	5.84	5.87	14.22	8.32	0.07	15.41	0.250	81	3.77	108	18
9615	J143001.87+032352.1	–	0.0333	10.15	1.62	1.69	4.97	9.23	0.08	16.67	0.808	37	5.35	1691	44
9607	J143043.65+031149.3	–	0.0268	10.26	2.16	2.19	6.65	9.28	0.08	15.06	0.396	70	5.79	1691	18
38198	J143134.60+244053.6	–	0.0378	10.65	4.01	4.49	13.32	8.83	0.09	14.81	0.471	64	–	–	37
31095	J143749.60+064454.3	CGCG 047−122	0.0290	10.08	6.14	6.39	13.46	8.13	0.09	14.91	0.600	55	2.52	1995	25
41621	J144011.86+081512.2	–	0.0296	10.35	1.69	1.71	5.16	9.50	0.08	15.03	0.399	69	5.27	93	28
9702	J144043.35+032226.4	IC 1043	0.0319	10.79	2.25	2.32	7.37	9.63	0.09	14.41	0.510	61	5.50	2701	10
9938	J144140.50+040347.1	–	0.0275	10.08	5.75	6.31	12.53	8.24	0.09	15.16	0.936	21	3.12	1696	20
41699	J144213.77+084036.0	CGCG 075−117	0.0341	10.92	5.38	6.31	16.05	8.94	0.08	14.24	0.621	53	4.90	218	7
9695	J144216.88+034844.7	–	0.0257	10.13	3.19	3.42	10.96	8.85	0.09	15.18	0.387	70	5.26	1687	15
31131	J144248.49+063924.3	CGCG 048−003	0.0279	10.48	3.03	3.26	9.98	9.17	0.09	14.49	0.766	41	5.38	1743	21
9942	J144325.65+042244.6	CGCG 048−008	0.0264	10.82	4.34	4.51	15.20	9.25	0.09	13.74	0.787	39	5.22	1911	4
41718	J144338.96+083350.7	–	0.0346	10.46	2.62	2.74	8.77	9.09	0.08	15.20	0.822	36	5.73	218	52
31478	J144350.25+313128.7	–	0.0335	10.37	1.77	1.85	5.79	9.37	0.04	15.39	0.412	68	5.49	84	46
41723	J144605.27+085456.2	CGCG 076−020	0.0295	10.71	3.28	3.47	11.06	9.29	0.08	14.11	0.618	53	5.29	221	10
29371	J144907.58+105847.6	CGCG 076−065	0.0292	10.70	4.18	4.35	14.12	9.07	0.06	14.16	0.677	49	5.31	141	10
10032	J145024.11+043655.2	–	0.0468	10.82	1.66	1.80	5.21	9.57	0.14	15.35	0.407	69	5.43	1682	42
42233	J145304.36+310406.0	–	0.0323	10.49	2.50	3.04	7.68	9.22	0.05	15.48	0.424	68	3.73	317	39
10005	J145307.29+033217.4	–	0.0334	10.47	2.51	2.64	7.48	9.17	0.11	15.05	0.734	44	4.95	5768	45
42191	J145403.73+305046.4	–	0.0320	10.12	1.71	1.74	4.86	9.19	0.06	15.31	0.641	52	2.62	317	38
38935	J145458.46+114156.2	CGCG 076−094	0.0305	10.90	3.61	4.02	14.43	9.36	0.09	13.88	0.576	57	5.09	79	5
41743	J150204.10+064922.9	–	0.0462	10.45	3.39	3.57	8.99	8.60	0.09	15.79	0.415	68	3.59	1677	171
39014	J150513.62+084747.6	CGCG 076−145	0.0449	11.05	4.86	5.23	15.92	8.91	0.09	14.21	0.767	41	5.00	79	12
39082	J150721.51+095541.0	CGCG 077−013	0.0352	11.02	5.41	5.68	18.80	9.01	0.10	13.99	0.586	56	5.14	148	5
41869	J150921.50+070439.8	–	0.0414	10.15	3.22	3.16	6.85	8.44	0.11	16.05	0.366	72	3.40	1613	109
41863	J151028.90+072455.4	–	0.0322	10.11	4.20	3.43	8.99	8.40	0.10	16.46	0.356	72	1.76	1613	39
10211	J151219.92+031826.6	–	0.0469	10.97	5.70	5.81	13.20	8.65	0.12	14.88	0.386	70	4.01	1666	21

Downloaded from http://mnras.oxfordjournals.org/ at Swinburne University of Technology on August 11, 2014

Table A1 – *continued*

GASS (1)	SDSS ID (2)	Other name (3)	z_{SDSS} (4)	$\log M_*$ ($M_\odot$) (5)	$R_{50,z}$ (arcsec) (6)	R_{50} (arcsec) (7)	R_{90} (arcsec) (8)	$\log \mu_*$ ($M_\odot$ kpc^{-2}) (9)	ext$_r$ (mag) (10)	r (mag) (11)	$(b/a)_r$ (12)	incl (deg) (13)	NUV$-r$ (mag) (14)	T_{NUV} (s) (15)	T_{max} (min) (16)
7813	J151243.59+012752.2	CGCG 021−049	0.0293	10.79	4.15	4.74	15.08	9.17	0.13	14.04	0.581	56	5.60	1811	7
25057	J152106.26+304036.9	–	0.0308	10.01	3.12	2.90	8.04	8.59	0.06	15.81	0.719	45	5.35	2185	32
25115	J152112.78+303928.5	CGCG 165−039	0.0308	10.50	2.93	2.79	8.96	9.14	0.06	14.60	0.537	59	5.40	2185	32
39407	J152239.21+083226.7	–	0.0366	10.26	2.57	2.64	7.44	8.86	0.10	15.89	0.484	63	5.26	1513	65
39532	J152346.52+083853.1	–	0.0301	10.24	4.03	4.09	11.06	8.62	0.09	15.55	0.731	44	6.09	1513	29
28348	J154051.59+282027.7	–	0.0329	10.22	3.32	3.96	10.44	8.69	0.08	16.22	0.415	68	4.62	4531	42
28327	J154129.97+275911.4	–	0.0320	11.02	3.40	3.93	13.28	9.49	0.10	13.79	0.865	31	5.84	4531	3
28317	J154408.13+274024.3	–	0.0316	10.07	1.99	2.03	5.71	9.02	0.09	15.76	0.457	65	5.75	943	36
25682	J154811.74+090424.5	–	0.0393	10.59	2.55	2.75	8.97	9.13	0.11	15.11	0.639	52	5.85	1703	57
25721	J155506.74+093023.0	–	0.0341	10.09	2.62	2.99	8.40	8.73	0.11	16.38	0.346	73	4.16	1688	49
10918	J221421.77+135711.1	CGCG 428−054	0.0261	10.78	4.78	5.18	15.28	9.14	0.17	13.89	0.860	31	4.85	7104	4
11086	J225524.42+131453.8	NGC 7414	0.0329	10.43	2.68	2.77	7.96	9.08	0.14	15.21	0.390	70	4.26	1690	42
11080	J225608.33+130337.9	–	0.0290	10.10	2.26	2.47	6.76	9.01	0.12	15.91	0.366	72	4.74	2905	25
11249	J230757.92+152455.2	–	0.0362	10.11	2.93	2.78	6.69	8.60	0.64	15.96	0.791	39	7.87	298	63
11257	J230806.95+152520.1	–	0.0368	10.18	2.47	2.65	6.79	8.80	0.69	16.34	0.331	74	4.10	298	67
11312	J231225.98+135450.1	–	0.0339	10.44	2.40	2.54	7.54	9.17	0.19	15.16	0.526	60	5.60	3264	48
11193	J231321.76+141648.8	–	0.0394	10.50	2.46	2.75	6.76	9.07	0.19	15.57	0.296	77	5.41	4965	88
11192	J231340.27+140127.7	–	0.0399	10.56	1.16	1.00	1.83	9.77	0.18	17.19	0.804	37	3.67	3264	70
11284	J231545.95+133035.6	–	0.0394	10.34	3.03	3.25	7.93	8.72	0.17	16.23	0.234	83	5.13	3335	88
11292	J231608.02+134918.4	–	0.0389	10.54	2.89	3.02	8.12	8.98	0.17	15.31	0.488	63	4.56	3335	69
11291	J231616.05+135042.9	–	0.0386	10.39	2.38	2.69	8.05	9.00	0.17	15.62	0.372	71	3.01	3335	82
11347	J231647.75+153459.7	–	0.0388	10.87	3.11	3.12	9.36	9.25	0.13	14.56	0.541	59	5.81	4851	15
11444	J232114.19+131851.2	–	0.0420	10.69	6.15	7.56	17.62	8.40	0.25	15.18	0.514	61	3.63	1682	48
11410	J232222.95+135938.2	–	0.0415	10.55	2.53	2.66	8.53	9.05	0.13	15.23	0.787	39	5.72	1676	86
11435	J232321.31+141704.4	–	0.0434	10.97	4.80	5.30	14.70	8.87	0.11	14.71	0.387	70	4.66	1676	15
11434	J232326.70+140753.9	–	0.0417	10.96	5.25	5.84	14.81	8.81	0.13	14.24	0.728	44	3.49	1676	14
11636	J232331.69+151401.6	–	0.0394	10.10	2.87	3.04	7.71	8.54	0.20	16.08	0.886	28	4.30	3180	89
11395	J232337.45+133908.1	–	0.0425	10.77	2.34	2.47	8.15	9.32	0.19	15.30	0.921	23	5.40	1676	34
11509	J232407.17+145006.6	–	0.0384	10.50	4.06	4.49	11.62	8.65	0.15	15.15	0.519	61	4.36	1681	80
11524	J232423.53+152636.3	–	0.0256	10.41	3.20	3.44	10.30	9.14	0.14	14.65	0.419	68	5.52	3180	15
11585	J232516.78+142135.6	–	0.0445	11.08	3.09	3.36	11.34	9.34	0.11	14.51	0.686	48	6.09	1681	10
11544	J232538.54+152115.9	IC 1488	0.0412	11.22	5.48	5.86	17.42	9.06	0.19	14.48	0.213	86	5.95	208	4
11676	J232711.15+144546.3	–	0.0418	10.58	3.51	4.07	11.27	8.79	0.15	15.95	0.371	71	4.37	1681	77
11669	J232713.50+152831.1	–	0.0466	10.74	5.17	5.80	12.32	8.51	0.17	15.01	0.835	34	3.20	208	60
11685	J232749.71+150709.1	–	0.0419	11.16	7.54	8.74	20.31	8.71	0.20	14.02	0.586	56	4.39	208	5
11571	J232934.08+132718.3	–	0.0337	10.28	5.13	5.48	11.94	8.36	0.15	15.04	0.668	49	2.80	109	46
11573	J233011.60+132656.3	–	0.0386	10.47	3.75	4.95	11.81	8.69	0.17	15.49	0.494	63	3.69	109	81
11568	J233013.51+132801.7	–	0.0417	11.19	3.58	3.91	12.59	9.39	0.17	14.11	0.628	53	5.56	109	5
11567	J233019.67+132657.4	–	0.0399	11.22	4.40	4.69	15.29	9.27	0.17	13.87	0.722	45	5.69	109	3
11791	J235159.08+144504.1	–	0.0466	10.95	3.74	4.26	13.09	9.00	0.09	14.96	0.918	24	4.67	1699	23

Downloaded from http://mnras.oxfordjournals.org/ at Swinburne University of Technology on August 11, 2014

Column 9: base-10 logarithm of the stellar mass surface density, μ_*, in M$_\odot$ kpc^{-2}. This quantity is defined as $\mu_* = M_*/(2\pi R_{50,z}^2)$, with $R_{50,\,z}$ in kpc units.

Column 10: Galactic extinction in r band, ext$_r$, in magnitudes, from SDSS.

Column 11: r-band model magnitude from SDSS, r, corrected for Galactic extinction.

Column 12: minor-to-major axial ratio from the exponential fit in r band, $(b/a)_r$, from SDSS.

Column 13: inclination to the line-of-sight, in degrees (see Catinella et al. 2012b for details).

Column 14: NUV$-r$ observed colour from our reprocessed photometry, corrected for Galactic extinction.

Column 15: exposure time of *GALEX* NUV image, $T_{\rm NUV}$, in seconds.

Column 16: maximum on-source integration time, $T_{\rm max}$, required to reach the limiting H I mass fraction, in minutes (see Section 2). Given the H I mass limit and redshift of each galaxy, $T_{\rm max}$ is computed assuming a 5σ signal with 300 km s^{-1} velocity width and the instrumental parameters typical of our observations (i.e. gain ~10 K Jy^{-1} and system temperature ~28 K at 1370 MHz).

H I source catalogues

This data release includes 147 detections and 103 non-detections, for which we provide upper limits below.

The measured H I parameters for the detected galaxies are listed in Table A2, ordered by increasing right ascension:

Columns 1 and 2: GASS and SDSS identifiers.

Column 3: SDSS redshift, $z_{\rm SDSS}$.

Column 4: on-source integration time of the Arecibo observation, $T_{\rm on}$, in minutes. This number refers to *on scans* that were actually combined, and does not account for possible losses due to RFI excision (usually negligible).

Column 5: velocity resolution of the final, smoothed spectrum in km s^{-1}.

Column 6: redshift, z, measured from the H I spectrum. The error on the corresponding heliocentric velocity, cz, is half the error on the width, tabulated in the following column.

Column 7: observed velocity width of the source line profile in km s^{-1}, W_{50}, measured at the 50 per cent level of each peak. The error on the width is the sum in quadrature of the statistical and systematic uncertainties in km s^{-1}. Statistical errors depend primarily on the signal to noise of the H I spectrum, and are obtained from the rms noise of the linear fits to the edges of the H I profile. Systematic errors depend on the subjective choice of the H I signal boundaries (see DR1 paper), and are negligible for most of the galaxies in our sample (see also Appendix B).

Column 8: velocity width corrected for instrumental broadening and cosmological redshift only, $W_{50}{}^c$, in km s^{-1} (see Catinella et al. 2012b for details). No inclination or turbulent motion corrections are applied.

Column 9: observed, integrated H I-line flux density in Jy km s^{-1}, $F \equiv \int S{\rm d}v$, measured on the smoothed and baseline-subtracted spectrum. The reported uncertainty is the sum in quadrature of the statistical and systematic errors (see column 7). The statistical errors are calculated according to equation 2 of S05 (which includes the contribution from uncertainties in the baseline fit).

Column 10: rms noise of the observation in mJy, measured on the signal- and RFI-free portion of the smoothed spectrum.

Column 11: signal-to-noise ratio of the H I spectrum, S/N, estimated following Saintonge (2007) and adapted to the velocity resolution of the spectrum. This is the definition of S/N adopted by ALFALFA, which accounts for the fact that for the same peak flux a broader spectrum has more signal.

Column 12: base-10 logarithm of the H I mass, $M_{\rm H\,I}$, in solar units (see Catinella et al. 2012b for details).

Column 13: base-10 logarithm of the H I mass fraction, $M_{\rm H\,I}/M_*$.

Column 14: quality flag, Q (1 = good, 2 = marginal, 3 = marginal and confused, 5 = confused). An asterisk indicates the presence of a note for the source in Appendix B. Code 1 indicates reliable detections, with an S/N ratio of the order of 6.5 or higher. Marginal detections have lower S/N, thus more uncertain H I parameters, but are still secure detections, with H I redshift consistent with the SDSS one. We flag galaxies as 'confused' when most of the H I emission is believed to originate from another source within the Arecibo beam. For some of the galaxies, the presence of small companions within the beam might contaminate (but is unlikely to dominate) the H I signal – this is just noted in Appendix B.

Table A3 gives the derived H I upper limits for the non-detections. Columns 1–4 and 5 are the same as columns 1–4 and 10 in Table A2, respectively. Column 6 lists the upper limit on the H I mass in solar units, log $M_{\rm H\,I,lim}$, computed assuming a 5σ signal with 300 km s^{-1} velocity width, if the spectrum was smoothed to 150 km s^{-1}. Column 7 gives the corresponding upper limit on the gas fraction, log $M_{\rm H\,I,lim}/M_*$. An asterisk in column 8 indicates the presence of a note for the galaxy in Appendix B.

SDSS postage stamps and H I spectra

SDSS images and H I spectra of the galaxies are presented here, organized as follows: H I detections with quality flag 1 in Table A2 (Fig. A1), marginal and/or confused detections with quality flags 2–5 (Fig. A2) and non-detections (Fig. A3). The objects in each of these figures are ordered by increasing GASS number (indicated on the top-right corner of each spectrum). The SDSS images show a 1 arcmin^2 field, i.e. only the central part of the region sampled by the Arecibo beam (the half-power full width of the beam is ~3.5 arcmin at the frequencies of our observations). Therefore, companions that might be detected in our spectra typically are not visible in the postage stamps, but they are noted in Appendix B. The H I spectra are always displayed over a 3000 km s^{-1} velocity interval, which includes the full 12.5 MHz bandwidth adopted for our observations. The H I-line profiles are calibrated, smoothed (to a velocity resolution between 5 and 21 km s^{-1} for the detections, as listed in Table A2, or to ~15 km s^{-1} for the non-detections), and baseline subtracted. A red, dotted line indicates the heliocentric velocity corresponding to the optical redshift from SDSS. In Figs A1–A2, the shaded area and two vertical dashes show the part

Downloaded from http://mnras.oxfordjournals.org/ at Swinburne University of Technology on August 11, 2014

Table A2. H I properties of GASS detections.

GASS (1)	SDSS ID (2)	z_{SDSS} (3)	T_{on} (min) (4)	Δv (km s^{-1}) (5)	z (6)	W_{50} (km s^{-1}) (7)	$W_{50}{}^{c}$ (km s^{-1}) (8)	F (Jy km s^{-1}) (9)	rms (mJy) (10)	S/N (11)	log M_{HI} (M$_{\odot}$) (12)	log M_{HI}/M_* (13)	Q (14)
11910	J000632.57+154004.7	0.0370	14	13	0.037 052	317 ± 1	300	0.45 ± 0.06	0.41	12.1	9.43	−0.85	1
12062	J002556.06+153815.0	0.0365	5	13	0.036 445	255 ± 12	240	1.18 ± 0.09	0.64	22.9	9.84	−0.25	1*
3305	J005709.66+143906.6	0.0494	5	13	0.049 501	403 ± 6	378	1.30 ± 0.13	0.75	16.9	10.15	−0.56	1
3284	J010253.84+141140.3	0.0397	53	16	0.039 637	289 ± 7	271	0.23 ± 0.03	0.20	12.3	9.20	−1.40	1
3666	J011803.07+153224.4	0.0382	10	13	0.038 173	295 ± 8	278	0.60 ± 0.07	0.49	14.1	9.59	−0.66	1*
3792	J012842.03+143633.2	0.0364	15	13	0.036 442	416 ± 2	396	0.49 ± 0.07	0.39	11.9	9.45	−1.36	1
27250	J013006.16+131702.1	0.0380	10	13	0.037 986	76 ± 6	67	0.58 ± 0.04	0.53	24.9	9.57	−0.67	1
27284	J013204.58+153001.2	0.0440	10	13	0.043 984	358 ± 12	336	0.74 ± 0.08	0.47	16.2	9.80	−1.15	1
3851	J013851.94+150258.8	0.0278	15	15	0.028 420	380 ± 11	362	0.40 ± 0.07	0.37	9.9	9.15	−1.44	5*
4111	J014601.79+141421.0	0.0441	4	13	0.044 131	251 ± 4	235	0.61 ± 0.10	0.75	10.0	9.72	−1.17	1*
4165	J015046.48+134127.5	0.0441	29	16	0.044 554	307 ± 1	287	0.25 ± 0.04	0.26	9.8	9.34	−1.49	5*
4163	J015244.40+131133.3	0.0262	5	13	0.026 201	241 ± 1	229	1.29 ± 0.09	0.69	24.0	9.59	−0.63	1
4134	J015606.45+123403.2	0.0445	30	13	0.044 484	376 ± 19	354	0.41 ± 0.05	0.29	14.5	9.55	−1.09	1
4136	J015703.78+131001.4	0.0323	16	15	0.032 649	185 ± 38	172	0.20 ± 0.04	0.31	8.5	8.97	−1.88	5*
4132	J015742.52+132318.8	0.0443	15	16	0.044 231	429 ± 18	404	0.65 ± 0.06	0.33	16.5	9.75	−1.07	1
3917	J015755.84+132129.3	0.0444	20	21	0.044 457	227 ± 3	207	0.09 ± 0.04	0.25	3.7	8.90	−2.05	2*
3936	J015945.90+134652.6	0.0441	18	16	0.044 144	248 ± 12	230	0.30 ± 0.05	0.35	9.6	9.41	−0.71	1*
3960	J020351.38+144534.3	0.0321	8	13	0.032 172	231 ± 7	218	0.61 ± 0.07	0.53	15.1	9.45	−0.58	1*
3966	J020455.76+140055.4	0.0310	34	13	0.031 305	271 ± 7	257	0.18 ± 0.04	0.26	8.1	8.88	−1.65	5*
4008	J020829.86+124359.9	0.0347	5	13	0.034 677	255 ± 3	240	1.55 ± 0.08	0.61	31.5	9.91	−0.58	1
3987	J021337.66+132741.5	0.0420	28	13	0.041 602	303 ± 3	285	0.26 ± 0.04	0.30	9.9	9.30	−1.50	5*
4056	J021349.29+135035.7	0.0375	72	16	0.037 049	217 ± 17	202	0.08 ± 0.02	0.17	5.3	8.66	−1.76	2*
12069	J073906.01+290936.2	0.0388	5	13	0.038 927	212 ± 5	198	1.50 ± 0.09	0.74	27.6	10.00	−1.13	1
21842	J074533.96+184812.0	0.0450	12	16	0.045 075	450 ± 7	423	0.55 ± 0.09	0.44	9.9	9.70	−1.36	1
51334	J075329.53+140122.8	0.0294	4	13	0.029 414	320 ± 8	304	0.98 ± 0.11	0.76	14.4	9.57	−0.53	1*
51351	J075457.85+142718.8	0.0293	8	15	0.029 280	523 ± 2	501	1.31 ± 0.12	0.58	15.8	9.69	−1.32	1
51336	J075617.10+143609.6	0.0474	19	21	0.047 309	467 ± 2	436	0.25 ± 0.07	0.29	5.5	9.39	−1.61	2
51580	J080403.84+150518.4	0.0390	20	16	0.038 927	331 ± 2	311	0.21 ± 0.05	0.31	6.7	9.15	−1.09	1*
14247	J080528.11+355648.1	0.0330	8	13	0.033 040	480 ± 6	458	0.93 ± 0.13	0.71	10.8	9.65	−1.49	1*
51899	J083131.52+192228.3	0.0387	10	13	0.039 004	439 ± 4	416	1.08 ± 0.09	0.49	19.7	9.86	−0.15	5*
52045	J083836.42+173809.2	0.0415	4	13	0.041 499	120 ± 2	109	0.81 ± 0.08	0.83	17.5	9.79	−0.38	1*
32308	J083934.43+252837.6	0.0292	8	13	0.029 284	89 ± 4	81	0.26 ± 0.05	0.66	8.2	8.99	−1.03	1*
56509	J085045.27+114839.0	0.0297	15	13	0.029 791	411 ± 5	393	1.00 ± 0.08	0.50	19.5	9.59	−0.89	1*
8096	J085254.99+030908.4	0.0345	5	15	0.034 417	320 ± 29	301	0.92 ± 0.13	0.79	11.7	9.68	−0.60	1*
19989	J085425.62+081241.0	0.0294	30	15	0.029 674	135 ± 9	124	0.12 ± 0.03	0.29	6.4	8.66	−1.80	1*
52297	J085724.03+204237.9	0.0328	8	13	0.032 899	374 ± 8	356	0.63 ± 0.10	0.63	10.4	9.48	−1.01	1*
56662	J090254.93+133938.5	0.0299	20	15	0.029 924	329 ± 26	312	0.28 ± 0.05	0.31	9.1	9.04	−1.20	1*
20041	J091427.70+080445.9	0.0309	35	15	0.030 998	400 ± 6	381	0.33 ± 0.05	0.24	12.1	9.14	−0.89	5*
20042	J091444.06+083605.3	0.0468	60	16	0.046 879	165 ± 6	150	0.11 ± 0.02	0.19	8.2	9.04	−0.97	1
16815	J091831.34+065223.3	0.0393	20	13	0.039 284	368 ± 10	348	0.42 ± 0.05	0.34	12.9	9.45	−1.18	1

Downloaded from http://mnras.oxfordjournals.org/ at Swinburne University of Technology on August 11, 2014

Table A2 – *continued*

GASS (1)	SDSS ID (2)	$z_{\rm SDSS}$ (3)	$T_{\rm on}$ (min) (4)	Δv (km s^{-1}) (5)	z (6)	W_{50} (km s^{-1}) (7)	$W_{50}{}^{c}$ (km s^{-1}) (8)	F (Jy km s^{-1}) (9)	rms (mJy) (10)	S/N (11)	log $M_{\rm H\,I}$ (M$_\odot$) (12)	log $M_{\rm H\,I}/M_*$ (13)	Q (14)
19672	J091929.51+341810.2	0.0458	5	13	0.045 872	461 ± 3	434	1.34 ± 0.16	0.86	13.3	10.10	−0.63	1*
32937	J092708.07+292408.2	0.0258	5	13	0.025 831	286 ± 6	272	0.82 ± 0.11	0.81	12.0	9.38	−1.07	1
32907	J093009.18+285351.3	0.0349	20	15	0.034 934	355 ± 13	336	0.42 ± 0.07	0.42	9.6	9.35	−1.12	1
33214	J093624.28+320445.5	0.0269	20	15	0.027 319	256 ± 22	241	0.16 ± 0.05	0.36	5.2	8.72	−1.62	2*
55745	J093710.07+165837.9	0.0278	8	21	0.027 813	298 ± 6	280	0.25 ± 0.08	0.45	5.1	8.94	−1.98	2*
8349	J093953.62+034850.2	0.0285	29	15	0.028 783	341 ± 4	324	0.18 ± 0.05	0.27	6.6	8.82	−1.55	1
22822	J095144.91+353719.6	0.0270	5	13	0.027 185	346 ± 6	331	2.70 ± 0.16	0.99	29.2	9.94	−0.62	1
20376	J095416.82+103457.5	0.0399	73	16	0.040 141	164 ± 1	150	0.06 ± 0.02	0.16	5.4	8.65	−1.89	2*
33737	J095851.33+320423.0	0.0270	4	10	0.026 078	232 ± 3	222	2.97 ± 0.10	0.87	50.6	9.95	−0.74	1*
8634	J101324.41+050131.7	0.0464	45	13	0.046 469	387 ± 3	363	0.30 ± 0.04	0.24	12.6	9.46	−0.67	1*
26407	J102138.86+131845.6	0.0461	15	13	0.046 205	405 ± 3	381	0.40 ± 0.07	0.38	10.1	9.58	−1.45	1*
26406	J102149.72+132649.6	0.0322	4	15	0.032 289	361 ± 8	342	0.79 ± 0.15	0.83	9.0	9.56	−1.20	1*
26535	J102727.40+132526.2	0.0315	15	15	0.031 589	197 ± 13	184	0.37 ± 0.05	0.40	12.0	9.22	−0.84	1
23070	J102802.88+104630.4	0.0448	15	21	0.044 654	297 ± 19	274	0.18 ± 0.06	0.34	4.8	9.21	−1.81	2*
55541	J103246.99+211256.3	0.0429	10	13	0.042 826	414 ± 12	391	0.89 ± 0.11	0.62	13.8	9.86	−0.76	1*
26586	J103611.29+131025.3	0.0334	15	13	0.033 420	235 ± 9	221	0.38 ± 0.05	0.41	11.9	9.27	−0.79	1*
23213	J103621.90+115317.0	0.0293	20	13	0.029 327	330 ± 9	314	0.38 ± 0.05	0.35	11.8	9.15	−0.99	1
26569	J103808.15+131737.0	0.0319	25	15	0.032 112	298 ± 3	281	0.25 ± 0.04	0.28	9.3	9.05	−1.20	1
15257	J104805.79+060114.4	0.0288	24	15	0.028 847	237 ± 5	223	0.19 ± 0.04	0.26	8.6	8.84	−1.25	5*
8945	J105315.29+042003.1	0.0417	25	21	0.041 555	492 ± 2	462	0.25 ± 0.06	0.26	6.1	9.28	−1.55	2*
23496	J105721.59+120611.0	0.0477	4	13	0.047 793	295 ± 12	276	0.99 ± 0.11	0.72	15.7	10.00	−0.16	1*
17635	J105935.53+085536.5	0.0309	29	13	0.030 908	407 ± 3	389	0.31 ± 0.05	0.30	10.1	9.11	−1.37	1
17673	J105958.54+102312.4	0.0363	65	15	0.036 722	292 ± 0	274	0.10 ± 0.03	0.17	5.9	8.77	−1.55	3*
17622	J110043.97+090243.0	0.0354	18	15	0.035 435	323 ± 9	305	0.33 ± 0.06	0.37	9.0	9.26	−0.79	1*
34989	J110339.49+315129.4	0.0466	10	13	0.046 642	570 ± 2	539	2.01 ± 0.10	0.50	27.6	10.29	−0.75	1
48356	J111113.19+284147.0	0.0287	4	15	0.029 177	361 ± 65	343	0.70 ± 0.12	0.67	10.1	9.42	−1.83	5*
17824	J111404.85+090924.0	0.0342	29	13	0.034 214	332 ± 4	315	0.28 ± 0.05	0.31	10.1	9.17	−0.94	1
5701	J111509.40+024156.4	0.0442	20	13	0.044 244	459 ± 8	434	0.80 ± 0.07	0.40	17.0	9.84	−0.88	1*
48521	J111738.91+263506.0	0.0475	19	13	0.047 483	185 ± 2	171	0.25 ± 0.04	0.34	10.5	9.39	−0.90	1*
48518	J111750.72+263927.0	0.0285	25	15	0.027 409	657 ± 39	632	0.91 ± 0.07	0.29	17.1	9.48	−0.94	5*
24496	J111809.91+074653.9	0.0421	10	21	0.042 109	395 ± 14	369	0.76 ± 0.08	0.38	15.6	9.77	−0.83	1*
5848	J112142.43+033424.5	0.0391	10	13	0.039 110	374 ± 1	354	0.89 ± 0.10	0.62	14.6	9.78	−0.66	1
23703	J112731.58+120834.3	0.0459	35	13	0.046 082	461 ± 7	434	0.42 ± 0.05	0.27	12.9	9.59	−1.15	1*
48604	J112746.27+265734.5	0.0334	5	13	0.033 400	377 ± 4	359	1.22 ± 0.11	0.70	17.8	9.78	−0.82	1*
6015	J113524.48+021627.3	0.0289	20	13	0.028 967	267 ± 1	253	0.41 ± 0.07	0.53	9.4	9.18	−1.05	1*
23739	J113706.07+115237.7	0.0358	12	15	0.035 465	321 ± 1	302	0.32 ± 0.06	0.38	8.5	9.25	−1.65	1*
23789	J114144.66+122937.1	0.0342	55	15	0.034 194	420 ± 5	399	0.16 ± 0.04	0.20	6.9	8.92	−1.49	5*
23781	J114212.30+113041.1	0.0432	15	16	0.042 980	438 ± 8	413	0.58 ± 0.07	0.36	13.2	9.67	−0.95	5*
48994	J114218.00+301349.0	0.0322	5	10	0.032 286	392 ± 4	375	4.41 ± 0.17	1.15	43.2	10.31	−0.42	1*
23815	J115036.65+112151.9	0.0306	20	13	0.030 651	323 ± 1	307	0.49 ± 0.05	0.36	14.9	9.30	−0.93	1*
18084	J115112.59+085311.6	0.0351	60	15	0.035 164	282 ± 9	265	0.12 ± 0.03	0.18	7.3	8.82	−1.52	1*
49433	J115536.63+292104.4	0.0458	49	21	0.045 765	290 ± 15	267	0.20 ± 0.03	0.16	11.0	9.27	−1.18	1
49386	J115913.81+305325.8	0.0294	27	15	0.029 527	281 ± 9	266	0.29 ± 0.04	0.27	11.6	9.04	−1.49	1*

Downloaded from http://mnras.oxfordjournals.org/ at Swinburne University of Technology on August 11, 2014

Table A2 – *continued*

GASS (1)	SDSS ID (2)	$z_{\rm SDSS}$ (3)	$T_{\rm on}$ (min) (4)	Δv (km s^{-1}) (5)	z (6)	W_{50} (km s^{-1}) (7)	$W_{50}{}^c$ (km s^{-1}) (8)	F (Jy km s^{-1}) (9)	rms (mJy) (10)	S/N (11)	log $M_{\rm H\,I}$ (M$_\odot$) (12)	log $M_{\rm H\,I}/M_*$ (13)	Q (14)
18138	J120239.51+085624.2	0.0347	30	21	0.034 827	454 ± 4	429	0.16 ± 0.05	0.21	5.2	8.94	−1.70	2*
49727	J120445.20+311132.9	0.0250	10	15	0.025 875	610 ± 36	587	1.56 ± 0.11	0.47	19.7	9.66	−0.61	5*
18131	J120445.85+092521.1	0.0353	55	15	0.035 668	68 ± 2	58	0.05 ± 0.01	0.18	6.0	8.44	−1.90	2*
18225	J120511.42+103341.0	0.0334	54	15	0.033 446	191 ± 8	178	0.08 ± 0.03	0.19	5.3	8.59	−1.55	2*
28062	J122800.84+081108.1	0.0377	30	16	0.037 733	336 ± 17	316	0.29 ± 0.05	0.27	10.5	9.26	−1.44	5*
50404	J123409.10+280750.5	0.0400	45	13	0.039 994	139 ± 7	128	0.14 ± 0.02	0.24	9.6	8.99	−1.56	1*
50406	J123653.92+274456.8	0.0258	15	13	0.025 781	232 ± 12	220	0.37 ± 0.05	0.42	11.6	9.04	−1.37	1*
50550	J124128.01+284728.3	0.0350	9	15	0.035 114	302 ± 2	285	0.48 ± 0.08	0.47	10.6	9.42	−0.87	1
40495	J125626.93+093604.5	0.0459	24	21	0.046 039	297 ± 33	274	0.14 ± 0.05	0.26	4.7	9.11	−1.81	2*
40502	J125752.83+101754.6	0.0363	10	13	0.036 272	344 ± 5	325	0.90 ± 0.10	0.64	15.0	9.72	−0.47	1*
35437	J130125.07+284038.0	0.0291	10	13	0.029 200	136 ± 6	126	0.42 ± 0.05	0.52	13.7	9.19	−1.04	1
6679	J130210.77+030623.6	0.0472	20	13	0.047 236	275 ± 10	256	0.47 ± 0.05	0.38	14.6	9.67	−1.36	1*
13159	J130525.44+035929.7	0.0437	80	16	0.043 717	286 ± 12	266	0.28 ± 0.03	0.20	15.1	9.38	−0.99	1*
40647	J130624.82+095635.8	0.0487	60	13	0.048 734	363 ± 8	340	0.26 ± 0.03	0.20	13.4	9.44	−1.29	1
25215	J131032.19+110121.0	0.0427	5	13	0.042 796	395 ± 4	372	0.59 ± 0.12	0.69	8.5	9.68	−0.91	1*
44354	J132050.70+313700.6	0.0448	5	13	0.044 821	298 ± 6	279	1.76 ± 0.10	0.67	30.0	10.19	−0.49	1
51150	J132259.87+270659.1	0.0345	10	15	0.034 400	259 ± 20	243	0.42 ± 0.07	0.44	10.7	9.34	−1.46	1*
51161	J132522.77+271456.7	0.0345	5	15	0.034 577	260 ± 6	244	0.61 ± 0.11	0.76	8.9	9.50	−0.65	1*
43963	J134142.40+300731.5	0.0370	5	13	0.037 112	309 ± 9	292	1.14 ± 0.11	0.71	18.1	9.84	−1.21	1
38018	J134834.19+245329.2	0.0297	4	13	0.029 694	344 ± 3	328	0.72 ± 0.11	0.73	10.7	9.45	−0.63	1
35981	J135308.35+354250.5	0.0411	5	5	0.041 152	376 ± 3	359	3.45 ± 0.14	1.33	42.2	10.41	0.11	1
44856	J135411.14+243322.5	0.0286	25	15	0.028 646	301 ± 18	285	0.49 ± 0.05	0.29	17.8	9.25	−0.80	1*
13618	J135622.01+043710.6	0.0339	49	15	0.033 857	226 ± 12	211	0.10 ± 0.03	0.21	6.0	8.72	−1.48	3*
13674	J135815.23+035953.8	0.0300	4	21	0.030 004	289 ± 11	270	0.78 ± 0.12	0.67	10.6	9.49	−0.61	1*
9317	J140430.25+050629.4	0.0295	5	13	0.029 490	170 ± 9	159	0.65 ± 0.07	0.66	15.0	9.39	−0.65	1
38458	J140603.77+123016.2	0.0387	80	21	0.038 176	693 ± 15	658	0.29 ± 0.03	0.12	10.6	9.27	−1.14	5*
7121	J140642.63+015452.2	0.0472	85	21	0.047 163	323 ± 4	298	0.08 ± 0.03	0.17	4.2	8.91	−1.33	2*
45254	J141830.77+291012.3	0.0349	9	15	0.034 914	401 ± 20	380	0.85 ± 0.09	0.46	16.4	9.66	−1.37	1
7405	J141837.70+020245.4	0.0256	10	12	0.025 494	381 ± 12	366	1.34 ± 0.09	0.58	23.6	9.58	−0.95	1*
28703	J142802.34+120134.9	0.0267	15	13	0.026 712	290 ± 7	277	0.37 ± 0.06	0.41	10.5	9.06	−1.10	1*
9615	J143001.87+032352.1	0.0333	20	13	0.033 333	274 ± 2	259	0.52 ± 0.06	0.41	15.1	9.41	−0.74	1*
38198	J143134.60+244053.6	0.0378	10	13	0.037 903	444 ± 3	421	0.79 ± 0.08	0.47	14.8	9.70	−0.95	1*
31095	J143749.60+064454.3	0.0290	4	13	0.028 963	258 ± 5	245	1.10 ± 0.11	0.85	16.0	9.61	−0.47	1*
9938	J144140.50+040347.1	0.0275	20	13	0.027 482	123 ± 0	114	0.16 ± 0.04	0.41	6.9	8.71	−1.37	1
41699	J144213.77+084036.0	0.0341	12	15	0.034 344	65 ± 1	56	0.08 ± 0.03	0.35	5.1	8.62	−2.30	2
9942	J144325.65+042244.6	0.0264	9	21	0.026 518	544 ± 2	520	0.29 ± 0.10	0.40	4.2	8.95	−1.87	3*
41718	J144338.96+083350.7	0.0346	50	15	0.035 164	112 ± 5	101	0.12 ± 0.02	0.20	9.9	8.81	−1.65	1*
10032	J145024.11+043655.2	0.0468	51	16	0.046 652	369 ± 14	345	0.26 ± 0.04	0.20	12.2	9.40	−1.42	1*
42233	J145304.36+310406.0	0.0323	15	13	0.032 279	360 ± 9	343	0.57 ± 0.07	0.41	14.7	9.42	−1.07	1*
10005	J145307.29+033217.4	0.0334	50	21	0.033 306	362 ± 2	340	0.12 ± 0.04	0.17	5.9	8.78	−1.69	2*
42191	J145403.73+305046.4	0.0320	40	15	0.031 869	206 ± 44	192	0.15 ± 0.04	0.25	7.4	8.82	−1.30	1*
41743	J150204.10+064922.9	0.0462	20	13	0.046 269	345 ± 3	324	0.42 ± 0.06	0.37	12.1	9.60	−0.85	1

Downloaded from http://mnras.oxfordjournals.org/ at Swinburne University of Technology on August 11, 2014

Table A2 – *continued*

GASS (1)	SDSS ID (2)	z_{SDSS} (3)	T_{on} (min) (4)	Δv (km s^{-1}) (5)	z (6)	W_{50} (km s^{-1}) (7)	$W_{50}{}^c$ (km s^{-1}) (8)	F (Jy km s^{-1}) (9)	rms (mJy) (10)	S/N (11)	log $M_{H\,I}$ (M$_\odot$) (12)	log $M_{H\,I}/M_*$ (13)	Q (14)
39082	J150721.51+095541.0	0.0352	9	15	0.035 525	273 ± 7	256	0.29 ± 0.08	0.50	6.4	9.21	−1.81	2*
41869	J150921.50+070439.8	0.0414	29	13	0.041 479	314 ± 2	296	0.25 ± 0.04	0.29	9.9	9.29	−0.86	1*
41863	J151028.90+072455.4	0.0322	5	13	0.032 382	365 ± 7	347	1.40 ± 0.10	0.65	22.3	9.81	−0.30	5*
7813	J151243.59+012752.2	0.0293	12	13	0.029 083	245 ± 12	232	0.51 ± 0.08	0.58	11.1	9.27	−1.52	1*
28317	J154408.13+274024.3	0.0316	20	13	0.031 915	218 ± 2	205	0.28 ± 0.05	0.38	9.9	9.09	−0.98	1*
25721	J155506.74+093023.0	0.0341	44	21	0.034 207	341 ± 3	319	0.15 ± 0.04	0.20	6.1	8.88	−1.21	2*
11086	J225524.42+131453.8	0.0329	15	13	0.032 889	354 ± 2	336	0.44 ± 0.07	0.45	10.2	9.32	−1.11	1*
11312	J231225.98+135450.1	0.0339	16	13	0.034 147	487 ± 4	465	0.74 ± 0.07	0.39	15.4	9.58	−0.86	5*
11193	J231321.76+141648.8	0.0394	85	16	0.039 671	376 ± 3	354	0.10 ± 0.03	0.17	5.2	8.82	−1.68	2*
11192	J231340.27+140127.7	0.0399	9	13	0.039 981	339 ± 16	320	1.01 ± 0.07	0.47	22.9	9.85	−0.71	5
11292	J231608.02+134918.4	0.0389	64	16	0.038 807	458 ± 2	434	0.31 ± 0.04	0.18	13.4	9.32	−1.22	5*
11291	J231616.05+135042.9	0.0386	5	16	0.038 580	362 ± 11	341	0.86 ± 0.11	0.60	13.6	9.75	−0.64	1*
11347	J231647.75+153459.7	0.0388	10	13	0.038 947	474 ± 6	450	0.95 ± 0.09	0.47	17.0	9.80	−1.07	5*
11444	J232114.19+131851.2	0.0420	5	10	0.042 059	173 ± 2	161	1.17 ± 0.07	0.68	28.9	9.96	−0.73	1
11435	J232321.31+141704.4	0.0434	16	16	0.043 500	521 ± 1	491	0.32 ± 0.07	0.33	6.7	9.42	−1.55	1*
11434	J232326.70+140753.9	0.0417	15	13	0.041 839	392 ± 9	370	0.73 ± 0.06	0.38	18.8	9.75	−1.21	1*
11509	J232407.17+145006.6	0.0384	80	21	0.038 126	283 ± 28	263	0.08 ± 0.02	0.14	5.5	8.72	−1.78	2*
11676	J232711.15+144546.3	0.0418	15	13	0.041 816	377 ± 2	356	0.47 ± 0.07	0.42	11.4	9.56	−1.02	1
11669	J232713.50+152831.1	0.0466	5	13	0.046 592	149 ± 3	137	0.45 ± 0.07	0.66	11.0	9.64	−1.10	1*
11685	J232749.71+150709.1	0.0419	10	16	0.041 926	388 ± 22	365	0.76 ± 0.09	0.47	14.8	9.77	−1.39	1
11571	J232934.08+132718.3	0.0337	5	13	0.033 577	252 ± 5	238	1.46 ± 0.09	0.70	26.2	9.86	−0.43	1
11573	J233011.60+132656.3	0.0386	80	21	0.038 617	250 ± 4	230	0.08 ± 0.02	0.14	5.2	8.70	−1.77	2*

Downloaded from http://mnras.oxfordjournals.org/ at Swinburne University of Technology on August 11, 2014

Table A3. GASS non-detections.

GASS (1)	SDSS ID (2)	$z_{\rm SDSS}$ (3)	$T_{\rm on}$ (min) (4)	rms (mJy) (5)	log $M_{\rm HI,lim}$ ($M_{\odot}$) (6)	log $M_{\rm HI,lim}/M_*$ (7)	Note (8)
11892	J000200.82+150132.1	0.0357	46	0.21	8.76	−1.78	*
11903	J000458.72+154018.2	0.0373	65	0.18	8.73	−1.44	*
12030	J001842.68+151142.6	0.0372	34	0.26	8.88	−1.77	–
3157	J003032.94+145635.4	0.0381	55	0.20	8.80	−1.77	*
3258	J005316.95+160556.1	0.0393	68	0.17	8.74	−1.53	*
3321	J010228.41+154457.0	0.0403	14	0.42	9.16	−1.69	–
3634	J011347.63+153029.8	0.0453	25	0.29	9.11	−1.78	–
3773	J012153.31+145344.6	0.0362	43	0.23	8.80	−1.76	–
4130	J015720.03+131013.4	0.0448	35	0.25	9.03	−1.78	*
3957	J020325.71+133910.7	0.0325	45	0.21	8.68	−1.46	–
3956	J020353.23+134011.9	0.0327	28	0.27	8.78	−1.81	–
3972	J020539.16+143907.7	0.0429	8	0.51	9.30	−1.85	*
4014	J020720.31+130154.4	0.0482	23	0.29	9.17	−1.81	*
3980	J021423.65+122015.6	0.0408	14	0.37	9.12	−1.83	*
14260	J074158.62+231035.0	0.0431	10	0.51	9.31	−1.75	*
14017	J074426.50+291609.7	0.0396	15	0.42	9.15	−1.77	*
51462	J075600.62+141144.6	0.0357	4	0.73	9.30	−1.80	*
19132	J080020.05+222634.8	0.0350	50	0.24	8.79	−1.56	–
56320	J080342.27+100159.7	0.0337	55	0.20	8.68	−1.53	*
19274	J081625.36+255928.8	0.0453	4	0.69	9.49	−1.83	*
56486	J084528.61+143425.6	0.0360	60	0.17	8.68	−1.57	–
56612	J090307.74+134149.4	0.0290	25	0.29	8.71	−1.56	*
56650	J090308.20+133103.9	0.0289	25	0.29	8.71	−1.53	*
20026	J090610.15+082343.3	0.0457	80	0.21	8.97	−1.49	–
16756	J091717.67+064151.5	0.0333	45	0.22	8.72	−1.71	*
33019	J092533.76+272050.9	0.0484	10	0.45	9.36	−1.79	–
53269	J093116.00+263259.6	0.0458	18	0.32	9.17	−1.81	*
20165	J093231.96+094957.3	0.0498	50	0.21	9.06	−1.76	*
20149	J093647.77+100551.1	0.0494	30	0.27	9.16	−1.75	*
33469	J095009.35+333409.5	0.0270	10	0.50	8.88	−1.73	*
20445	J095429.64+103530.1	0.0397	34	0.26	8.95	−1.76	*
26017	J095641.82+111144.6	0.0416	44	0.23	8.93	−1.78	*
33777	J100250.75+323840.2	0.0477	80	0.17	8.94	−1.16	*
54240	J102253.59+243623.0	0.0463	10	0.45	9.32	−1.81	*
26503	J102314.32+125224.0	0.0329	35	0.26	8.79	−1.66	*
26436	J102413.51+131444.8	0.0326	40	0.23	8.72	−1.28	–
23029	J102705.85+110317.5	0.0323	5	0.61	9.13	−1.77	*
5204	J102750.83+023634.0	0.0285	25	0.33	8.75	−1.65	*
23102	J102949.21+115144.4	0.0386	80	0.15	8.67	−1.51	*
54577	J103018.65+273422.9	0.0480	20	0.31	9.20	−1.80	*
23203	J103549.90+121212.7	0.0371	10	0.43	9.10	−1.82	*
23302	J104248.63+110000.8	0.0295	28	0.26	8.69	−1.74	–
8971	J104837.87+044756.4	0.0333	45	0.23	8.73	−1.42	*
34723	J105134.08+301221.8	0.0356	44	0.22	8.77	−1.80	–
8953	J105241.71+040913.9	0.0425	15	0.38	9.16	−1.79	*
15485	J110004.55+080622.2	0.0349	55	0.19	8.70	−1.43	–
23457	J110011.41+121015.1	0.0354	58	0.18	8.69	−1.43	*
47825	J111147.22+281602.2	0.0359	5	0.69	9.28	−1.77	–
48205	J111151.56+271156.0	0.0471	10	0.44	9.32	−1.80	*
48160	J111201.78+275053.8	0.0474	16	0.35	9.24	−1.79	*
23531	J111429.02+110847.8	0.0406	35	0.25	8.94	−1.80	*
12452	J112006.21+041035.6	0.0492	50	0.22	9.07	−1.75	*
48544	J112039.09+271737.4	0.0486	18	0.34	9.24	−1.81	*
23761	J113704.29+125535.7	0.0345	4	0.78	9.30	−1.77	–
18004	J115135.06+084507.6	0.0352	4	0.64	9.23	−1.89	*
18185	J120308.04+110920.4	0.0438	30	0.27	9.04	−1.79	–
18220	J120536.25+104113.3	0.0344	50	0.22	8.74	−1.76	*
28030	J122902.67+083133.3	0.0385	80	0.16	8.71	−1.31	*
12967	J123553.51+054723.4	0.0419	50	0.20	8.88	−1.69	*
50856	J125547.82+281521.9	0.0270	15	0.37	8.76	−1.64	–
50866	J125609.90+275039.3	0.0253	15	0.37	8.70	−1.79	*

Downloaded from http://mnras.oxfordjournals.org/ at Swinburne University of Technology on August 11, 2014

Table A3 – *continued*

GASS (1)	SDSS ID (2)	z_{SDSS} (3)	T_{on} (min) (4)	rms (mJy) (5)	log $M_{HI,lim}$ ($M_\odot$) (6)	log $M_{HI,lim}/M_*$ (7)	Note (8)
35497	J125650.61+285547.4	0.0270	20	0.30	8.66	−1.78	*
35475	J125935.67+283304.9	0.0253	15	0.38	8.71	−1.58	*
25213	J131222.82+114339.5	0.0320	40	0.22	8.67	−1.45	*
26936	J131525.21+152522.2	0.0266	5	0.59	8.94	−1.81	–
35659	J134159.72+294653.5	0.0449	8	0.56	9.38	−1.76	–
44021	J134231.07+301500.1	0.0363	5	0.66	9.27	−1.79	*
44892	J135609.30+251143.6	0.0290	12	0.44	8.89	−1.77	–
30746	J140908.49+061048.8	0.0363	60	0.22	8.79	−1.53	*
7310	J141657.47+021039.5	0.0261	15	0.42	8.78	−1.66	*
45940	J142748.88+262900.7	0.0325	40	0.22	8.70	−1.73	*
9607	J143043.65+031149.3	0.0268	23	0.32	8.68	−1.58	–
41621	J144011.86+081512.2	0.0296	30	0.25	8.66	−1.69	–
9702	J144043.35+032226.4	0.0319	10	0.48	9.02	−1.77	*
9695	J144216.88+034844.7	0.0257	16	0.38	8.72	−1.41	–
31131	J144248.49+063924.3	0.0279	20	0.28	8.67	−1.81	–
31478	J144350.25+313128.7	0.0335	45	0.23	8.75	−1.62	*
41723	J144605.27+085456.2	0.0295	10	0.47	8.94	−1.77	*
29371	J144907.58+105847.6	0.0292	10	0.45	8.91	−1.79	–
38935	J145458.46+114156.2	0.0305	9	0.42	8.92	−1.98	–
39014	J150513.62+084747.6	0.0449	12	0.42	9.26	−1.79	–
10211	J151219.92+031826.6	0.0469	20	0.35	9.22	−1.75	*
25057	J152106.26+304036.9	0.0308	33	0.24	8.68	−1.33	*
25115	J152112.78+303928.5	0.0308	30	0.24	8.68	−1.82	*
39407	J152239.21+083226.7	0.0366	60	0.23	8.83	−1.43	*
39532	J152346.52+083853.1	0.0301	30	0.27	8.71	−1.53	–
28348	J154051.59+282027.7	0.0329	38	0.24	8.74	−1.48	*
28327	J154129.97+275911.4	0.0320	4	0.72	9.19	−1.83	*
25682	J154811.74+090424.5	0.0393	57	0.21	8.84	−1.75	*
10918	J221421.77+135711.1	0.0261	4	0.68	8.99	−1.79	–
11080	J225608.33+130337.9	0.0290	25	0.29	8.71	−1.39	*
11249	J230757.92+152455.2	0.0362	63	0.19	8.72	−1.39	*
11257	J230806.95+152520.1	0.0368	63	0.17	8.69	−1.49	*
11284	J231545.95+133035.6	0.0394	84	0.15	8.70	−1.64	*
11410	J232222.95+135938.2	0.0415	80	0.16	8.79	−1.76	*
11636	J232331.69+151401.6	0.0394	84	0.17	8.76	−1.34	*
11395	J232337.45+133908.1	0.0425	35	0.23	8.95	−1.82	*
11524	J232423.53+152636.3	0.0256	15	0.37	8.71	−1.70	–
11585	J232516.78+142135.6	0.0445	10	0.43	9.27	−1.81	*
11544	J232538.54+152115.9	0.0412	4	0.74	9.43	−1.79	*
11568	J233013.51+132801.7	0.0417	5	0.61	9.36	−1.84	*
11567	J233019.67+132657.4	0.0399	4	0.71	9.38	−1.84	*
11791	J235159.08+144504.1	0.0466	19	0.34	9.20	−1.75	*

of the profile that was integrated to measure the H I flux and the peaks used for width measurement, respectively.

APPENDIX B: NOTES ON INDIVIDUAL OBJECTS

We list here notes for galaxies marked with an asterisk in the last column of Tables A2 and A3. The galaxies are ordered by increasing GASS number. In what follows, AA2 is the abbreviation for ALFALFA detection code 2.

Detections (Table A2)

3666 – small blue companion ∼1 arcmin SW, SDSS J011759.89+153148.0 ($z = 0.038\,248$), some contamination certain. There is also a blue galaxy ∼3 arcmin N, no SDSS redshift.

3851 – offset from SDSS redshift, confused. This is a galaxy group, including a blue disc ∼2 arcmin W (SDSS J013844.52+150331.1, $z = 0.028\,769$, 8625 km s^{-1}) and two early-type galaxies ∼1.5 arcmin SW (SDSS J013848.58+150141.2, $z = 0.028\,044$) and ∼2 arcmin SE (SDSS J013854.76+150117.7, $z = 0.027\,916$).

3917 – marginal detection. Notice companion spiral galaxy ∼4 arcmin NW, SDSS J015742.52+132318.8 ($z = 0.044\,431$).

3936 – small blue disc ∼2 arcmin N has no SDSS redshift.

3960 – spectacular pair of interacting galaxies in the foreground ($z = 0.012$). AA2.

3966 – blend/confused with blue companion ∼2 arcmin W, SDSS J020447.70+140147.8 ($z = 0.030\,942$).

Downloaded from http://mnras.oxfordjournals.org/ at Swinburne University of Technology on August 11, 2014

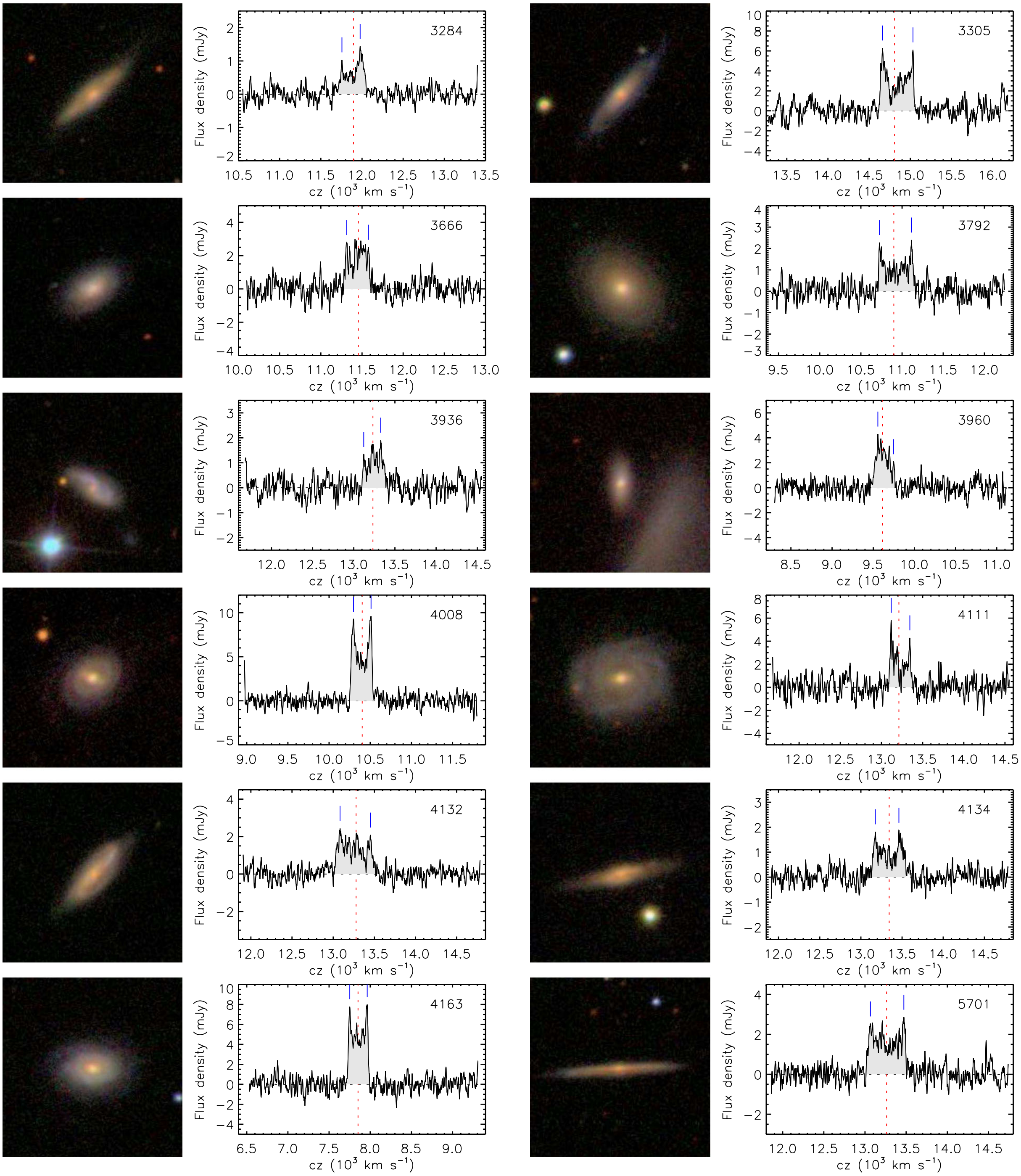

Figure A1. SDSS postage stamp images (1 arcmin^2) and H I-line profiles of the detections included in this final data release, ordered by increasing GASS number (indicated in each spectrum). The H I spectra are calibrated, smoothed and baseline subtracted. A dotted line and two dashes indicate the heliocentric velocity corresponding to the SDSS redshift and the two peaks used for width measurement, respectively. This is a sample of the complete figure, which is available as Supporting Information in the online version of the article.

3987 – detected blue companion ∼2 arcmin W, SDSS J021327.81+132806.1 ($z = 0.041\,604$, 12 473 km s^{-1}), confusion certain.

4056 – high-frequency edge uncertain, systematic error. Small blue cloud at the N edge of the galaxy, perhaps responsible for the peak at 11 750 km s^{-1}?

4111 – AA2.

4136 – low-frequency edge uncertain, systematic error. Blue companion ∼40 arcsec SE, SDSS J015706.42+130926.9 ($z = 0.032\,673$, 9795 km s^{-1}), confused. The blue galaxy ∼40 arcsec NE, SDSS J015706.42+131039.4, has $z = 0.044\,781$.

Downloaded from http://mnras.oxfordjournals.org/ at Swinburne University of Technology on August 11, 2014

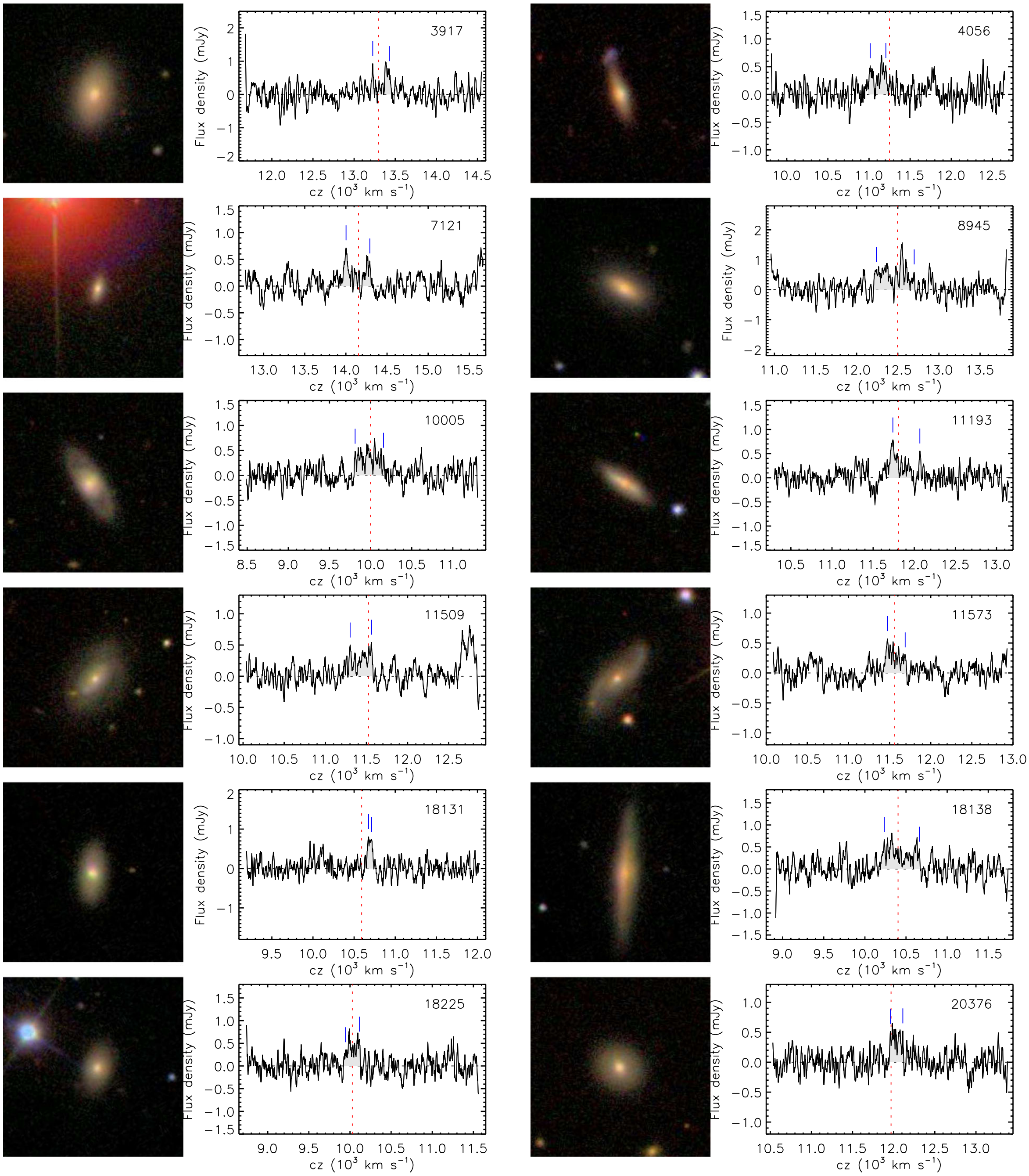

Figure A2. Same as Fig. A1 for marginal and/or confused detections. Here galaxies are sorted by quality flag first (starting with code 2 and increasing) and, within each category, by GASS number. This is a sample of the complete figure, which is available as Supporting Information in the online version of the article.

4165 – confused: blue companions ∼1.5 arcmin W (SDSS J015040.40+134106.1, $z = 0.044\,814$, 13 435 km s^{-1}) and 3 arcmin S (SDSS J015047.04+133824.1, $z = 0.044\,37$, 13 302 km s^{-1}); two other blue galaxies within 3 arcmin NE are in the background (SDSS J015057.74+134249.2, $z = 0.050$ and SDSS J015052.62+134318.6, $z = 0.057$).

5701 – two blue galaxies within 2.5 arcmin are in the background ($z = 0.08$); small early-type galaxy 40 arcsec N has no SDSS redshift, but is unlikely to contaminate the signal.

6015 – RFI spike at 1375 MHz (∼9900 km s^{-1}).

6679 – RFI feature at 1360 MHz (13 300 km s^{-1}). Three blue galaxies ∼3 arcmin W: the large edge-on disc (SDSS J130158.47+030602.6, $z = 0.023\,386$ from NED) and its small companion to the N are in the foreground, and SDSS J130200.53+030550.1 is in the background ($z = 0.079\,602$).

7121 – near bright star.

7405 – asymmetric profile, uncertain width; several small galaxies within 2 arcmin, the only two with redshifts are in the background ($z = 0.056$ and $z = 0.13$).

Downloaded from http://mnras.oxfordjournals.org/ at Swinburne University of Technology on August 11, 2014

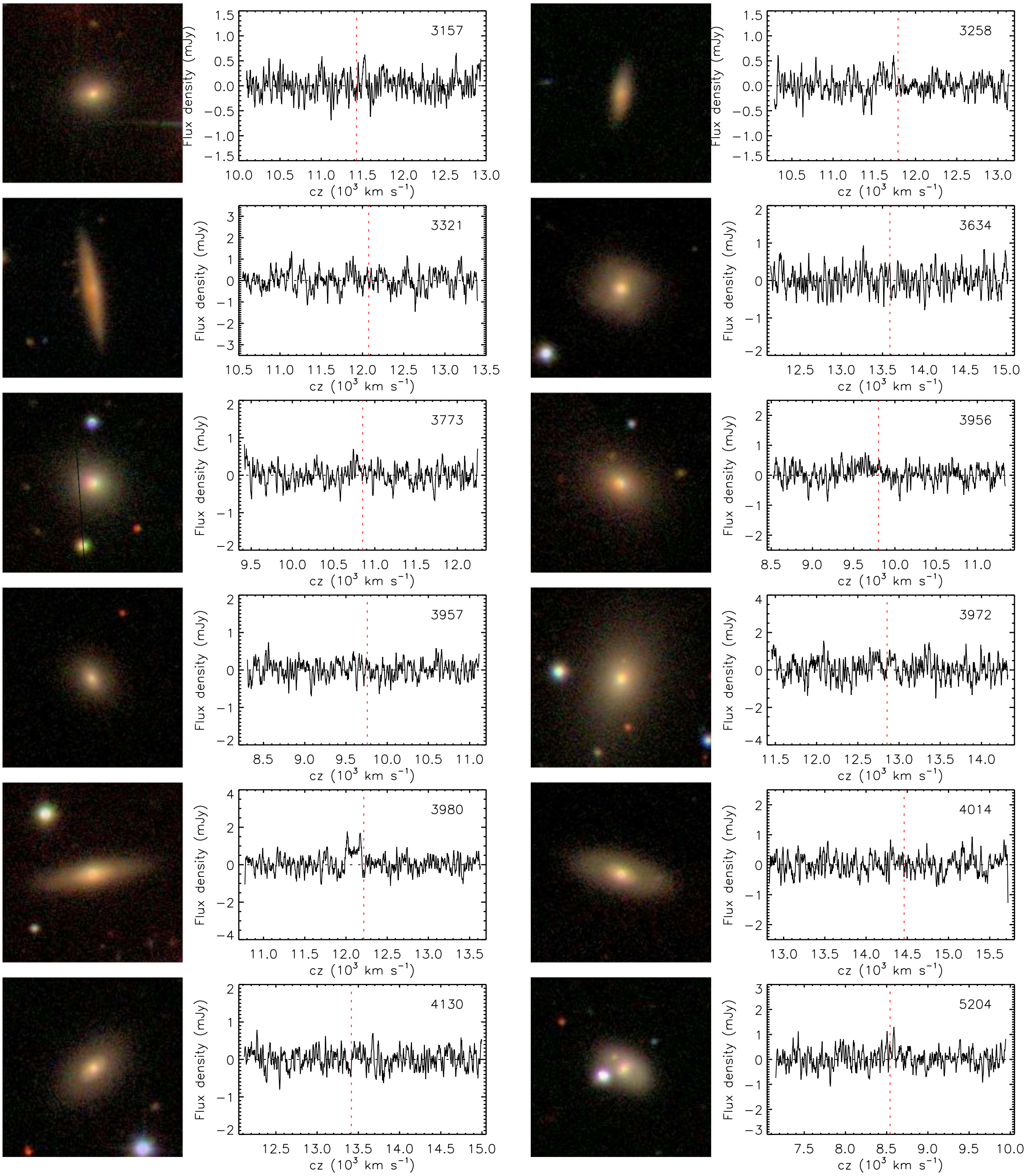

Figure A3. Same as Fig. A1 for non-detections. This is a sample of the complete figure, which is available as Supporting Information in the online version of the article.

7813 – blue companion ∼1.5 arcmin E, SDSS J151249.84+012827.7 (z = 0.0304, 9114 km s^{-1}), is separated enough in velocity not to cause any confusion (there is a small peak at the right velocity, but it is present in one polarization only). Also, blue companion 3.6 arcmin NW, SDSS J151233.08+013017.3 (z = 0.029 178).

8096 – low-frequency edge uncertain, systematic error. Small blue companion ∼1.5 arcmin SW, SDSS J085249.56+030823.9 (z = 0.034 776), some contamination certain.

8634 – possibly confused with blue galaxy ∼2 arcmin N, SDSS J101322.37+050312.7, no optical redshift (photometric redshift z = 0.042).

8945 – blue companion ∼3 arcmin W, SDSS J105303.39+042036.5 (z = 0.041 924, 12 568 km s^{-1}), some contamination likely; the blue galaxy ∼1 arcmin NW has z = 0.066.

9615 – RFI spike at 1375 MHz (∼9900 km s^{-1}), two channels replaced by interpolation. No companions within 3 arcmin,

Downloaded from http://mnras.oxfordjournals.org/ at Swinburne University of Technology on August 11, 2014

galaxy ~2.5 arcmin SW is in the background (SDSS J142955.29+032157.1, $z = 0.168$).

9942 – stronger in polarization A. Blend/confused with edge-on disc 0.4 arcmin NE, SDSS J144326.39+042308.2, $cz = 7879$ km s^{-1} from NED. Blue galaxy ~2.5 arcmin NE, SDSS J144332.81+042423.1, has $z = 0.071$.

10005 – blue disc ~3 arcmin SW, SDSS J145259.66+033013.2, is in the background ($z = 0.045$).

10032 – three galaxies ~1 arcmin N, 2 arcmin E and 2.5 arcmin SE are in the background ($z = 0.094$, 0.209 and 0.094, respectively).

11086 – 2.7 Jy continuum source at 5 arcmin, standing waves.

11092 – galaxy pair, the companion is a blue spiral ~15 arcsec SE, SDSS J231340.49+140115.5 ($z = 0.040\,436$, 12 122 km s^{-1}). Notice another two disc galaxies at the same redshift, ~2.5 arcmin SW (SDSS J231334.71+135912.4, $z = 0.039\,767$) and ~3 arcmin NW (SDSS J231330.39+140349.7, $z = 0.039\,527$).

11193 – uncertain profile; early-type companion ~1.5 arcmin E, SDSS J231328.01+141611.3 ($z = 0.038\,994$, 11 690 km s^{-1}); another companion ~4 arcmin NE, SDSS J231331.44+141938.7 ($z = 0.039\,231$, 11 761 km s^{-1}), significant contamination unlikely. Small galaxy 40 arcsec W has $z = 0.150$. Better in polarization B.

11291 – companion of GASS 11292, ~2.5 arcmin SW; strong contamination is unlikely, see note for GASS 11292.

11292 – most of the signal comes from GASS 11291 ~2.5 arcmin NE, as can be seen by comparing the two profiles.

11312 – galaxy triplet, H I signal is most likely a blend. The two companions are disc galaxies 1.9 arcmin NE (SDSS J231229.22+135632.1, $z = 0.034\,137$) and 2.3 arcmin N (SDSS J231224.51+135704.5, $z = 0.034\,135$).

11347 – most likely confused/blend with large spiral ~2 arcmin W, SDSS J231639.26+153516.2 ($z = 0.038\,807$ from NED).

11434 – small companion ~2.5 arcmin S, SDSS J232328.01+140530.2 ($z = 0.041\,497$), some contamination possible.

11435 – small companions ~2 arcmin NW (SDSS J232314.91+141817.8, $z = 0.043\,379$) and ~2.5 arcmin S (SDSS J232318.65+141446.6, $z = 0.044\,175$), some contamination possible. Large spiral galaxy ~3 arcmin NE is in the foreground ($z = 0.026$).

11509 – high-frequency edge uncertain, systematic error. Detected (part of) blue companion ~1.7 arcmin NW, SDSS J232403.09+145137.7 ($z = 0.042\,698$, 12 801 km s^{-1}).

11573 – stronger in polarization B. Early-type companion 2 arcmin E, SDSS J233019.67+132657.3 ($z = 0.039\,838$); the early-type galaxy ~1 arcmin N, SDSS J233013.51+132801.6, has $z = 0.041\,588$ (12 468 km s^{-1}).

11669 – edge-on galaxy ~1 arcmin SE, SDSS J232715.24+152752.4 ($z = 0.046\,110$ from NED), some contamination possible (although the profile is consistent with the fact that the target is almost face-on). AA2.

12062 – reddish companion ~2 arcmin NE, same redshift ($z = 0.036\,556$), and two small galaxies ~30 arcsec S, no redshifts; small contamination possible.

13159 – no obvious companion within the beam; however, notice two small, blue smudges ~1 and 1.5 arcmin E, without optical redshifts.

13618 – blend with companion 1 arcmin S, SDSS J135621.74+043606.0 ($z = 0.033\,82$, 10 139 km s^{-1}).

13674 – AA2.

14247 – small companion ~2 arcmin SW, SDSS J080523.82+355454.5 ($z = 0.033\,211$), some contamination possible.

15257 – uncertain profile; most likely confused/blend with blue galaxy ~45 arcsec W, SDSS J104802.72+060103.7, without optical redshift.

17622 – disc galaxy ~1.5 arcmin SW is in the background ($z = 0.061$). AA2.

17673 – confused/blend with blue companion ~3 arcmin E, SDSS J110009.92+102214.1 ($z = 0.036\,759$, 11 020 km s^{-1}); small galaxy ~1 arcmin SE has $z = 0.092$.

18084 – detected blue companion ~2 arcmin W, SDSS J115104.26+085225.0 ($z = 0.036\,558$, 10 960 km s^{-1}).

18131 – two blue galaxies in the background, one ~1 arcmin N (SDSS J120446.89+092617.6, $z = 0.069$) and one 3 arcmin S (SDSS J120446.35+092222.2, $z = 0.041$). Notice however blue, low surface brightness (LSB) galaxy 1 arcmin S, SDSS J120445.64+092426.7, without optical redshift. Confused?

18138 – early-type companion ~3 arcmin W, SDSS J120227.14+085548.2 ($z = 0.034\,643$), significant contamination unlikely. Stronger in polarization B.

18225 – blue disc ~1 arcmin W, SDSS J120507.73+103352.6, without optical redshift. Small blue galaxy ~2 arcmin E, SDSS J120517.65+103320.5, has $z = 0.023$. Notice large early-type companion ~3.5 arcmin N, SDSS J120514.04+103647.6 ($z = 0.033\,449$). Three other galaxies ~3 arcmin away in the W quadrant are in the background ($z = 0.09$).

19672 – galaxy pair.

19989 – several small galaxies around without optical redshifts; galaxy ~2.5 arcmin SW, SDSS J085419.08+081057.2, has $z = 0.096$.

20041 – large, blue companion 3.3 arcmin NE, SDSS J091437.31+080702.0 ($z = 0.031\,015$ from NED). The companion is detected by ALFALFA (AGC 191126) with $W_{50} = 402$ km s^{-1} and flux of 3.09 Jy km s^{-1}. Confused?

20376 – polarization mismatch (clear, overlapping signal in both polarizations, but offset by 1 MHz). The signal is most likely confused/blend with that of a blue spiral ~2.5 arcmin NW, SDSS J095407.95+103625.6 (also AGC 193987, detected by ALFALFA; $z = 0.040\,392$, 12 109 km s^{-1}). Notice also GASS 20445 ~3 arcmin E ($z = 0.039\,708$, 11904 km s^{-1}; non-detection in this release).

23070 – spiral galaxy 3 arcmin W has $z = 0.109$.

23496 – RFI spikes near 1352.5 MHz (~15 000 km s^{-1}). Small companion ~1 arcmin E, SDSS J105725.50+120638.9 ($z = 0.047\,348$), and galaxy ~30 arcsec NW without SDSS redshift; some contamination possible. AA2.

Downloaded from http://mnras.oxfordjournals.org/ at Swinburne University of Technology on August 11, 2014

23703 – small blue galaxy ∼2 arcmin S, no optical redshift.

23739 – blue companion ∼3 arcmin SW, SDSS J113655.36+115053.9 (z = 0.034 412, 10 316 km s^{-1}), separated enough in velocity from the target.

23781 – confused/blend with large blue spiral ∼2 arcmin NW, SDSS J114206.64+113216.0 (z = 0.042 924, 12 868 km s^{-1}).

23789 – most likely confused/blend with blue companion ∼2.7 arcmin E, SDSS J114154.89+123030.7 (z = 0.034 531, 10 352 km s^{-1}).

23815 – small galaxy ∼20 arcsec SW has no redshift; blue galaxy ∼2 arcmin E is in the background (z = 0.052).

24496 – small blue companion ∼2 arcmin N, SDSS J111809.86+074845.7 (z = 0.041 832), some contamination certain.

25215 – several galaxies to the S, all in the background.

25721 – small blue galaxy ∼1.7 arcmin S, SDSS J155507.68+092848.6, no optical redshift.

26406 – small galaxy ∼2.5 arcmin W has z = 0.044; smudge ∼1 arcmin E has no SDSS redshift.

26407 – RFI spike at 1352.6 MHz (15 000 km s^{-1}). Edge-on galaxy ∼2 arcmin NE is in the background (z = 0.086).

26586 – notice two blue, edge-on discs ∼4 arcmin from the target and with similar redshifts: SDSS J103624.87+130827.0 (4 arcmin SE, z = 0.034 084) and SDSS J103619.24+131317.5 (3.5 arcmin NE, z = 0.033 366).

28062 – most likely blend with small companion ∼1.5 arcmin E, SDSS J122807.37+081057.3 (z = 0.037 407, 11 214 km s^{-1}), which is exactly centred on the highest peak. Also notice companion galaxy ∼3.5 arcmin NE.

28317 – companion ∼2 arcmin NW, SDSS J154403.74+274152.5 (z = 0.031 411), but there is no hint of detection on the side away from GASS 28317, so contamination is unlikely. Notice however disc galaxy next to it, without optical redshift.

28703 – AA2.

31095 – AA2.

32308 – AA2.

33214 – high-frequency edge uncertain, systematic error. The disc galaxy ∼2.5 arcmin S has z = 0.050.

33737 – disturbed, no companions within the beam, large offset from SDSS redshift (z = 0.026 869, 8055 km s^{-1}).

38198 – several galaxies within 3 arcmin in the background (z = 0.097).

38458 – uncertain profile; blend: connected to large companion ∼40 arcsec E, SDSS J140606.72+123013.6 (also GASS 25575, not detected in DR1; z = 0.037 966, 11 382 km s^{-1}); notice also small companion ∼1.5 arcmin W, SDSS J140557.71+123016.6 (z = 0.039 257, 11 769 km s^{-1}).

39082 – blue LSB galaxy ∼1 arcmin SE, no optical redshift (photo-z = 0.037), possible contamination. AA2.

40495 – low-frequency edge uncertain, systematic error; stronger in polarization A.

40502 – 163 mJy continuum source at 1 arcmin, standing waves.

41718 – detected blue companion in board 3, ∼1365 MHz (∼12 150 km s^{-1}), most likely the very blue galaxy ∼1 arcmin NW, SDSS J144334.78+083432.3 (no optical redshift); galaxy ∼2.5 arcmin W, SDSS J144328.85+083248.9, has z = 0.033 037 (9904 km s^{-1}).

41863 – interacting pair of blue galaxies: the companion is ∼40 arcsec E, SDSS J151031.62+072500.2 (cz = 9597 km s^{-1} from NED).

41869 – detected blue companion, SDSS J150921.31+070631.4, ∼2 arcmin N (z = 0.037 367, 1369.24 MHz, 11 200 km s^{-1}); galaxy ∼1 arcmin NE is in the background (z = 0.078).

42191 – profile edges uncertain, systematic error.

42233 – several galaxies within 3 arcmin in the background (z > 0.08).

44856 – tiny blue galaxy ∼1.5 arcmin S, SDSS J135409.08+243200.3, unknown redshift.

48356 – high-frequency edge uncertain, systematic error. Interacting with SDSS J111113.00+284242.7, ∼1 arcmin N (z = 0.029 366, 8804 km s^{-1}); several other galaxies with similar redshift within 3 arcmin.

48518 – low-frequency edge uncertain, systematic error; uncertain profile. Blend with large spiral 2 arcmin S, SDSS J111750.61+263732.8 (z = 0.027 048, 8109 km s^{-1}); there is also a small companion ∼1 arcmin N, SDSS J111751.46+264035.3 (z = 0.026 349, 7899 km s^{-1}).

48521 – small blue galaxy ∼30 arcsec E, SDSS J111740.84+263502.1, unknown redshift, possible confusion. AA2.

48604 – small blue companion ∼1.5 arcmin N, SDSS J112746.74+265909.7 (z = 0.033 782, 10 129 km s^{-1}), some contamination certain. Several smaller galaxies within ∼2 arcmin, either in the background or without SDSS redshift. AA2.

48994 – two small blue companions ∼2.5 arcmin NE, SDSS J114225.77+301549.5 and SDSS J114227.14+301552.6 (both have z = 0.033), likely adding very little to the signal (given their size and distance to the target).

49386 – small spiral ∼2 arcmin SW is in the background (z = 0.080).

49727 – low-frequency edge uncertain, systematic error. Galaxy pair, separation 4 arcsec (from NED); H I signal also blended with that of UGC 7064 (∼1 arcmin S, z = 0.024 916, 1385.88 MHz, face-on blue galaxy, which is responsible for the low-velocity peak) and likely with that of SDSS J120445.26+310927.8 (blue galaxy 2 arcmin S, z = 0.026 637, 1383.55 MHz).

50404 – small companion ∼2 arcmin SW, SDSS J123400.02+280641.8 (z = 0.040 307), some contamination possible. Spiral ∼3 arcmin NE is in the background (z = 0.084).

50406 – low-frequency edge uncertain, systematic error.

51150 – small companion ∼1 arcmin S, SDSS J132301.23+270558.8 (z = 0.034 507); notice also blue companion 3.7 arcmin SE, SDSS J132309.49+270359.2 (z = 0.034 215); significant contamination unlikely.

Downloaded from http://mnras.oxfordjournals.org/ at Swinburne University of Technology on August 11, 2014

51161 – AA2.

51334 – small companion ∼1.5 arcmin N, SDSS J075331.69+140237.3 (z = 0.029 093), some contamination possible. AA2.

51580 – red companion ∼2 arcmin SW, SDSS J080359.21+150343.1 (z = 0.039), significant contamination unlikely. Several small galaxies nearby without SDSS redshift.

51899 – blend with two companions, a blue edge-on disc 2 arcmin S (SDSS J083131.00+192042.6, z = 0.039 271) and a large galaxy ∼2.5 arcmin E (SDSS J083140.72+192307.8, z = 0.038 759); there is also a small bluish galaxy ∼15 arcsec NE without optical redshift.

52045 – disturbed (tidal tail or companion to the S).

52297 – companion ∼2 arcmin NE, SDSS J085724.03+204237.8 (z = 0.032 874), plus several galaxies nearby without SDSS redshifts; some contamination likely.

55541 – small blue galaxy ∼1 arcmin SW has z = 0.048, no contamination problems.

55745 – stronger in polarization B.

56509 – 111 mJy continuum source at 2 arcmin, standing waves. Small blue companion ∼2 arcmin N, SDSS J085047.04+115102.8 (z = 0.029 322), some contamination likely.

56662 – a few small galaxies within 3 arcmin, all in the background.

Non-detections (Table A3)

3157 – small face-on, spiral companion ∼2 arcmin E, SDSS J003042.29+145610.4 (z = 0.038 491, 11 539 km s^{-1}).

3258 – perhaps hint of galaxy signal; blue galaxy ∼2.5 arcmin SW has z = 0.076.

3972 – edge-on companion ∼3 arcmin SW, SDSS J020530.66+143652.7 (z = 0.042 305, 12 683 km s^{-1}); hint of signal centred at 12 800 km s^{-1} is in polarization B only.

3980 – detected LSB companion ∼1.5 arcmin S, SDSS J021424.66+121836.7 (z = 0.040 399, 12 111 km s^{-1}, in much better agreement with SDSS redshift). Stronger in polarization A.

4014 – small companion ∼3.5 arcmin NE, SDSS J020732.08+130338.3 (z = 0.048 163, 14 439 km s^{-1}).

4130 – blue companion ∼3.5 arcmin W, SDSS J015706.42+131039.4 (z = 0.044 781); several other galaxies within 3 arcmin, with redshifts significantly different from GASS 4130 or unknown.

5204 – blue companion ∼3 arcmin SE, SDSS J102800.60+023414.1 (z = 0.028 467, 8534 km s^{-1}) also not detected.

7310 – the two disc galaxies 3 arcmin S and ∼3.5 arcmin NE have z > 0.05.

8953 – blue companion ∼3 arcmin NE, SDSS J105251.60+041109.3 (z = 0.043 311, 12 984 km s^{-1}), marginally detected?

8971 – two companions: edge-on disc ∼1.5 arcmin NW, SDSS J104832.28+044838.1 (z = 0.033 723, 10 110 km s^{-1}) and face-on, blue spiral ∼3 arcmin NW, SDSS J104827.34+044931.7 (z = 0.034 128, 10 231 km s^{-1}), also not detected. The small galaxy ∼3 arcmin SE, SDSS J104847.35+044605.5, has z = 0.026.

9702 – small galaxy ∼1 arcmin W, SDSS J144039.22+032250.3 (z = 0.030 114, 9028 km s^{-1}); several other galaxies within ∼3 arcmin with redshifts z < 0.028 or z > 0.089.

10211 – blue galaxy ∼1.5 arcmin S has z = 0.093.

11080 – double nucleus; detected blue companion ∼2 arcmin N in board 3, SDSS J225609.41+130551.4 (z = 0.037 436, 1369.15 MHz).

11249 – companion of GASS 11257, ∼2 arcmin E (SDSS J230806.95+152520.2, z = 0.036 716, see next note); large early-type galaxy ∼0.5 arcmin N without optical redshift.

11257 – companion of GASS 11249, ∼2 arcmin W (SDSS J230757.92+152455.2, z = 0.036 23, see previous note); large early-type galaxy ∼2.5 arcmin W without optical redshift.

11284 – perhaps hint of galaxy signal.

11395 – small companion ∼2 arcmin S, SDSS J232336.22+133706.0 (z = 0.042 373, 12 703 km s^{-1}).

11410 – detected companion without redshift? perhaps the small LSB galaxy ∼0.5 arcmin NW, SDSS J232220.71+135957.4; the signal is significantly stronger in polarization A, although no RFI is visible at that frequency.

11544 – AA2. Marginally detected disc galaxy ∼2 arcmin NW, SDSS J232531.72+152211.6 (z = 0.040 311, 12 085 km s^{-1}).

11567 – two companions, a large spiral 2 arcmin W, SDSS J233011.60+132656.2 (z = 0.038 729, 11 611 km s^{-1}) and a small one ∼2 arcmin SE, SDSS J233024.64+132531.6 (z = 0.039 084, 11 717 km s^{-1}); notice also the early-type galaxy ∼2 arcmin NW, SDSS J233013.51+132801.6 (z = 0.041 588, 12 468 km s^{-1}).

11568 – large early-type galaxy ∼2 arcmin SE, SDSS J233019.67+132657.3 (z = 0.039 838) and a spiral ∼1.5 arcmin S, SDSS J233011.60+132656.2 (z = 0.038 729).

11585 – marginally detected blue companion ∼3 arcmin N, SDSS J232519.80+142419.5 (z = 0.042 036, 12 602 km s^{-1}).

11636 – two blue companions: SDSS J232336.90+151532.2 ∼2 arcmin NE (z = 0.043 298, 12 980 km s^{-1}) and GASS 11494 ∼2.5 arcmin S (SDSS J232335.34+151148.7, z = 0.042 709, 12 804 km s^{-1}, DR2 detection). The H I signal is most likely a blend of the two.

11791 – marginally detected blue companion ∼1.5 arcmin SE, SDSS J235205.28+144403.6 (z = 0.0450, 13 491 km s^{-1}); another two galaxies with similar redshifts ∼2 arcmin N (SDSS J235158.07+144711.1, z = 0.046 598, 13 970 km s^{-1}) and ∼3.5 arcmin SW (SDSS J235148.64+144241.3, z = 0.046 466, 13 930 km s^{-1}).

11892 – three galaxies within 3 arcmin with z > 0.09, and two edge-on discs ∼3 arcmin S without optical redshifts.

11903 – two small galaxies within 0.5 arcmin without optical redshift.

Downloaded from http://mnras.oxfordjournals.org/ at Swinburne University of Technology on August 11, 2014

12452 – companion ~2 arcmin S, SDSS J112003.92+040830.2 (z = 0.049 371, 14 801 km s^{-1}); three other galaxies within 2.5 arcmin with $z = 0.15$.

12967 – companion of GASS 12970, ~2 arcmin S (SDSS J123553.79+054539.8, z = 0.041 788, DR2 non-detection). Small galaxy ~2.5 arcmin S, SDSS J123556.38+054459.2 (z = 0.041 189, 12 348 km s^{-1}) also not detected. $T_{\rm max}$ not reached; perhaps hint of galaxy signal, but stronger in polarization A.

14017 – small blue cloud to the NW edge of the galaxy; galaxy pair ~4 arcmin SW in the foreground ($z = 0.016$).

14260 – small blue galaxy ~2 arcmin S has $z = 0.145$.

16756 – edge-on disc ~40 arcsec SE and small blue galaxy ~1 arcmin SW, both without optical redshift.

18004 – barred spiral galaxy ~40 arcsec SE and small galaxy ~40 arcsec W, both without optical redshifts; small early-type companion ~2.5 arcmin E, SDSS J115145.97+084531.2 (z = 0.035 926) also not detected.

18220 – perhaps hint of galaxy signal. Early-type companion ~2.5 arcmin W, SDSS J120527.47+104204.4 (z = 0.035 443, 10 626 km s^{-1}); the blue galaxy ~2.5 arcmin NW, SDSS J120530.37+104313.8, has $z = 0.063$.

19274 – AA2. Small companion ~3 arcmin N, SDSS J081622.22+260241.1 (z = 0.045 113) also not detected.

20149 – hint of galaxy signal.

20165 – detected companion (GASS 20133, DR1 detection) ~1 arcmin E (SDSS J093236.58+095025.9, z = 0.048 884, 14 655 km s^{-1}).

20445 – companion of GASS 20376, ~3 arcmin W (SDSS J095416.83+103457.5, z = 0.039 938, see detections in this release).

23029 – three companions: SDSS J102714.26+110340.0, ~2 arcmin W (z = 0.032 969), SDSS J102710.59+110116.2, ~2.5 arcmin S (z = 0.032 657) and SDSS J102707.78+110038.5, ~3 arcmin S (z = 0.032 367).

23102 – perhaps hint of galaxy signal.

23203 – detected companion, probably the LSB galaxy ~3 arcmin E, SDSS J103602.58+121118.3 (z = 0.038 124, 11 429 km s^{-1}), but notice also blue smudge ~1.5 arcmin NE without optical redshift.

23457 – early-type galaxy ~1 arcmin NE without optical redshift.

23531 – RFI at 1370 MHz (~11 000 km s^{-1}) visible in final spectrum.

25057 – companion of GASS 25115 (SDSS J152112.78+303928.5, ~1.8 arcmin SE, see next note), also not detected; several other galaxies within 3 arcmin in the background ($z > 0.07$).

25115 – companion of GASS 25057 (SDSS J152106.26+304036.9, see previous note), also not detected; several other galaxies within 3 arcmin in the background ($z > 0.07$).

25213 – detected companion, most likely SDSS J131221.39+114022.8, 3 arcmin S (z = 0.030 132, 9033 km s^{-1}). Two other galaxies within the beam with slightly higher redshift: SDSS J131229.71+114432.7, ~2 arcmin NE (z = 0.030 916, 9268 km s^{-1}) and GASS 25214 (SDSS J131232.81+114344.2, z = 0.031 105, 9325 km s^{-1}), 2.5 arcmin E, which was not detected in DR1.

25682 – three galaxies within ~3.5 arcmin at slightly higher redshift ($z = 0.042$), plus others without optical redshifts.

26017 – large early-type companion ~2.5 arcmin SW, SDSS J095634.77+110947.4 (z = 0.041 272, 12 373 km s^{-1}), and small disc galaxy ~2 arcmin W, SDSS J095633.88+111058.2 (z = 0.040 49, 12 139 km s^{-1}).

26503 – large early-type companion 3 arcmin SE, SDSS J102323.75+125006.1 (z = 0.032 486, 9739 km s^{-1}); other galaxies within 3 arcmin are in the background or have no redshift.

28030 – perhaps hint of galaxy signal, but present in polarization B only.

28327 – next to bright star; two companion spirals ~3.5 arcmin E (SDSS J154145.55+275917.8, z = 0.032 026) and 4 arcmin N (SDSS J154135.57+280258.6, z = 0.031 891, AA2).

28348 – companion ~2 arcmin SE, SDSS J154100.75+281922.9 (z = 0.032 234, 9664 km s^{-1}); the small blue galaxy ~2 arcmin E has $z = 0.066$.

30746 – galaxy ~1 arcmin NW has $z = 0.079$.

31478 – hint of galaxy signal; two galaxies ~2 arcmin W and ~2 arcmin NW have $z = 0.063$.

33469 – small blue galaxy ~2.5 arcmin E is in the foreground ($z = 0.005$).

33777 – detected blue companion ~2 arcmin W, SDSS J100240.68+323749.4 (z = 0.045 315, 13 585 km s^{-1}); several other galaxies within 3 arcmin with redshifts between 0.048 and 0.052.

35475 – face-on spiral galaxy ~3 arcmin SE, SDSS J125941.30+283025.9 (z = 0.027 566, 8264 km s^{-1}), also not detected.

35497 – hint of galaxy signal. Four galaxies within 3.5 arcmin are in the background ($z > 0.06$).

39407 – blue companion ~2 arcmin SE, SDSS J152248.12+083148.0 (z = 0.036 607, 10 975 km s^{-1}), and three galaxies ~2.5 arcmin away with $z = 0.034 - 0.035$ (SDSS J152236.57+083447.5, SDSS J152249.21+083337.9, SDSS J152244.22+083013.3).

41723 – blue companion ~3.5 arcmin NE, SDSS J144610.59+085807.7 (z = 0.029 595, 8872 km s^{-1}); also notice two blue discs ~2.5 arcmin N without optical redshifts.

44021 – small blue galaxy ~70 arcsec NE, SDSS J134235.17+301547.2, has $z = 0.124$; very blue galaxy ~2 arcmin SW, SDSS J134226.53+301311.0, has no optical redshift.

45940 – small bluish cloud to the N of the galaxy. Large red companion ~2.5 arcmin NE, SDSS J142758.18+263016.2 (z = 0.032 298) and two galaxies ~3 arcmin SE, SDSS J142759.07+262754.1 (z = 0.031 056) and SDSS J142759.98+262805.9 (no optical redshift).

Downloaded from http://mnras.oxfordjournals.org/ at Swinburne University of Technology on August 11, 2014

48160 – feature at ~13 250 km s^{-1} is present in both polarizations; detected perhaps the small blue galaxy ~1 arcmin S (SDSS J111203.29+274951.2) without optical redshift?

48205 – disc galaxy 2 arcmin N is in the foreground ($z = 0.037$); small galaxies within 1.5 arcmin without optical redshifts.

48544 – RFI spike at 1350 MHz (~15 600 km s^{-1}) visible in final spectrum. Small blue companion ~3 arcmin E, SDSS J112053.20+271816.7 ($z = 0.047\,646$, 14 284 km s^{-1}).

50866 – small disc galaxy ~2 arcmin SE, SDSS J125614.26+274856.0 ($z = 0.022\,243$, 6668 km s^{-1}); a few other small galaxies within 3 arcmin in the background ($z > 0.08$).

51462 – small, blue companion ~2 arcmin NW, SDSS J075555.63+141317.0 ($z = 0.036\,25$, 10 867 km s^{-1}) also not detected.

53269 – smaller galaxy almost superimposed is in the background (SDSS J093115.52+263255.8, $z = 0.058$).

54240 – two edge-on galaxies nearby, SDSS J102254.55+243639.4 (~20 arcsec NE, $z = 0.046\,341$, 13 893 km s^{-1}) and SDSS J102248.59+243622.3 (~1 arcmin W, no optical redshift).

54577 – companion ~2.5 arcmin W, SDSS J103007.19+273436.7 ($z = 0.047\,206$).

56320 – detected companion, large spiral ~1 arcmin N, SDSS J080343.91+100306.2 ($z = 0.034\,116$, 10 228 km s^{-1}); also notice small blue galaxy ~2.5 arcmin W, SDSS J080332.99+100259.1 ($z = 0.034\,658$).

56612 – three large, discy companions: SDSS J090320.38+134142.0, ~3 arcmin E ($z = 0.029\,988$), SDSS J090313.10+134444.1, ~3 arcmin NE ($z = 0.028\,401$) and SDSS J090254.93+133938.4, ~4 arcmin SW ($z = 0.029\,838$); the small galaxy ~40 arcsec W is in the background ($z = 0.102$).

56650 – perhaps hint of galaxy signal (not well centred on SDSS redshift).

SUPPORTING INFORMATION

Additional Supporting Information may be found in the online version of this article:

SDSS postage stamps and H I spectra. SDSS images and H I spectra of the galaxies are presented here, organized as follows: H I detections with quality flag 1 in Table A2 (Fig. A1), marginal and/or confused detections with quality flag 2–5 (Fig. A2) and non-detections (Fig. A3). The objects in each of these figures are ordered by increasing GASS number (indicated on the top-right corner of each spectrum). The SDSS images show a 1 arcmin^2 field, i.e. only the central part of the region sampled by the Arecibo beam (the half-power full width of the beam is ~3.5 arcmin at the frequencies of our observations). Therefore, companions that might be detected in our spectra typically are not visible in the postage stamps, but they are noted in Appendix B. The H I spectra are always displayed over a 3000 km s^{-1} velocity interval, which includes the full 12.5 MHz bandwidth adopted for our observations. The H I-line profiles are calibrated, smoothed (to a velocity resolution between 5 and 21 km s^{-1} for the detections, as listed in Table A2, or to ~15 km s^{-1} for the non-detections), and baseline subtracted. A red, dotted line indicates the heliocentric velocity corresponding to the optical redshift from SDSS. In Figs A1–A2, the shaded area and two vertical dashes show the part of the profile that was integrated to measure the H I flux and the peaks used for width measurement, respectively.
Figure A1. SDSS postage stamp images (1 arcmin^2) and H I-line profiles of the detections included in this final data release, ordered by increasing GASS number (indicated in each spectrum). The H I spectra are calibrated, smoothed and baseline subtracted. A dotted line and two dashes indicate the heliocentric velocity corresponding to the SDSS redshift and the two peaks used for width measurement, respectively.
Figure A2. Same as Fig. A1 for marginal and/or confused detections. Here galaxies are sorted by quality flag first (starting with code 2 and increasing) and, within each category, by GASS number.
Figure A3. Same as Fig. A1 for non-detections (http://mnras.oxfordjournals.org/lookup/suppl/doi:10.1093/mnras/stt1417/-/DC1).

Please note: Oxford University Press are not responsible for the content or functionality of any supporting materials supplied by the authors. Any queries (other than missing material) should be directed to the corresponding author for the article.

This paper has been typeset from a TEX/LATEX file prepared by the author.

Downloaded from http://mnras.oxfordjournals.org/ at Swinburne University of Technology on August 11, 2014